Forschungsbericht 2019-17

Multidisciplinary Design of High-Lift Systems

Dirk Matthias Franke

Deutsches Zentrum für Luft- und Raumfahrt
Institut für Aerodynamik und Strömungstechnik
Braunschweig

Deutsches Zentrum
DLR für Luft- und Raumfahrt

Forschungsbericht 2019-17

Multidisciplinary Design of High-Lift Systems

Dirk Matthias Franke

Deutsches Zentrum für Luft- und Raumfahrt
Institut für Aerodynamik und Strömungstechnik
Braunschweig

112 Seiten
68 Bilder
14 Tabellen
91 Literaturstellen

Deutsches Zentrum
DLR für Luft- und Raumfahrt

TU Braunschweig – Niedersächsisches
Forschungszentrum für Luftfahrt

Berichte aus der Luft- und Raumfahrttechnik

Forschungsbericht 2019-06

Multidisciplinary Design of High-Lift Systems

Dirk Matthias Franke

Deutsches Zentrum für Luft- und Raumfahrt
Institut für Aerodynamik und Strömungstechnik
Braunschweig

Diese Veröffentlichung wird gleichzeitig in der Berichtsreihe „NFL - Forschungsberichte“ geführt.

Diese Arbeit erscheint gleichzeitig als von der Fakultät für Maschinenbau der Technischen Universität Carolo-Wilhelmina zu Braunschweig zur Erlangung des akademischen Grades eines Doktor-Ingenieurs genehmigte Dissertation.

Multidisciplinary Design of High-Lift Systems

Von der Fakultät für Maschinenbau
der Technischen Universität Carolo-Wilhelmina zu Braunschweig

zur Erlangung der Würde
eines Doktor-Ingenieurs (Dr.-Ing.)
genehmigte Dissertation

von:	Dirk Matthias Franke
aus (Geburtsort):	Karlsruhe

eingereicht am:	17.10.2018
mündliche Prüfung am:	01.03.2019

Gutachter:	Prof. Dr.-Ing. C.-C. Rossow
	Prof. Dr.-Ing. P. Horst

2019

Multidisciplinary Design of High-Lift Systems

Deutsches Zentrum
für Luft- und Raumfahrt e.V.

Institut für Aerodynamik und Strömungstechnik
Abteilung Transportflugzeuge
Lilienthalplatz 7, 38108 Braunschweig

Braunschweig, im Juli 2019

Institutsdirektor:

Prof. Dr.-Ing. C.-C. Rossow

Verfasser:

Dipl.-Ing. D. M. Franke

Abteilungsleiter:

Prof. Dr.-Ing. R. Rudnik

Multidisciplinary Design of High-Lift Systems

Abstract

This work is dedicated to investigations of the interrelation of the disciplines involved in the multidisciplinary design of a two-dimensional high-lift system, provided by industry. The disciplines involved in this work are: kinematics, aerodynamics, mass estimation of the flap and slat mechanism and finally the flight mechanics. This thesis covers the development and implementation of the modules to simulate the deployment of the mechanism for the flap and to estimate the mass of the deployment mechanism of the slat and flap. In addition, a process chain is established to enable the generation of a multidisciplinary data base for the high-lift system. The results of this thesis indicate: First, the data base gained is plausible. Second, the multidisciplinary process is able to improve the performance of the high-lift system during take-off and landing. Third, recommendations are presented for the use of disciplines in the design of high-lift systems. Based on the results of this thesis, it is highly recommended to account the mechanisms for slat and flap in future high-lift design tasks. The flight mechanics is a relevant discipline to weight the aerodynamic coefficients for the different phases of take-off and landing in a realistic manner. It reflects well the quantities that are used widely for aerodynamic optimizations of high-lift systems. According to the analyses in this thesis, the negligence of the mass estimation for the high-lift mechanisms leads to a more conservative contemplation of the design issue. This means, that not the full potential for enhancements in the high-lift performance is exploited when the mass estimation is neglected. Variations in the mass of the flap mechanism are significantly higher in comparison to the variations for the mass of the slat mechanism. The reductions in the overall mass of the aircraft are a result of the mass reductions achieved by the flap mechanism, mostly for the slat mechanism an increase of its mass is recognized. These observations reflect only designs that improve both the take-off and landing performance. Finally, the variations in the take-off and landing performance are always judged in comparison with the baseline configuration. The baseline configuration is a highly sophisticated design of a very successful aircraft in service and was designed by industry in a multidisciplinary context. Based on this, it is reasonable that only minor enhancements are achieved in the take-off and landing performance. It is seen as a great success, that the automated process chain is able to detect optimal high-lift settings close to the baseline configuration and that the flight mechanics performance is even enhanced.

Multidisziplinärer Entwurf von Hochauftriebssystemen

Übersicht, Kurzfassung

Die Arbeit widmet sich dem Themengebiet des multidisziplinären Entwurfs von Hochauftriebssystemen. Dabei wird der Fokus auf die Untersuchung der gegenseitigen Beeinflussung der betrachteten Disziplinen gelegt. Das Hochauftriebssystem (zweidimensional) wurde von einem Industriepartner zur Verfügung gestellt. Folgende Disziplinen werden innerhalb dieser Arbeit betrachtet: Kinematik, Aerodynamik, Massenabschätzung des Mechanismus zum Ausfahren des Vorflügels und des Hinterkantenauftriebselements und schließlich die Flugmechanik. Die Arbeit umfasst die Entwicklung und Implementierung der Module zur Simulation des Ausfahrvorgangs des Vorflügels und der Hinterkantenklappe. Weiterhin wurde eine Prozesskette implementiert, mit der Zielsetzung eine multidisziplläre Datenbasis für Hochauftriebssysteme zu erstellen. Das Ergebnis der Optimierungen, d.h. der Datensatz, liefert erstens plausible Zusammenhänge. Zweitens wurde festgestellt, dass die Prozesskette Daten generiert, die die Start- und Landeleistung des Hochauftriebssystems verbessern. Drittens werden Empfehlungen aus den Ergebnissen abgeleitet, welche Disziplinen im Entwurfsprozess für Hochauftriebssysteme als geeignet erachtet werden. Die Ergebnisse legen nahe, dass es äußerst sinnvoll ist, den Mechanismus der Hochauftriebselemente für zukünftige Hochauftriebsoptimierungen zu berücksichtigen. Die Flugmechanik zeigte sich als geeignete Disziplin, um die einzelnen aerodynamischen integralen Beiwerte für die jeweiligen Flugphasen während Start und Landung realistisch zu gewichten. Diese Disziplin berücksichtigt zweckmäßig die Größen, die in der Hochauftriebsoptimierung standardmäßig Verwendung finden. Die Betrachtung der Masse des Hochauftriebssystems zeigte, dass die Vernachlässigung eben dieser zu einer konservativeren Betrachtung der Entwurfsaufgabe führt. Das bedeutet, dass nicht das ganze Verbesserungspotential für die Hochauftriebsleistung ausgeschöpft wird, wenn die Massen des Hochauftriebssystems vernachlässigt werden. Masseänderungen für den Hinterkantenklappenmechanismus sind weit ausgeprägter, als für den Mechanismus des Vorflügels. Die Senkung der Masse des Luftfahrzeuges ist auf die Verringerung der Masse des Hinterkantenklappenmechanismus zurückzuführen. Die Masse des Mechanismus des Vorflügels wird größtenteils erhöht. Diese Aussagen beziehen sich nur auf Entwürfe, die sowohl eine Verringerung der Startstrecke als auch der Landestrecke zeigen. Die Veränderungen in der Start- und Landeleistung werden immer im Vergleich zum initialen Entwurf (baseline configuration) bewertet. Dieser initiale Entwurf ist eine hochentwickelte Konfiguration eines sehr erfolgreichen im Betrieb befindlichen Luftfahrzeuges. Dieser Entwurf wurde von der Industrie in einem multidisziplinären Umfeld entworfen. Demnach ist es schlüssig, dass lediglich minimale Verbesserungen der Start- und Landeleistung erzielt wurden. Dies wird vielmehr als großer Erfolg bewertet, da die automatisierte Herangehensweise in der Lage ist Konfigurationen nahe des Initialentwurfs zu reproduzieren und fähig ist die Hochauftriebsleistung des Initialentwurfs noch weiter zu verbessern.

Acknowledgments

This thesis envolved during my employment at the institute of aerodynamics and flow technology at the German aerospace center (DLR) in Braunschweig and beyond.
Especially, I want to thank Jochen Wild who supported this thesis with guidance, great cooperativeness and with his broad expertise in the field of high-lift design.
Special thanks go to my doctoral adviser and head of institute, Professor Cord-Christian Rossow, who gave pragmatic and wise recommendations to finish this thesis successfully.
I want to thank Professor Peter Horst from the Technical University of Braunschweig for being my second doctoral adviser and supporting the work.
Professor Rolf Radespiel is thanked for chairing the PhD committee.
ASCO industries is thanked here for the collaboration with respect to the development of the mass estimation tool for the slat mechanism. Especially I want to thank Koën Peeters, Stein Janssens, Michaël Raets for the helpful, fruitful discussions and for the possibility to collaborate on site in Brussels with them.
At Airbus, special thanks go to Klaus Becker, Adrian Eberle and Daniel Reckzeh for providing a realistic, industrialized designed airfoil configuration, which helped substantially to show the potential of the process approach developed within this thesis.
The work is proudly dedicated to the four girls of my life, my brilliant wife Eva and my fantastic daughters, in order of appearance, Lotta, Stella and Paula.
The support of my family and friends, especially of my parents Annerose and Hermann Franke and of my siblings Christine Franke, Jochen Franke and Carolin Ecker is greatly acknowleged.
I want to say thank you to my former colleagues from the institute of aerodynamics and flow technology for many useful discussions and their support. Special thanks goes to: Ana Manso-Jaume, Luciana Savoni, Carlos O. Marquez Gutierrez, Carsten Lenfers, Sven Geisbauer, Vlad Ciobaca, Karl-Stéphan Rossignol, Mohammad Abu-Zurayek, Joël Brezillon, Andreas Schütte and Arno Ronzheimer.
Stefan Langer is thanked for providing a library to solve linear systems of equations.
I am thankful to Ralf Rudnik as head of my department for providing computational resources and funding.
Braunschweig, im Juli 2019

Contents

Nomenclature

Arabic Symbols

a	[m/s^2]	acceleration
AoA	[deg]	angle of attack
c	[-]	chord length
c_{clean}	[-]	chord length of the clean aifoil
c_{Flap}	[-]	chord length of the flap
c_{Slat}	[-]	chord length of the slat
c_p	[-]	pressure coefficient
C_D	[-]	drag coefficient
C_L	[-]	lift coefficient
dz	[-]	vertical distance of the flap towards the trailing edge of the main element
D	[N]	aerodynamic drag force
e	[-]	Oswald factor
$\vec{e}_{ij}$	[-]	vector with unit length of one
E	[m^2/s^2]	specific total energy per unit mass
$f_i(\vec{x})$	[-]	vector of objective functions
$F(\vec{x})$	[-]	single-objective function
F	[N]	force
F_N	[N]	normal force
F_Q	[N]	shear force
$\overline{\overline{F}}$		flux density vector
g	[m/s^2]	gravitational acceleration
$g_j(\vec{x})$	[-]	vector of equality or inequality constraints
h	[-]	number of objective functions
H_1	[m]	height at which the transition phase starts during landing
H_2	[m]	vertical distance in which the aircraft climbs with constant climb angle during take-off
H_{Climb}	[m]	height until take-off is evaluated
J		Jacobian matrix
k	[-]	number of mechanisms (stations)
k_1	[deg]	constant angle within the mechanism
l_B	[m]	length of the beam
L	[N]	aerodynamic lift force
m	[kg]	mass
m_c	[-]	total number of constraints
m_e	[-]	number of equality constraints
M	[Nm]	moment
M_{bending}	[Nm]	bending moment
Ma	[-]	Mach number
n	[-]	dimension of the parameter space

n	[-]	load factor
$\vec{n}$		outer normal vector
O/L	[-]	overlap
p	[N/m^2]	pressure
P	[-]	number of Cauchy samples
$\vec{q}$		vector of variables
R	[m]	radius of transition arc during take-off or landing
Re	[-]	Reynolds number
s	[m]	horizontal distance over ground
s_{App}	[m]	horizontal distance over ground for final approach during landing
s_B	[m]	height of beam
$s_{\text{GR, I}}$	[m]	horizontal distance for ground-roll during landing (part I: free ground-roll)
$s_{\text{GR, II}}$	[m]	horizontal distance for ground-roll during landing (part II: ground-roll with breaks applied and thrust reversal activated)
$s_{\text{GR, III}}$	[m]	horizontal distance for ground-roll during landing (part III: ground-roll with breaks applied till standstill)
s_{Landing}	[m]	overall horizontal distance over ground for landing
$s_{\text{Take-off}}$	[m]	overall horizontal distance over ground for take-off
$s_{\text{Take-off, climb}}$	[m]	horizontal distance over ground for climb during take-off
$s_{\text{Take-off, ground-roll}}$	[m]	horizontal distance for ground-roll during take-off
$s_{\text{Take-off, trans}}$	[m]	horizontal distance over ground for transition during take-off
s_{Trans}	[m]	horizontal distance over ground for transition during landing
S	[m^2]	wing area
S	[m]	outer boundary of control volume
t	[s]	time
T	[N]	thrust
T_{rev}	[N]	thrust reversal
T/W	[-]	thrust loading
$\vec{u}$		velocity vector
v	[m/s]	flow velocity, flight speed
v_{App}	[m/s]	approach speed during landing
v_{Climb}	[m/s]	climb speed during take-off
$v_{\text{Lift-off}}$	[m/s]	lift-off speed during take-off
$v_{\text{Stall, 1g, take-off}}$	[m/s]	stall speed for take-off configuration
$v_{\text{Stall, 1g, landing}}$	[m/s]	stall speed for landing configuration
$v_{\text{Touch-down}}$	[m/s]	touch-down speed during landing
v_{Trans}	[m/s]	transition speed during take-off or landing
V	[m^3]	control volume
$\vec{V}_{ij}$	[-]	vector
VFTO	[m/s]	final take-off speed
w	[-]	factor to weight objective functions

W	[N]	weight
W/S	[N/m^2]	wing loading
$\vec{W}$		vector of conservative state variables
$\vec{x}$		vector of design variables
x	[m]	x-coordinate
y	[m]	y-coordinate
z	[m]	z-coordinate
z_{loc}	[m]	local z-coordinate

Greek Symbols

β	[deg]	sweep angle
δ	[deg]	deflection angle
δ_{Flap}	[deg]	deflection angle of flap element
δ_{Slat}	[deg]	deflection angle of slat element
ϵ	[-]	convergence criterion
ϵ_2	[m]	convergence criterion
γ	[deg]	constant angle within the mechanism
γ_{App}	[deg]	glide slope during approach
γ_{Climb}	[deg]	climb angle during climb phase
λ	[-]	constant coefficient for mass estimation of mechanism
Λ	[-]	aspect ratio
μ_r	[-]	friction coefficient
ω	[-]	number of vector loop equations
ϕ	[deg]	angle within the mechanism (change during deployment)
Φ	[-]	number of links in mechanism
ρ	[kg/m^3]	density
χ	[-]	number of elements in mechanism
Ψ	[-]	vector loop equation
$\vec{\Psi}$		system of vector loop equations

Subscripts

2D	two-dimensional
2.5D	infinitely swept wing
3D	three-dimensional
app	approach during landing
B	beam
climb	climb during take-off
clean	clean
CA	carriage
GR	ground-roll
Flap	flap related
Ldg	landing
max	maximum
loc	local
obj	objective
RA	rotary actuator
rev	reverse
Slat	slat related
stall	stall condition
TO	take-off
tot	total condition
trans	transition
quasi, 3D	quasi three-dimensional
∞	freestream condition

Acronyms and Abbreviations

ACARE	**A**dvisory **C**ouncil for **A**eronautics **R**esearch in **E**urope and **N**oise control on n**ext** generation wing
AIAA	**A**merican **I**nstitute of **A**eronautics and **A**stronautics
CFD	**C**omputational **F**luid **D**ynamics
CFR	**C**ode of **F**ederal **R**egulations
CRM	**C**ommon **R**esearch **M**odel
DeSiReH	**De**sign, **Si**mulation and Flight **Re**ynolds Number testing for advanced **H**igh Lift Solution
DLR	**D**eutsches Zentrum für **L**uft- und **R**aumfahrt (German Aerospace Center)
DOC	**D**irect **O**perating **C**osts
EUROLIFT	**EURO**pean high **LIFT** program
FAA	**F**ederal **A**viation **A**dministration
FAR	**F**ederal **A**irworthiness **R**egulations
HINVA	**H**igh lift **IN**flight **VA**lidation
HLFC	**H**ybrid **L**aminar **F**low **C**ontrol
MLW	**M**aximum **L**anding **W**eight
MOVE.ON	**MOV**able d**E**sign and **O**ptimisation of performance and low **N**oise
MTOW	**M**aximum **T**ake-**O**ff **W**eight
RANS	**R**eynolds **A**veraged **N**avier **S**tokes
RSM	**R**esponse **S**urface **M**ethod
TEFlaMeS	**T**railing **E**dge **Fla**p **Me**chanism **S**ynthesis
VDI	**V**erein **D**eutscher **I**ngenieure

"progress is achieved
in a series of incremental steps."[1]

[1] Baker [1] page 30

1 Introduction

1.1 General Aspects of High-Lift Systems

Why High-Lift Systems? Most of the times, during the flight of a commercial aircraft, high-lift devices are retracted. Only during short periods of take-off and landing these elements are used. In the first place, the necessity of high-lift systems on commercial airliners will be discussed. Second, the economics of high-lift systems in the context of a whole aircraft will be taken into account. Let's have a look at the design of the high-lift systems and how they affect the total aircraft performance, although they are only applied during short periods of the flight. Based on these considerations, the reasons that make aircraft designers spend much effort on the high-lift system will be regarded.

The **Necessity of the High-Lift System** on commercial airliners originates from the strongly different air speeds between cruise and low speed phases, namely, take-off and landing. The wing of the aircraft, designed to be beneficial for cruise, is not able to generate enough lift in these low speed phases. A short but emphatic example is given by v. Dam [2], where a typical commercial aircraft is considered. He shows that the classical configuration is not able to generate enough lift during take-off and landing without a high-lift system. He further compares this typical commercial aircraft with an aircraft B with enlarged wing area. Aircraft B does not require a high-lift system, due to the enlarged wing area. However, the cruise performance ($\mathrm{Ma}_\infty C_L/C_D$) is reduced due to a smaller lift coefficient at cruise. He assumes that the drag characteristics for both airplanes are constant.

Now let's take the second question into account, w.r.t. the **Economics of High-Lift Systems.** Is the generation of enough lift during the low speed phases the only challenge of the high-lift system? This is indeed not the case. The design of a high-lift system is crucial for the economic success of a commercial airplane. Although the high-lift system is only applied during take-off and landing in the low speed phase of the flight, the cost efficiency of the airplane is strongly influenced by it. The aerodynamic performance of the high-lift system during take-off and landing is estimated for a generic twin engine aircraft by Meredith [3]. Meredith presents simple *"trade factors derived for a generic large twin engine transport"*.[1] In this publication, estimations have been presented on how increased lift coefficient, maximum lift coefficient and lift-to-drag ratio affect the airplane in terms of weight savings or increased payload. In 1984 Butter [4] gave assumptions on how maximum lift for take-off, landing and lift-to-drag for take-off effect the payload capacity of a large twin engined aircraft.

Van Dam [2] also gives statements regarding the economics of high-lift systems. *"Multi-element high-lift systems have a significant impact on the cost of a typical jet transport because (i) they are time consuming to design and test, (ii) their flows, geometry, and actuation and support systems are complex, (iii) they are heavy, (iv) have a high part count, and (v) are maintenance*

[1] Meredith [3] page 19-1

intensive."[2]
According to Rudolph [5] the high-lift system of a typical jet transporter accounts for about 6-11% of the total production cost. Rudolph further explains the importance of take-off lift-to-drag ratio and maximum lift coefficient for landing. According to him, the main issue is the lift-to-drag ratio for the take-off. A small reduction in the maximum lift coefficient for landing can be acceptable if therewith a gain in lift-to-drag ratio for take-off is obtained. Garner et al. [6] states, that high-lift systems are *"a necessity for commercial transport aircraft,"*[3] but they *"add cost, complexity, and weight to the airplane"*[3]. Additionally, Garner states that the aim of the designer is to *"meet airplane take-off and landing requirements while keeping the high-lift system as simple as possible"*[3]. Rogers et al. [7] affirm: *"Increases in lift coefficient CL and in lift-over-drag can lead to a simpler high-lift system, resulting in less weight and less noise, as well as increases in both payload and range."*[4]

Tendencies of High-Lift Systems:
Rudolph [5] describes in his publication the trends in the high-lift system design over the last decades. Until the 1970s *"high-lift systems increased in complexity and reached peak sophistication with triple-slotted, trailing-edge flaps on the Boeing 727, 737, and 747"*[5]. After that peak, a decrease in complexity is recognizable. Rudolph explains that this decay, by optimized aerodynamic shapes and optimized positions of the elements of the high-lift system, was possible due to *"refinement of computational fluid mechanics technology"*[5] and with *"more powerful computers"*[5]. These tendencies are recognizable both for Boeing and above all for Airbus. Although the complexity is decreased, the aerodynamic performance of the high-lift system could be preserved. In the case of Airbus, even a gain is noticeable for the take-off. Reckzeh [8] states: *"Single-Slotted Flap driven on Track-kinematics as trailing edge solution became the Airbus standard solution from A320 up to A380."*[6] Concerning dropped-hinge kinematics Reckzeh affirms: *"While being beneficial for complexity and weight the solution is far from being optimum for the aerodynamics design freedom and therefore detrimental to an unconstrained optimized performance."*[7] In the course of the design of the Boeing 787 and Airbus A350, the complexity has reached a minimum so far since both airplanes are equipped with a rather simple hinge mechanism for the flap with a gap control through spoiler droop. The advantages of the spoiler droop technique are already described by Rudolph [5] in 1996. Dillner et al. [9] stated in 1984 w.r.t. high-lift systems that *"the strongest bias must be in favor of simplicity".*[8]
In this context, the Fowler motion of the flap has to be mentioned. *"Fowler motion denotes the aft motion of the flaps during deployment resulting in increased planform and, hence, lift."*[9] A beneficial, *"'smart' flap mechanism provides most of the available Fowler motion in the initial flap deployment at low deflection angles."*[10]

Environmental Issues and Future Demands for Aircraft:
Future demands and targets for the aircraft sector in Europe are formulated in the "Vision 2020" [10]. This vision defines targets for a new aircraft of 2020 which should achieve a

[2] van Dam [2] page 103
[3] Garner et al. [6] page 14
[4] Rogers et al. [7] page 425
[5] Rudolph [5] page 117
[6] Reckzeh [8] page 3
[7] Reckzeh [8] page 5
[8] Dillner et al. [9] page 9.4
[9] van Dam [2] page 110
[10] Rudolph [5] page 27

"50% cut in CO_2 emissions per passenger kilometer (which means a 50% cut in fuel consumption ...) and an 80% cut in nitrogen oxide emissions"[11] compared to a new aircraft in 2000. Further on, a demand for the aircraft industry is to *"halve the 'time to market' for new products with the help of advanced electronic analytical, design, manufacturing and maintenance tools, methods and processes."*[12] In addition, the average accident rate is targeted to be drastically reduced (*"five-fold reduction"*[13]) in 2020.
"Flightpath 2050" [11] is the current vision that follows the "Vision 2020" and was published in 2011. It describes more demanding targets that are thought to be realized in a longer time period. The main targets of the "Vision 2020" concerning CO_2, nitrogen oxide emissions are reformulated in the "Flightpath 2050", but with more drastical reductions (CO_2 75% and NOx 90% compared to a *"typical new aircraft in 2000"*[14]). Besides these targets, the vision includes statements concerning the application of multidisciplinary design which is *"used routinely ... to support a high level of integrated system design"*[15].
Therewith future demands are defined not only to preserve the environment but also to keep *"technological leadership"*[16] in the aircraft sector. These facts incorporate that design processes comprise aspects of multiple disciplines to achieve a high level of technology/breakthrough technologies, in order to decrease the turn-around cycle for the design of aircraft dramatically. In the end, only by innovations and by technologically advanced airplanes, industry can serve the economical market and achieve the ambitious environmental objectives. *"This is not only a matter of success but also of survival."*[16]

Safety Issues for High-Lift Systems:
Besides economics, safety is one of the major issues in aerospace industry. As already mentioned, the "Vision 2020" takes safety as a top priority and in "Flightpath 2050" it is claimed that *"in 2050, European aviation has achieved unprecedented level of safety and continues to improve"*[17].
Investigations on flight accidents during approach revealed that landing accident rate correlates with approach speed, refer to Rudolph [5], Dillner et al. [9], Flaig et al. [12] and see Figure 1. Dillner states: *"approach speed has a value in itself, not only as a performance variable, but as an important safety factor."*[18] Airplane manufacturers are encouraged to design high-lift systems with a high performance to be competitive in the international aerospace market and to satisfy the aerospace safety standards. Performance indicators are, for example, the required take-off and landing distance, which are directly linked to the aerodynamic performance of the wing.

1.2 State-of-the-Art

Aerodynamics of High-Lift Systems: The real understanding of the aerodynamics of multi-element airfoils goes back to the work of A.M.O. Smith [13] in 1975. This fundamental work entitled "High-Lift Aerodynamics" presents in detail the principles that trigger the aerody-

[11] "Vision 2020" [10] page 14, CO_2 = carbon dioxide, NOx = nitrogen oxide
[12] "Vision 2020" [10] page 15
[13] "Vision 2020" [10] page 14
[14] "Flightpath 2050" [11] page 15
[15] "Flightpath 2050" [11] page 12
[16] "Flightpath 2050" [11] page 6
[17] "Flightpath 2050" [11] page 16
[18] Dillner et al. [9] page 9-3

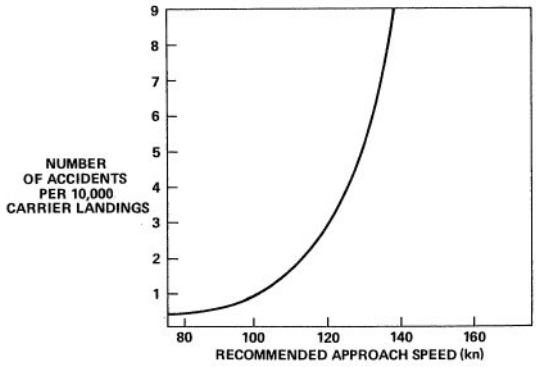

Figure 1: Influence of aircraft approach speed on carrier-landing accidents; source Dillner et al. [9].

namics of high-lift devices w.r.t. gaps. Smith defines five primary effects of gaps, namely slat effect, circulation effect, dumping effect, off-the-surface pressure recovery and fresh-boundary-layer effect. Garner et al. [6] discuss inter alia *"Scale Effects on High-Lift Systems"* i.e. Reynolds Number effects, *"Relaminarisation"* and *"Viscous Wake Interactions"*. Over the last decades high-lift aerodynamics became a common research field for experimental [14–16] and numerical studies [17–19]. Publications concerning numerical studies with wind tunnel verification are presented e.g. by Eliasson [20], Schindler et al. [21] and Rumsey et al. [22, 23]. Rumsey summarizes the outcome of the first and second "High-Lift Prediction Workshop"of the American Institute of Aeronautics and Astronautics (AIAA). Rogers at al. [7] investigate numerically the aerodynamics of the Boeing B777 in its landing configuration and compare the results with wind tunnel data. The capabilities of numerical methods concerning the aerodynamic performance of high-lift devices are reviewed by Rumsey [24].
Recently in the German national project HINVA, the maximum lift capability of an Airbus A320 was studied by flight tests [25, 26], numerical computations [27] and a wind tunnel campaign [28]. An overview of the project in an early state was given by Rudnik [29]. The project was conducted first to generate broad validation data from the different approaches (flight test, wind tunnel, numerics), and second according to Rudnik *"to significantly enhance the accuracy and reliability of the prediction and assessment of the aerodynamic performance of civil aircraft with deployed high-lift devices"*[19].
In a recent publication of Wild [30] a broad overview of research topics in the scope of high-lift aerodynamics are presented. This publication summarizes topics which were investigated recently at the Institute of Aerodynamics and Flow Technology of the German Aerospace Center (DLR) in national and international collaborations. This publication covers among others, high-lift aerodynamics for wings with laminar flow during cruise and flow control to avoid separations during high-lift by active systems.
High-Lift Design in Industrial Context: Dillner et al. [9] present in their publication design aspects of high-lift systems. The *"design is generally optimized first and foremost for cruise efficiency. The objective of the complementary high-lift design effort is to produce a system which will allow a cruise optimized configuration to adequately meet take-off and landing requirement safely and reliably."*[20] From the perspective of an airplane designer, Reckzeh [31] describes the design process, its challenges and constraints for the high-lift system within the multidisciplinary context of the development of a megaliner aircraft. In a further publication [8] he describes

[19]Rudnik et al. [29] page 1
[20]Dillner et al. [9] page 9-2

the design requirements for the military transport aircraft Airbus A400M with a focus on the aerodynamics of the high-lift system and the special requirements that arise from military missions. The design of the high-lift system of the Airbus A321 is described by Flaig et al. [12]. From the perspective of Boeing, Nield [32] presents an overview of the aerodynamic design of the Boeing B777's high-lift system. Kafyeke et al. [33] show the design of the high-lift system of the Bombardier CRJ-700 and show results from wind tunnel, numerics and flight test. In the context of the AIAA high-lift prediction workshop, a high-lift common research model is designed by Lacy et al. [34] from Boeing. The model is developed based on a high-speed wing, however some adaptations were done to improve the high-lift suitability. The model is available for research. For validation purposes wind tunnel measurements are planned.

Mechanisms for High-Lift Systems: Mechanisms to deploy high-lift systems are reviewed and described in detail by Rudolph [5]. This compilation not only comprises the concepts but also gives many examples from commercial airplanes. Additionally, Niu [35] and v. Dam [2] give an overview of used types of mechanisms on commercial aircraft.

Nowadays high-lift research additionally deals with mono- and multidisciplinary optimization.

Aerodynamic Setting/Shape Optimization of High-Lift Systems: Early works in this context are from Eyi et al. [36] and Besnard et al. [37]. Eyi et al. are pioneers since they used first a Navier-Stokes method to simulate the aerodynamics, whereas Besnard et al. used an interactive boundary layer approach. Aerodynamic shape and setting optimization based on Navier-Stokes methods is demonstrated by Wild [38, 39], Nemec et al. [40], Benini et al. [41], Carrese et al. [42] and are addressed within e.g. the European projects DeSiReH by Benini et al. [43], Iannelli et al. [44] and EUROLIFT II by Brezillon et al. [45] and Wild et al. [46]. Within EUROLIFT II a wind tunnel campaign was conducted to verify the achievements of the optimized shapes and settings [47].

New demands arise for the leading-edge high-lift system, when laminar flow on the wing during cruise is desired. Moens and Dandois [48] research in the laminar context a slatless high-lift configuration, for which mechanical vortex generators (position, shape) and flap setting are simultaneously optimized. A previous publication of the author et al. [49] presents the aerodynamic shape and setting design of a Krüger device in the context of hybrid laminar flow control (HLFC). Here, special attention is laid on the investigation of the correlation of size and aerodynamic high-lift performance of the Krüger. Realistic boundary conditions w.r.t. mechanism and systems for the suction system to ensure hybrid laminar flow are accounted in this work.

Multidisciplinary Aspects of High-Lift Systems: Multidisciplinarity regarding high-lift systems is taken into account by v. Dam et al. [50], Takenaka and Nakahashi [51], Kolla et al. [52], Holert [53, 54], and Kintscher et al. [55]. V. Dam, Takenaka and Kolla deal with the aerodynamic optimization of high-lift systems under consideration of the flap mechanism. V. Dam optimizes the aero-mechanical system while analyzing the flap mechanism and taking the aerodynamic performance from a pre-computed aerodynamic database. Takenaka investigates the trade-off between aerodynamics and kinematics with a genetic optimization algorithm for the take-off configuration. Kolla optimizes the shape of the flap in landing configuration while fulfilling a stowability constraint. Holert presents in his publications a framework to optimize the mechanism of the flap to achieve a system that meets various pre-defined flap settings that originate from an aerodynamic setting optimization. The framework is able to optimize the flap mechanism w.r.t. e.g. its mass, the accuracy of the target flap settings and gap convergence. Further on, it can deal with limitations in the installation space. Kintscher et al. focus on the pre-design and sizing of a droop nose leading

edge device and its deployment mechanism. The shape of the droop nose is optimized from the aerodynamic perspective. Later on, the design of the mechanism and the skin thickness distribution is optimized to meet structural demands and the aerodynamically optimized shapes.
Pepper et al. [56] present in their publication simple relationships to estimate the mass of a slat and flap mechanism for the use within an optimization framework based on existing aircraft. Furthermore, the influence of the mechanisms on the direct operating costs (DOC) is roughly estimated in this publication.
Recently, in 2016, Zaccai et al. [57] present in their publication a multidisciplinary methodology to design single slotted trailing edge high-lift systems. This publication puts a clear focus on the simulation of the flap high-lift mechanism. The novum in this work is, that it covers three-dimensional flap kinematics. Additionally, the flap mechanism is structurally sized, that leads to a system mass approximation and on power assumption. The aerodynamic load generation relies on handbook methods, semi-empirical methods. Based on the implemented design process a three-dimensional trailing edge high-lift system can be "automatically synthesized and sized based on kinematics, aerodynamics and mechanical requirements."[21]
Meredith [3] gives preliminary assumptions on the influence of the aerodynamic performance of the high-lift system on the overall aircraft.
From a flight mechanics' perspective in conjunction with noise abatement at low-speeds Kreth [58] investigates flight procedures during take-off and landing for a simulation model of the Boeing B747. The aerodynamic coefficients are taken from tables.
In a previous publication, published 2010, the author [59] focuses on the aero-mechanical setting optimization of the flap. The flap trajectory path is calculated and analyzed to ensure a clash free deployment of the flap for the optimized aero-mechanical system. It is shown that a sequential approach to optimize the flap setting, first by an aerodynamic and then by a kinematic optimization, is unfavorable compared to a coupled, dualdisciplinary optimization. This publication is a pre-study for this thesis.
The author [60] presents in a further publication in 2012 a multidisciplinary approach to design a generic high-lift system. This publication was published within the scope of this thesis. Besides the aerodynamics and kinematics, the flight mechanics are considered in the design loop. The relationships w.r.t. the flight mechanics are accounted for to weight the aerodynamic coefficients in a realistic manner by an approximation of the take-off and landing distance and are used as performance indicators. The work shows a successful multidisciplinary proof-of-concept optimization of the generic high-lift system at take-off and landing. The distances for both phases of the optimization problem, i.e. for take-off and landing, are reduced while the constraints are satisfied.
Aerodynamic evaluations of a three dimensional high-lift configuration where kinematics relationships are considered for the deployment of the slat and flap elements are presented by the author [61] in 2015. Additionally, take-off and landing performance are evaluated with a preliminary design tool based on the high-fidelity aerodynamic data base and according to Federal Aviation Regulations (FARs) by the Federal Aviation Administration (FAA). This treatment of the flight mechanics is highly elaborated, since for take-off and landing next to the balanced field length also the approach climb, landing climb, one engine inoperative conditions are evaluated. The interest of this work lies in off-design, meaning variation of the airport elevation, temperature and mass of the aircraft for take-off and landing. These scenarios are studied to derive optimal settings for the high-lift system. This work evolved

[21] Zaccai et al. [57] page 522

from the German national project MOVE.ON.

1.3 Motivation, Objectives and Delimitation

Monodisciplinary aerodynamic shape and setting optimization are well investigated, widely applied and show a high potential to improve the aerodynamic performance of a high-lift system. The consequent next step should be the consideration of the design task as a multidisciplinary issue.
This work is motivated by the interest in the mutual influence of disciplines involved in the design process of a favorable high-lift system. The objectives of this thesis are to study how the single disciplines affect the final design, how the disciplines interact, and until which extent there is any benefit in a highly elaborated multidisciplinary optimization, i.e. a wholistic approach, in contrast to a sequence of monodisciplinary optimizations.
Within this work, kinematics, aerodynamics, mass estimation and flight mechanics are taken as disciplines to study the high-lift system from a multidisciplinary point of view which are motivated as follows:

- **Aerodynamics** is the core discipline and starting point from former works.
- **Kinematics** gives a realistic relationship between the settings for take-off and landing for the slat and flap respectively.
- The **Mass estimation** of the high-lift mechanisms is used to consider the fact that different aerodynamic loads result in varied mass of the components. The aerodynamic loads differ due to the variation of the geometry of the mechanism and the flap/slat setting.
- **Flight mechanics** is used as a performance indicator. This discipline enables the combination of the aerodynamic coefficients for ground-roll, climb and approach in a realistic manner and to consider the variation of the mass of the mechanisms by the change of the overall airplane mass.

The interaction of structure and aerodynamics for high-lift elements is already investigated widely, e.g. by Drews [62], Keye [63] and can be seen as state-of-the-art. Throughout this work the shape of the high-lift airfoil is kept constant, i.e. the optimizations performed are related to aerodynamic setting optimizations. Therewith the locations of the front and rear spar are not adapted within this thesis and consequently the available fuel tank volume and the mass of the main-wing structure are constant. The structural composition of the flap and slat are constant throughout this work. These aspects are favorable to neglect the interaction of structure and aerodynamics for the high-lift design in this thesis. Hence, for this work this discipline is excluded and no sizing of the structure of the high-lift elements is foreseen.
To study the interrelation of the disciplines of the multidisciplinary high-lift design the following tasks have to be conducted:

1. Development and implementation of up to now missing tools to fit within an automated process chain (kinematics simulation of the mechanism for the flap, mass estimation tool, flight mechanics tool).

2. Development and implementation of an adaptable process chain to enable optimizations ranging from monodisciplinary aerodynamic setting optimization to multidisciplinary optimization of the high-lift system in a wholistic manner.

3. Accomplishment of optimizations with a different number of involved disciplines to study the influence of the single disciplines on the final design.

4. Evaluation of the benefits/drawbacks of multidisciplinary design in contrast to a sequence of mono- and dual disciplinary approaches.

In this work the focus is on one type of slat and flap mechanism, namely constant radius track for the slat and a track-linkage mechanism for the single slotted flap. The track-linkage system is *"Airbus standard solution from A320 up to A380"*[22] and *"the track type kinematics offer more design freedom to realize the optimum relation between flap Fowler movement and flap deflection"*[23]. The complexity of the configuration is limited to two-dimensional airfoils. Conversion of the two-dimensional data is done to approximate the aerodynamic coefficients for the wing of the assumed aircraft. By these coefficients the take-off and landing distances are estimated. The influence of the varied high-lift system on the cruise performance is not covered in this work. However, as the cruise wing in its shape and performance is not adapted the influence on the cruise performance is considered to be very small. The focus is laid on the trailing edge mechanism.

1.4 Overview and Structure of this Work

In Chapter 1 a general introduction to high-lift systems has been given. Additionally state-of-the-art, motivation, objectives and delimitation are presented.
Chapter 2 gives a background to optimization, describes the parameterization of the high-lift system and explains in detail the methodologies of the individual disciplines.
In Chapter 3 the results of variants of possible optimization approaches are presented and discussed. The starting point of this work is monodisciplinary aerodynamic setting optimization, where the objective function is based on flight mechanical relationships. Then the kinematics relationship derived for the flap mechanism is added to simulate the deployment of flap, which results in feasible flap settings. A further step regards the mass of the mechanisms to deploy the slat and the flap that changes due to the variations in the aerodynamic loads on both the flap and the slat. The results are examined in detail in this chapter from the perspective of each discipline involved in the design process.
The thesis closes with the conclusions and an outlook on possible future activities, referred to in Chapter 4.

[22] Reckzeh [8] page 3
[23] Flaig [12] page 31-4

2 Methodology

In this chapter the disciplines and corresponding tools that are involved in the various mono- and multidisciplinary design approaches are discussed. The chapter is structured as follows. A general description of optimization, objectives, constraints and algorithms is given at first. Then the test case used within this thesis is described and the process chains for the optimization are detailed. In the following the parameterization of the high-lift system and the disciplines based on which the high-lift system is analyzed within the optimization cycles are presented.

2.1 Optimization

The following section is based on the textbook "Numerical Optimization" by Nocedal and Wright [64].
The basic idea of optimization is to find a set of parameters which minimize a given objective function with respect to constraints. Next to the given constraints the system restricts the parameters. The optimization problem is solved by applying an appropriate optimization algorithm ranging from non-deterministic up to deterministic gradient-free or gradient-based algorithms. The fundamental expression for a multi-objective constraint optimization problem reads:

$$\begin{aligned} &\min\ f_i(\vec{x}),\ \ \vec{x} \in R^n, i = 1, \ldots, h \\ &\vdots \\ &\text{subject to} \\ &g_j(\vec{x}) = 0,\ \ j = 1, \ldots, m_e \\ &g_j(\vec{x}) \geq 0,\ \ j = m_e + 1, \ldots, m_c \\ &x_{l,k} \leq x_k \leq x_{u,k}, k = 1, \ldots, n \end{aligned} \tag{2.1}$$

where $\vec{x}$ is the vector of design variables[1] with the dimension n that are optimized. $f_i(\vec{x})$ are the objective functions and $g_j(\vec{x})$ are the equality and inequality constraints. Parameters or design variables $\vec{x}$ may be restricted by upper x_u and lower x_l bounds.
The standard form of optimization is a minimization problem with equality and inequality constraints. Furthermore the parameters may be bounded. Unrestricted design variables or parameters that do not have any upper and lower bound are free variables and free parameters, respectively.
When dealing with multi-objective optimization problems the term Pareto front comes into play. For the definition of the **Pareto front** we follow Trapani et al. [65] who state: *"a solution is Pareto optimal if no other feasible solution exists which would simultaneously improve all of*

[1]Note: the terms parameter, design variable and design parameter are used equivalently in this work.

the objective functions. The set of all the solutions that satisfy this requirement is defined as Pareto optimal set and consists of all the non-dominated solutions. The corresponding objective functions representation is instead defined Pareto Front".[2] The shape of the Pareto front defines the character of the trade-off between multiple objective functions.
In many practical cases it is useful to simplify the optimization problem since many optimization algorithms were originally designed for unconstrained single-objective optimization problems. The multi-objective optimization problem can be transferred into a single-objective optimization problem by taking into account the weighted sum of the single objectives. The resulting single-objective optimization problem reads:

$$\begin{aligned} &\min\ F(\vec{x}),\ \ \vec{x} \in R^n, \\ &F(\vec{x}) = \sum_{i=1}^{h} w_i \cdot f_i(\vec{x}), \end{aligned} \tag{2.2}$$

where the w_i are the weights of the corresponding objectives $f_i(\vec{x})$.
Before starting the optimization the user has to specify the weights w_i which have a significant influence on the final result. The weights of the single objectives define the slope of the line with constant objective function values, refer to Figure 2. The Pareto front is indicated

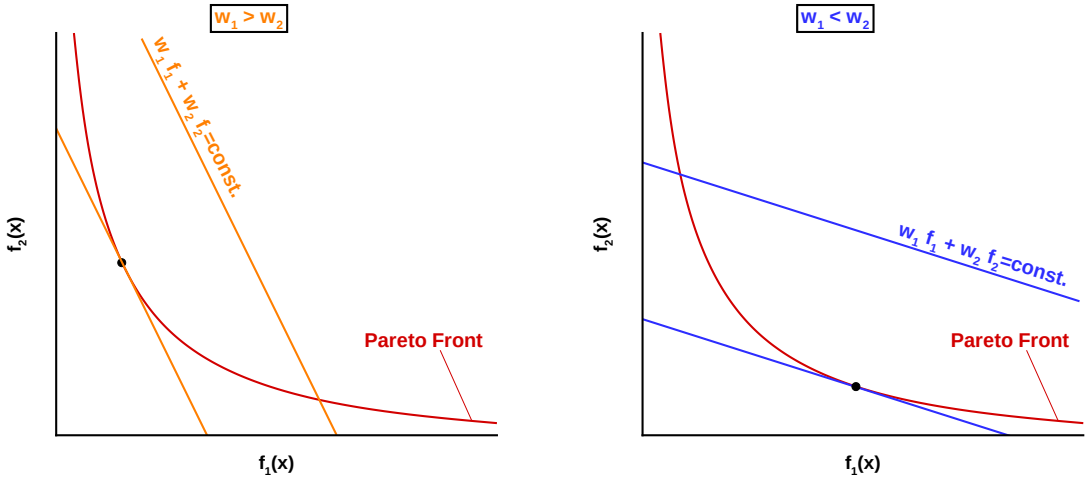

Figure 2: Influence of the weights on the optimal design for a given dual-objective optimization problem with a convex Pareto front.

by a curve. The optimal sample is indicated by a symbol on the Pareto front.
A technique to remove constraints from the optimization problem is known as the "penalty method". This is a simple approach as it penalizes the violation of the constraints by adding a penalty term to the objective function value. By applying this method a constrained optimization problem can be solved by an optimization algorithm dedicated to unconstrained problems.

2.1.1 Optimization Algorithm

The basic task of optimization algorithms is to find the global optimum (minimum or maximum) of the objective functions with a high precision w.r.t. the constraints and the

[2] Trapani et al. [65] page 122

feasible domain of the parameters. This task is meant to be achieved with a small number of function evaluations and independently of the initial starting point. To conclude the requirements, optimization strategies should be robust, accurate and efficient.

Robustness means that the algorithm detects the domain of the global optimum on various optimization problems for all initial sets of variables that are reasonable.
Accuracy means that a solution of the optimization problem is identified with high precision without being overly sensitive to errors in the data or round-off errors.
Efficiency means that usage of computer resources and time stays in reasonable bounds.

As described above, optimization problems can be distinguished based on their mathematical behavior. For each class of optimization problems, suitable optimization algorithms are developed. Further on, optimization algorithms can be distinguished between non-deterministic and deterministic gradient-free/gradient-based strategies. One example for non-deterministic optimization algorithms are evolutionary strategies. They are related to the analogy of natural evolution of species. Natural selection and reproduction guide the evolution towards individuals that are better adapted to the environment. This kind of algorithm is suited to detect the domain of the global extremum of the optimization problem with a high probability but it has a very slow convergence rate. Deterministic algorithms have a faster convergence rate and detect optima with a higher precision. But generally they lack the ability to detect the global extremum with a high probability, i.e. these kind of algorithms are less robust. Especially, gradient-based optimization algorithms are very fast in detecting the nearest optimum with a high precision, i.e. they are efficient and accurate but not robust.
In this work the deterministic, gradient-free optimization algorithm Subplex is used. The algorithm is developed by Rowan [66] and is basically a generalization of the Nelder-Mead Simplex [67] method. The idea of the Subplex strategy is *"to remove the weaknesses of the simplex method and to retain the positive features"*[3]. The weakness of the Simplex method is the loss of efficiency when increasing the number of design parameter, i.e. for $n \geq 5$. Whereas the positive features are firstly, a good convergence rate, i.e. the algorithm is able to solve optimization problems with a small number of function evaluations and secondly, the ability to handle noisy functions. The Subplex method works by a decomposition of the optimization problem into low-dimensional subspaces. These subspaces are searched by the Simplex method which is very efficient for low-dimensional problems.
Wild [38] shows that the Subplex algorithm is suitable for aerodynamic high-lift optimization problems. Further on, this work indicates that the tools (computational fluid dynamics (CFD)) used in the field of prediction of aerodynamic flows of high-lift systems are sensitive enough to assess properly small surface and setting variations. This was proven by numerical optimization that detects with a reasonable accuracy the optimum which was determined by an experimental optimization during a wind tunnel campaign. Wild [38] and Wikman et al. [68] confirm the ability of the Subplex algorithm to be able to handle noisy functions and to show a good convergence behavior against strongly different sensitivities of the parameters. The Simplex and the Subplex method are both designed for unconstrained optimization problems. As described above, in this thesis the weighted sum and the penalty methods are applied to transform the constrained multi-objective optimization problem into an unconstrained single-objective optimization problem.

[3] Rowan [66] page 63

2.1.2 Optimization Framework

The used optimization framework PYRANHA [69, 70] is developed at DLR. It offers optimization algorithms ranging from non-deterministic strategies to gradient-based and gradient-free strategies including the afore mentioned Subplex algorithm.
The optimization framework controls the optimization process and provides the user with strategies to solve a given problem. A process chain that reflects the optimization problem and its processes has to be implemented. The optimization framework is provided with the number and domains of the parameters, the objective function value and values for the constraints. Additionally if needed, the gradients of the objective and the constraints w.r.t. the parameters are supplied. The process chain is a black box for the optimization framework. The optimization algorithm decides based on the relation of the set of parameters and the corresponding function values of the objective and the constraints of the current and the former evaluations about the new set of the parameters for the next design. This design will be evaluated next. This procedure will be repeated until the convergence criteria of the optimization strategy will be satisfied and the minimum of the optimization problem will be detected with a high precision.

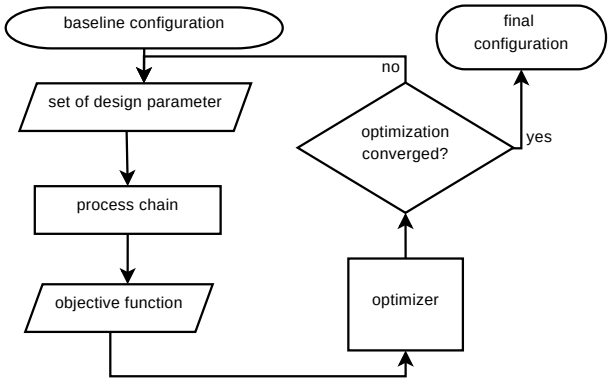

Figure 3: Flow chart of the optimization procedure.

Figure 3 depicts the flow chart of an optimization problem. It is an unconstrained, deterministic and gradient-free optimization with one single objective function.

2.2 Test Case

As test case, the geometry of a three-element airfoil provided by industry is taken. The airfoil has a slat with a chord length of $c_{\text{Slat}} = 13.5\% c_{\text{clean}}$ and a flap with a chord length of $c_{\text{Flap}} = 24.5\% c_{\text{clean}}$. From the perspective of the kinematics, we regard a constant radius track for the slat mechanism with a fixed hinge point, refer to Figure 4. This system is actuated by a rotary actuator (pinion drive). The rollers guide the constant radius track. The slat element is mounted on the track at the track head. This type of mechanism is the standard, state-of-the-art mechanism used for leading edge slats.
For the flap we consider a track-linkage system, see Figure 5, which is the *"Airbus standard solution"*[4]. This figure presents the main components of the track-linkage system. It has a rotary actuator, a drive strut, a carriage, a rear link and a beam to mount the system at the main element. The carriage can move on the track. The flap element can rotate around the

[4]Reckzeh [8] page 3

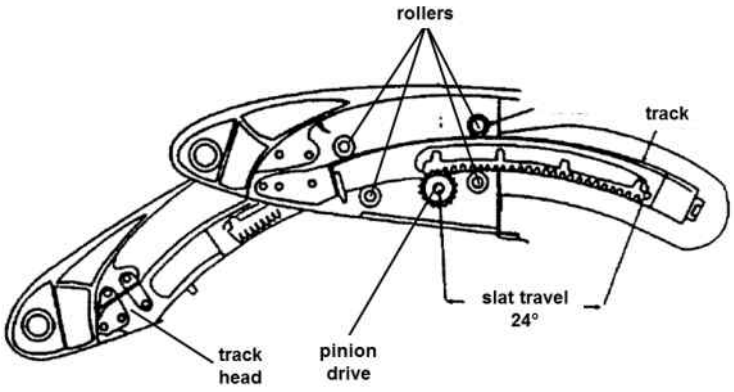

Figure 4: Illustration of a constant radius track for the slat of an Airbus A330/340; source: Rudolph [5].

axis where it is mounted on the carriage. The drive strut is mounted to the actuator and transmits the rotary actuation into the deployment of the flap mechanism. The rear link controls the flap deflection and is mounted at the rear part of the flap.
For the estimation of the take-off and landing distance we regard typical values for maximum take-off weight (MTOW), maximum landing weight (MLW), thrust, wing area, planform of the wing, etc. of a long-range transport aircraft, refer to Jenkinson et al. [71]. Additionally these data source is used to approximate the flow conditions for the test case. Based

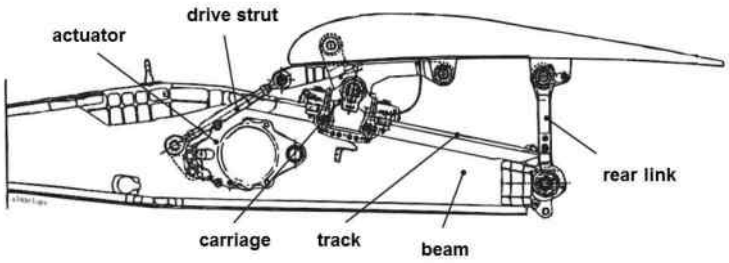

Figure 5: Sketch of a track-linkage system of an Airbus A340; source: Holert [72].

on these data (approach, climb speed) the stall, lift-off and touch-down speed are approximated w.r.t. to federal aviation regulations of the FAA (CFR 14 part 25 [73]) and handbook assumptions, see Table 1. The streamwise flow state conditions are summarized in Table 2

Table 1: Speed Regulations for a commercial airplane, according to federal aviation regulations CFR 14 part 25 of the FAA [73] and Raymer [74].

Take off:		
Climb	$v \geq 1.13 \cdot v_{\text{Stall, 1g, take-off}}$	[73]
Lift-off	$v \geq 1.1 \cdot v_{\text{Stall, 1g, take-off}}$	[74]
Landing:		
Approach	$v \geq 1.23 \cdot v_{\text{Stall, 1g, landing}}$	[73]
Touch down	$v \geq 1.15 \cdot v_{\text{Stall, 1g, landing}}$	[74]

for the spanwise position of the airfoil that is used within this work. For the fluid properties we consider the international standard atmosphere at sea level.

Table 2: Streamwise flow state conditions for the spanwise position of the high-lift airfoil that is considered in this work. The Reynolds number is based on the clean airfoil chord length for this spanwise position.

	Mach number [-]	Reynolds number [10^6]	Remark
Take off:			
Stall	0.251	40.6	$C_{\text{L,max}}$
Climb	0.284	45.9	$C_L = C_{\text{L,max,TO}}/1.13^2$
Ground-roll @ lift-off	0.276	44.7	$AoA = 0.0°$
Landing:			
Stall	0.186	30.0	$C_{\text{L,max}}$
Approach	0.229	36.9	$C_L = C_{\text{L,max,Ldg}}/1.23^2$
Ground-roll @ touch down	0.214	34.5	$AoA = 0.0°$

2.3 Process Chain

For the optimization of the high-lift system an adaptable process chain is set up. In the following, a brief overview of the modules used in the process chains is given. In detail, the modules are described in the subsequent sections. The process chains for the optimization approaches differ in the number of involved disciplines. The starting point is a monodisciplinary aerodynamic optimization in which the objective function is evaluated based on flight mechanical relationships. Finally, the most complex multidisciplinary optimization includes kinematics, aerodynamics, mass estimation and flight mechanics analysis of the high-lift system. Successively, the process chains for the optimizations will be described from the monodisciplinary to the most elaborated, multidisciplinary version.
The monodisciplinary process chain is illustrated in Figure 6-left. This process chain is used to optimize the take-off or the landing distance individually. Within the aerodynamic setting optimization the set of parameters define the setting for slat and flap. Based on the flap and slat setting the primary mesh to fill the computational domain is built with the mesh generator MegaCADs [75, 76]. The primary grid consists of cells that are related to the geometry. The flow simulation task includes the preprocessing and the execution of the flow solver, the DLR-TAU code [77].
In total, three CFD computations are performed. The maximum lift coefficient is evaluated. Further on the ground-roll condition is predicted. Depending on which scenario is optimized (take-off or landing) the climb or the approach condition is additionally computed. The postprocessing contains *inter alia* the extraction of the integral aerodynamic parameters for each flight condition. The aerodynamic integral coefficients obtained by the two-dimensional computations are converted in quasi three-dimensional coefficients, which account also for the estimation of the lift-induced-drag (refer to section 2.6). These coefficients are then used for the calculation of the take-off or landing distance. The take-off or landing

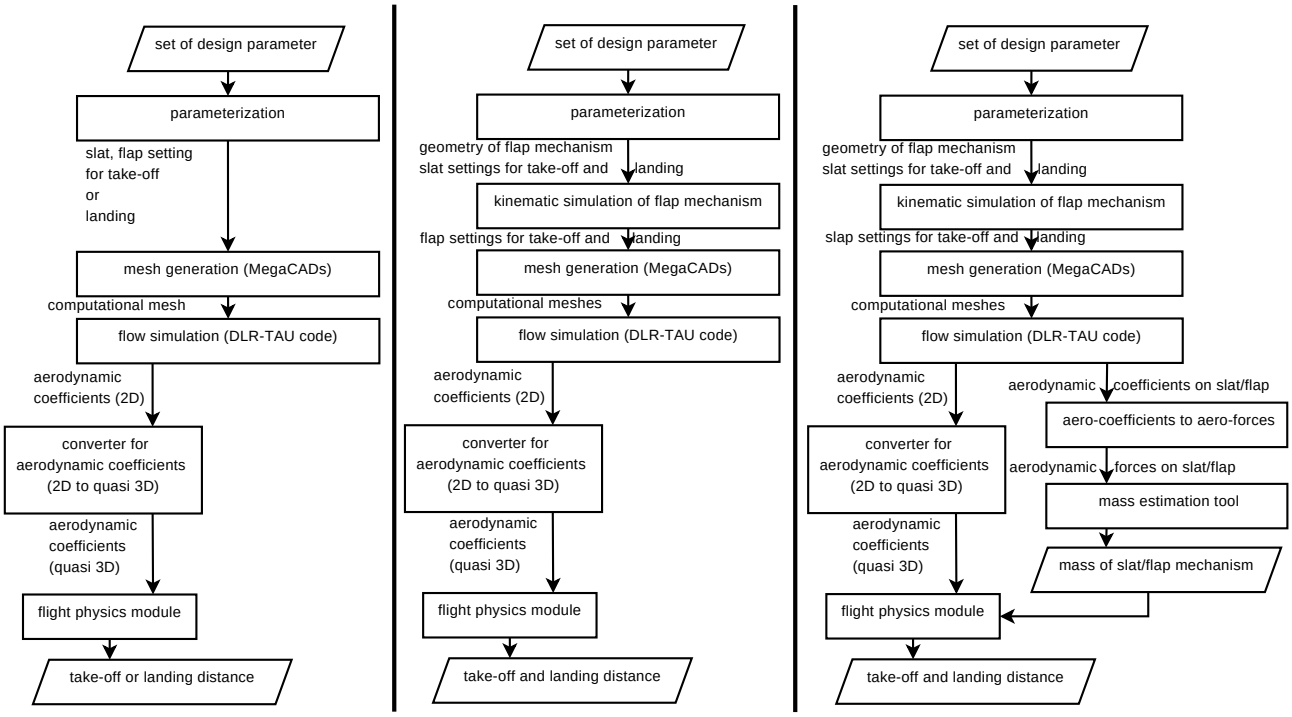

Figure 6: Flow chart of the process chain for the optimization of the high-lift system, where the objective function is evaluated based on flight mechanics relationships.
Left: aerodynamic optimization.
Center: multidisciplinary optimization which covers kinematics, aerodynamics and flight mechanics.
Right: multidisciplinary optimization which covers kinematics, aerodynamics, mass estimation of the high-lift mechanisms and flight mechanics.

distance form the function value of the objective function. MTOW and MLW are constant, respectively.
The next evolution of the process chain is illustrated in Figure 6-center. This process chain covers additionally a kinematics module. Therewith the parameterization changes. For this version the parameters define again the setting of the slat. Additionally, the geometry of the flap mechanism is defined by the parameters. The deployment of the flap is calculated based on kinematical relationships derived from the type of mechanism used here. The kinematics module provides then the settings for the flap during take-off and landing. For this approach the number of flow simulations is doubled to the previously described process chain, since the aerodynamics for both take-off and landing are evaluated for each design. This evolution of the process chain couples the take-off and the landing setting by the usage of the kinematics relationship. Hence, the take-off and landing cannot be optimized individually anymore, changes in the geometry of the mechanism affect the take-off and landing setting. The flight mechanics tool evaluates now both the take-off and landing distances, which form the function value of the objective function. The distances are equally weighted. Both, MTOW and MLW are constant.
The most elaborated version of the process chain is presented in Figure 6-right. This process chain covers next to the kinematics, aerodynamics and flight mechanics additionally a module to calculate the masses of the slat and flap mechanisms. The masses of the mechanisms to deploy the flap and the slat are calculated based on the aerodynamic loads acting on the slat and the flap element (refer to section 2.8). The global structure of the process is similar to

the one discussed before, but the process chain has additional quantities that are fed in the flight mechanics tool. The flight mechanics module depends in this version not only on the aerodynamic coefficients but it also considers the masses of the slat and flap mechanisms. By these the maximum take-off weight and the maximum landing weight are influenced. That means, the operational empty weight is affected by the weight of the mechanisms, whereas the weights for payload and fuel among others are constant throughout the work.

2.4 Kinematics

Kinematics is a subdiscipline of classical mechanics. Kinematics are related to the temporal and geometrical motion of points and bodies respectively. The origin of the motion, which are forces and moments, is not discussed in kinematics.
The discipline of the kinematics is applied in this work to evaluate the deployment of the flap w.r.t. a given mechanism. To describe the deployment-motion of a mechanism, the mechanism has to be transferred into a mathematical description. Two approaches are shortly described here. For the numerical analyses of the motion of planar gears, refer to text books [78, 79].
The first approach is based on modules which describe elements used within gears and is described in detail in the norm VDI-2729 [80] presented by the Verein Deutscher Ingenieure (VDI). This method describes the gear analytically and provides an exact solution of the motion.
The second approach is related to the formulation of vector-loop equations. These equations contain all information to describe the mechanism geometrically and include all known and unknown parameters. This method makes use of the condition that every vector-loop within a gear has to be closed and hence it has to be equal to the zero vector. A root-finding algorithm can be applied to solve the problem. Based on this vector-loop ansatz a Jacobian matrix is build which is characteristic for the gear, contains all relevant information of the gear in relation to its motion and reflects the unique relation between input (actuator position) and output (e.g. flap position) parameters of the gear. For a planar gear with one degree of freedom, χ elements and Φ links, the number of needed vector-loop equations ω is:

$$\omega = \Phi - (\chi - 1). \tag{2.3}$$

One planar vector-loop delivers two equations. In practical cases, where trigonometric functions are contained in the mathematical description of motion of the mechanism, the system of vector-loop equations is solved iteratively, since the vector-loop equations are non-linear and cannot be solved explicitly. A root-finding algorithm can be applied to receive the unknown parameters of the mechanism. One requirement to the vector-loops is that they contain every link and every element of the mechanism.
This work uses the formulation of vector-loop equations to describe the motion of the components of the mechanism. This method is simple to implement and is applicable on every system of gears. The method is fast if the variation of the input parameters is small and accurate. However it approximates the motion and does not provide the exact solution as the approach according to the norm VDI-2729. The vector-loop equations contain trigonometric relationships, that's why these equations are mostly not explicitly solvable. An iterative approach has to be applied to solve the system of equations and therewith the solution of the equations is not exact (e.g. truncation error). The Newton-Raphson root-finding method is implemented in this work to solve the non-linear system of vector-loop equations.

An already existing software TEFlaMeS [72] to simulate the flap deployment w.r.t. to a defined mechanism and to estimate the mass of the mechanism based on aerodynamic loads on the flap is used as a template within this thesis. The reason for not directly using this software is that it is unfortunately not applicable to an automatized optimization process chain. There exists only an interactive graphical user interface to control the software. However this software is very useful for the validation of the current developed approach, since much effort was spent by Holert [54, 72], the developer of TEFlaMeS, to validate this software with realistic configurations and it is based on the norm VDI-2729.

2.4.1 Kinematics Module

The utilization of the theory of the vector-loop approach is state-of-the-art in kinematics. However, for the particular application on a track-linkage system this approach needed to be adapted, implemented and validated by the author. In the following, a detail description is presented of the adapted and implemented approach to simulate the kinematics of a track-linkage mechanism.
For the description of the motion of the planar track-linkage system with five elements ($\chi = 5$) and eight links ($\Phi = 8$), four equations ($\omega = 4$) are needed according to Equation (2.3), i.e. two vector-loops. Figure 7 depicts the planar track-linkage flap mechanism. Additionally, the figure shows two possible vector-loops that are sufficient to describe the motion of this type of mechanism. In the following these vector-loops are described in detail and the method to solve the vector loops is presented.

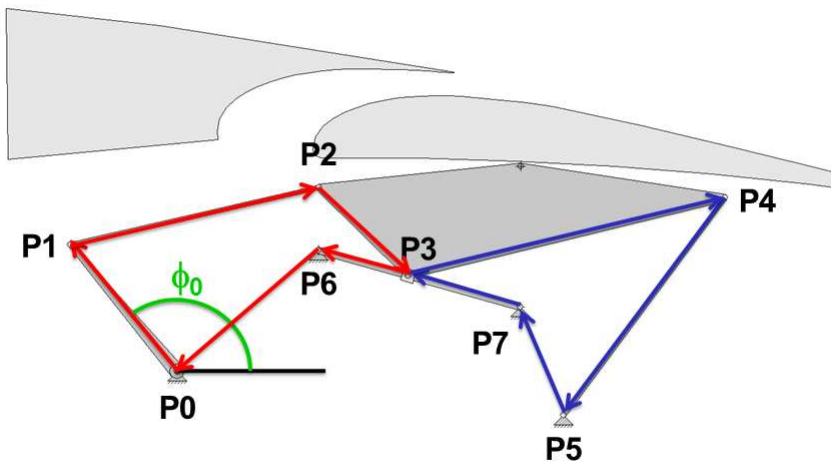

Figure 7: Sketch of a track-linkage system with the two implemented vector-loops. ϕ_0 is the angle at the actuator.

According to the figure the vector-loop equations for this type of mechanism read:

$$\vec{V_{01}} + \vec{V_{12}} + \vec{V_{23}} + \vec{V_{36}} + \vec{V_{60}} = \vec{0}, \tag{2.4}$$

$$\vec{V_{34}} + \vec{V_{45}} + \vec{V_{57}} + \vec{V_{73}} = \vec{0}. \tag{2.5}$$

The vector-loop equations are reformulated such as each vector is split into a scalar length and a vector with unit length of one:

$$\overline{P0P1} \cdot \vec{e}_{01} + \overline{P1P2} \cdot \vec{e}_{12} + \overline{P2P3} \cdot \vec{e}_{23} + \overline{P3P6} \cdot \vec{e}_{36} + \overline{P6P0} \cdot \vec{V_{60}} = \vec{0}, \tag{2.6}$$

$$\overline{P3P4} \cdot \vec{e}_{34} + \overline{P4P5} \cdot \vec{e}_{45} + \overline{P5P7} \cdot \vec{e}_{57} + \overline{P7P3} \cdot \vec{e}_{73} = \vec{0}. \tag{2.7}$$

The mechanism is defined in its retracted position during parameterization, hence following lengths are known and independent of the angle at the actuator (ϕ_0):

$$\overline{P0P1} = \text{const.},\ \overline{P1P2} = \text{const.},\ \overline{P2P3} = \text{const.},\ \overline{P6P0} = \text{const.}, \tag{2.8}$$

$$\overline{P3P4} = \text{const.},\ \overline{P4P5} = \text{const.},\ \overline{P5P7} = \text{const.}. \tag{2.9}$$

Additionally, for the retracted position following lengths are known, but they change during deployment:

$$\overline{P3P6} \neq \text{const.}, \tag{2.10}$$

$$\overline{P7P3} \neq \text{const.}. \tag{2.11}$$

The vector-loop equations are rewritten and cover among others the angles of the mechanism:

$$\begin{aligned} \overline{P0P1} \cdot \begin{pmatrix} \cos(\phi_0) \\ \sin(\phi_0) \end{pmatrix} + \overline{P1P2} \cdot \begin{pmatrix} \cos(\phi_1) \\ \sin(\phi_1) \end{pmatrix} + \overline{P2P3} \cdot \begin{pmatrix} \cos(\phi_2 - \gamma_2) \\ \sin(\phi_2 - \gamma_2) \end{pmatrix} \dots \\ \dots + \overline{P3P6} \cdot \begin{pmatrix} -\cos(\gamma_{67}) \\ \sin(\gamma_{67}) \end{pmatrix} + \begin{pmatrix} x_{P0} - x_{P6} \\ z_{P0} - z_{P7} \end{pmatrix} = \vec{0}, \end{aligned} \tag{2.12}$$

$$\begin{aligned} \overline{P3P4} \cdot \begin{pmatrix} \cos(\phi_{30}) \\ \sin(\phi_{30}) \end{pmatrix} + \overline{P4P5} \cdot \begin{pmatrix} -\cos(\phi_5) \\ -\sin(\phi_5) \end{pmatrix} + \begin{pmatrix} x_{P7} - x_{P5} \\ z_{P7} - z_{P5} \end{pmatrix} \dots \\ \dots + \overline{P7P3} \cdot \begin{pmatrix} -\cos(\gamma_{67}) \\ \sin(\gamma_{67}) \end{pmatrix} = \vec{0}. \end{aligned} \tag{2.13}$$

For illustration of the variables, refer to Figures 7, 8 and 9. For the system of equations following variables are known:

1. Angles: γ_{67}, γ_2, γ_3,
2. Lengths: $\overline{P0P1}$, $\overline{P1P2}$, $\overline{P2P3}$, $\overline{P6P0}$, $\overline{P3P4}$, $\overline{P4P5}$, $\overline{P5P7}$,

which are derived from the geometrical relationships of the mechanism in the retracted position. These variables are constant throughout the deployment, hence they are independent of the angle at the actuator (ϕ_0). The angle at the actuator (ϕ_0) serves as a boundary condition which is incrementally increased while deploying the mechanism. So, only the distances of the carriage to the ends of the track are variable lengths and change during deployment. In total we obtain six unknown variables/degrees of freedom for the mechanism, which read:

1. Angles: ϕ_1, ϕ_2, ϕ_5, ϕ_{30},
2. Lengths: $\overline{P3P6}$, $\overline{P7P3}$.

However, only four equations are available. To solve the system of non-linear equations two additional side relationships are considered, which are:

$$\overline{P3P6} + \overline{P7P3} = \overline{P6P7} = \text{const.} \tag{2.14}$$

$$\phi_{30} = 180° - \gamma_3 - \gamma_2 + \phi_2. \tag{2.15}$$

γ_3 and γ_2 are determined for the retracted mechanism and are independent of the angle of

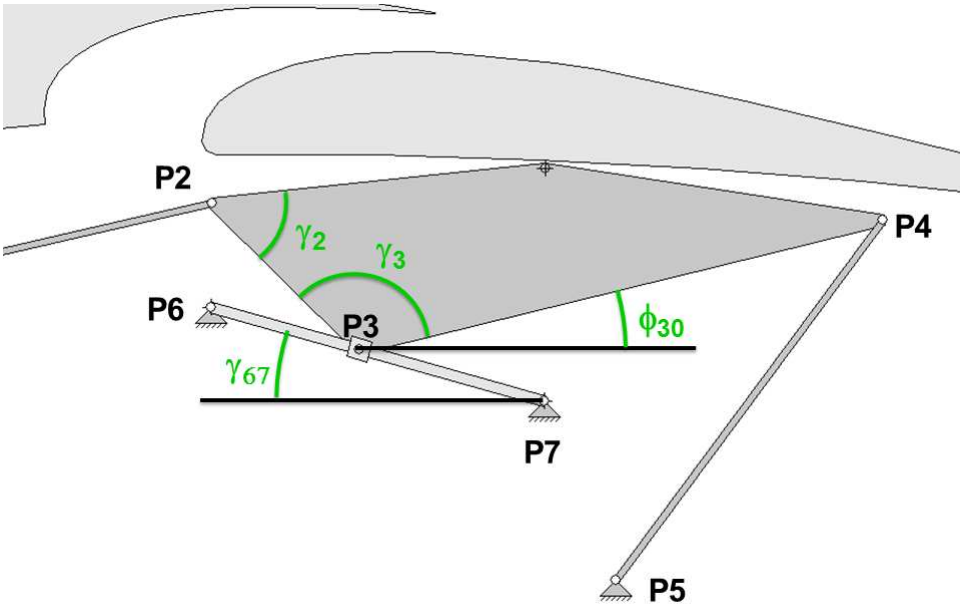

Figure 8: Sketch of a track-linkage system and the geometrical relationships.

the actuator. Therewith, the number of unknown variables/degrees of freedom is reduced and four unknown variables ($\phi_1,\ \phi_2,\ \phi_5,\ \overline{P3P6}$) are left. For illustration refer to Figure 9. The system of non-linear vector loop equations reads then:

$$\begin{aligned}
\Psi_1 &= \overline{P0P1} \cdot \cos(\phi_0) + \overline{P1P2} \cdot \cos(\phi_1) + \overline{P2P3} \cdot \cos(\phi_2 - \gamma_2) - \overline{P3P6} \cdot \cos(\gamma_{67}) + x_{P0} - x_{P6} \\
\Psi_2 &= \overline{P0P1} \cdot \sin(\phi_0) + \overline{P1P2} \cdot \sin(\phi_1) + \overline{P2P3} \cdot \sin(\phi_2 - \gamma_2) + \overline{P3P6} \cdot \sin(\gamma_{67}) + z_{P0} - z_{P7} \\
\Psi_3 &= \overline{P3P4} \cdot \cos(k_1 + \phi_2) - \overline{P4P5} \cdot \cos(\phi_5) + x_{P7} - x_{P5} - (\overline{P6P7} - \overline{P3P6}) \cdot \cos(\gamma_{67}) \\
\Psi_4 &= \overline{P3P4} \cdot \sin(k_1 + \phi_2) - \overline{P4P5} \cdot \sin(\phi_5) + z_{P7} - z_{P5} + (\overline{P6P7} - \overline{P3P6}) \cdot \sin(\gamma_{67})
\end{aligned} \tag{2.16}$$

The constant angle k_1 reads:

$$k_1 = 180° - \gamma_3 - \gamma_2.$$

For solving the system of non-linear equations a root-finding method is used.
The vector of variables reads:

$$\vec{q}(\phi_0) = \begin{bmatrix} \phi_1(\phi_0) \\ \phi_2(\phi_0) \\ \phi_5(\phi_0) \\ \overline{P3P6}(\phi_0) \end{bmatrix} \tag{2.17}$$

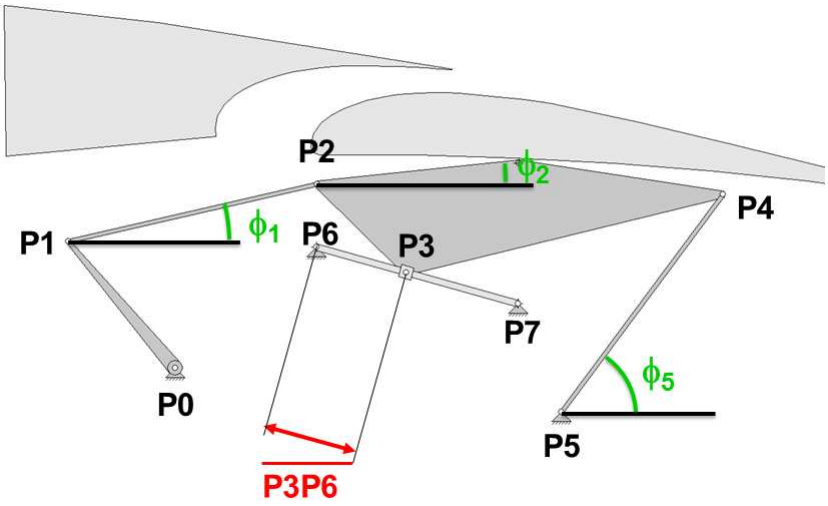

Figure 9: Sketch of a track-linkage system with indicated degrees of freedom.

and it depends on the angle of the actuator. The vector of variables is updated by the following formula for a discrete position of the mechanism:

$$\vec{q}^{\,i+1} = \vec{q}^{\,i} + \Delta\vec{q}. \tag{2.18}$$

The current solution of the vector of variables is (i) and the next solution is indicated as (i+1). The vector of variables is updated until the following limit is underrun:

$$|\Delta\vec{q}| \leq \epsilon. \tag{2.19}$$

ϵ is the user-defined convergence criterion. The variation of the vector of variables $\Delta\vec{q}$ is calculated as follows:

$$\Delta\vec{q} = -J^{-1} \cdot \vec{\Psi}(\vec{q}^{\,i}), \tag{2.20}$$

where J stands for the Jacobian matrix and $\vec{\Psi}$ for the system of non-linear equations, that covers the vector-loops ($\vec{\Psi} = (\Psi_1, \Psi_2, \Psi_3, \Psi_4)^t$), refer to Equation (2.16)). The Jacobian matrix reads:

$$J = \begin{bmatrix} \frac{\partial\Psi_1}{\partial\phi_1} & \frac{\partial\Psi_1}{\partial\phi_2} & \frac{\partial\Psi_1}{\partial\phi_5} & \frac{\partial\Psi_1}{\partial\overline{P3P6}} \\ \frac{\partial\Psi_2}{\partial\phi_1} & \frac{\partial\Psi_2}{\partial\phi_2} & \frac{\partial\Psi_2}{\partial\phi_5} & \frac{\partial\Psi_2}{\partial\overline{P3P6}} \\ \frac{\partial\Psi_3}{\partial\phi_1} & \frac{\partial\Psi_3}{\partial\phi_2} & \frac{\partial\Psi_3}{\partial\phi_5} & \frac{\partial\Psi_3}{\partial\overline{P3P6}} \\ \frac{\partial\Psi_4}{\partial\phi_1} & \frac{\partial\Psi_4}{\partial\phi_2} & \frac{\partial\Psi_4}{\partial\phi_5} & \frac{\partial\Psi_4}{\partial\overline{P3P6}} \end{bmatrix} \tag{2.21}$$

Note, the determinant of the Jacobian matrix is zero when the mechanism reaches a singularity.
The deployment of the mechanism and flap is stopped when the carriage reaches the end of the track with a defined distance, i.e. the stopping criterion reads: $\overline{P3P7} \leq \epsilon_2$. Additionally, it is possible to define a maximum deflection angle of the flap. When the flap element reaches this value the deployment of the mechanism stops.

For every discrete position of the mechanism the setting of the flap is determined and it is written to a file. Additionally, this file covers the coordinates for each node of the mechanism for each discrete position of the mechanism. Besides the geometrical parameters relevant for aerodynamics (gap, overlap, deflection angle), the minimum gap along the cove and its position are determined in each discrete position of the mechanism. By this gap convergence is monitored.
For every discrete position of the mechanism it is checked if a clash is recognized between the flap and the main element. The geometry of the spoiler can be defined such that a clash of the flap element with this entity is ignored. This implementation is foreseen to cover that spoilers can be moved upwards by flap elements during deployment.
As quality characteristics of the mechanism, two scalar values are written to a file which reflects clash (Q_c) and gap convergence (Q_G) which are both in the domain [0, 100]. The higher the values are the further the clash and the minimal gap moves away from the trailing edge of the main element along the cove. The user defines a number of positions of the actuator at which the coordinates of the flap are written to files. The user specified values are within the domain [0, 1]. 0 equals the actuator in retracted position and 1 equals the actuator in maximum deployed position.
The tool is programmed in the programming language C and it is suited for automatized optimization processes, i.e. no interactive controlling is needed. For the spline interpolation and the determination of the gap, gap convergence and clash functions from the mesh generation software MegaCADs are adapted and implemented in the kinematics tool.

2.4.2 Validation of the Kinematics Module

The validation of the kinematics module is performed by a comparison of the trajectory path of a flap provided by the kinematics tool TEFlaMeS and by the tool developed by the author. TEFlaMeS is a tool to simulate trailing edge mechanisms and to estimate the mass of the mechanism based on aerodynamic loads on the flap. The tool is developed and validated by Holert [54]. In contrast to the tool developed by the author which is based on vector-loop equations, TEFlaMeS uses an analytical method to calculate the deployment of the flap. The method is based on the norm VDI-2729.
As validation test case a typical Airbus flap mechanism is taken. The definition of the geometry of the flap mechanism and the airfoil geometry are taken from the documentation of TEFlaMeS [72]. This test case among others is used by Holert to validate TEFlaMeS itself with aircraft data. Figure 10 shows the distribution of the geometrical parameters (deflection angle, gap versus overlap) of the flap during the deployment. For better illustration of the comparison of the two methods, not all data samples are represented in the figure as symbols for TEFlaMeS.
The flap in retracted position is located at $O/L \ / \ O/L_{\text{max}} = 1$ and while it is deflected the value for the gap increases. The deflection angle of the flap gets negative during the first phase of the deployment, just after the flap leaves the retracted position. Thereafter the deflection angle increases while the overlap decreases. Negative deflection angles of the flap during the first phase of the deployment do not lead to a clash of the flap with the main element, since the gap increases monotonically from retracted to fully deployed flap and it has positive values.
The curves for the two methods collapse for gap and deflection angle versus the overlap respectively. The two methods are in very good agreement for the shown test case.

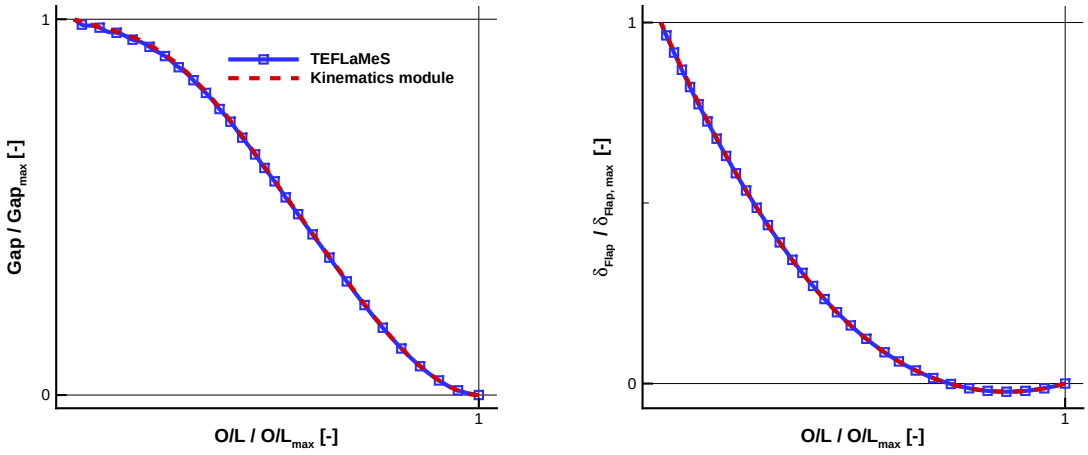

Figure 10: Left: distribution of the gap versus overlap of the flap during deployment for the baseline configuration. Right: distribution of the deflection angle versus overlap of the flap during deployment for the baseline configuration. Note: not all data points are represented as symbols.

2.5 Parameterization

Throughout this work two different parameterizations are used to define the flap setting. The first one is based on geometrical parameters relevant in aerodynamics and the second one is related to the deployment mechanism of the system. Within this work only one parameterization is used for the slat and it is based on a kinematic perspective.
The focus of this work is laid on the trailing edge system. For the leading edge mechanism the standard, state-of-the-art mechanism is used, which is a constant radius track system. The shapes of slat, flap and main element are constant throughout this work, i.e. we deal here solely with setting optimization.

2.5.1 Parameterization of the Leading-Edge High-Lift System

For the slat we regard a constant radius track. As stated before, the focus of the work is laid on the trailing edge mechanism. Therefore, a standard mechanism for the deployment of the slat was chosen here. It was aimed at a simple application of the slat mechanism as leading edge mechanism. To simplify the application, the hinge point and the radius are kept constant throughout this work. Thus, no additional checks w.r.t. clashes of the slat track with the skin of the main element are needed. Additionally, no structural assessment of the front spar has to be performed, which would be necessary when the size of the cutout in the front spar changes due to a variation in the slat track geometry.
Next to the just mentioned aspects, the parameterization of the leading edge high-lift system is also simplified by this approach. It has only one degree of freedom to define the slat setting, sketched in Figure 11-left. The parameter is the slat deflection angle (δ_{Slat}). The parameterization of the slat is aimed to be simple and realistic, but should offer the possibility to adjust the slat to achieve a balanced high-lift system.
Figure 11-right shows the trajectory path of the slat during deployment. The distribution of the gap and deflection angle versus the overlap are shown, respectively. For the gap versus

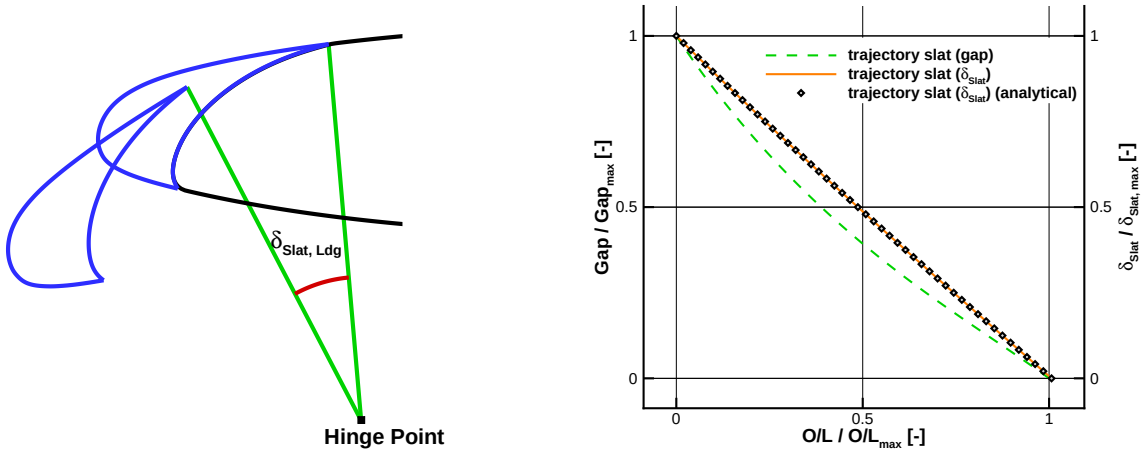

Figure 11: Left: illustration of the parameterization of the slat setting. Right: trajectory path of the slat for constant-radius track mechanism.

the overlap a slight non-linear behavior is found. The relationship between the deflection angle and the overlap show almost linear behavior with a negative slope. This seems to be contradictory to the fact that the slat is rotated around the hinge point, where trigonometric functions are used. The data was generated by an iterative execution of MegaCADs while the slat was deployed. For cross-checking, validation reasons the relations between deflection angle and overlap were derived analytically to ensure the accurate functionality of MegaCADs. The results of the analytical point of view are indicated by symbols. It is obvious that the two approaches collapse.
The slat is retracted when the ratio of overlap and maximum overlap is equal to one. While the overlap is reducing both the deflection angle and the gap increase.

2.5.2 Aerodynamic Parameterization of the Trailing-Edge High-Lift System

This parameterization of the flap setting follows the definition of Woodward and Lean [81]. The flap is parameterized by aerodynamic parameters namely dz, overlap (O/L) and deflection angle (δ_{Flap}). dz denotes the vertical distance of the flap towards the z-coordinate of the trailing edge of the main element. By this parameterization the gap is indirectly determined. The parameterization is illustrated in Figure 12. This parameterization is simpler to implement in contrast to the classical parameterization where the gap width is used instead of dz.

In total this parameterization has all three degrees of freedom for one setting.

2.5.3 Kinematic Parameterization of the Trailing-Edge High-Lift System

The parameterization of the flap mechanism is shown in Figure 13. For the parameterization of the flap deployment mechanism we can distinguish two categories of parameters.
The first category defines the geometry of the mechanism in retracted position by the definition of the nodes of the mechanism ($P0$-$P2$, $P4$-$P7$). $P6$ and $P7$ define the beginning and the end of the track, respectively. A side condition is used which implies that node $P3$ (position

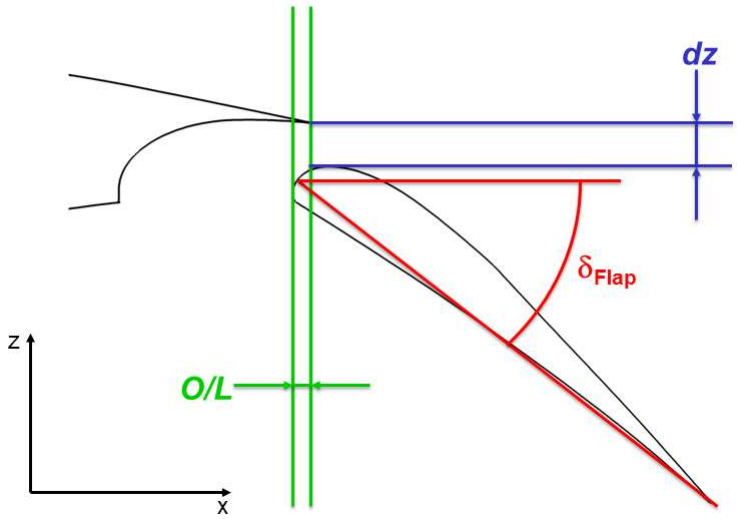

Figure 12: Sketch of the aerodynamic parameterization of the flap.

of the carriage on the track) is identical with node $P6$ in retracted position. Consequently it is ensured that the carriage is located on the track. By these parameters, the trajectory path of the flap is defined during deployment.
The second category defines the positions of the flap for take-off and landing on the trajectory path. This is realized by the definition of the angle at the actuator (ϕ_0), refer to Figure 13.
By this approach the aerodynamic parameters (gap, overlap and deflection angle) are defined indirectly by the previously described parameters. In total we obtain 14 parameters to

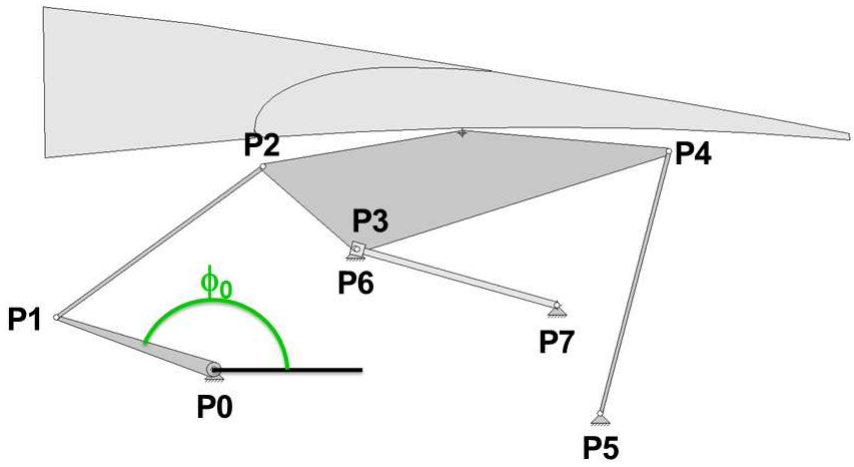

Figure 13: Sketch of the kinematic parameterization of the flap.

define the geometry of the track-linkage system in retracted position. Additionally, we have to consider one parameter per flap setting (angle at the actuator). For the evaluation in this thesis, where we consider two settings (take-off, landing), we obtain in total 16 parameters for the definition of the flap geometry and two flap settings.
Basically the trajectory path of the flap is defined by the rear link ($\overline{P4P5}$) and the track ($\overline{P6P7}$). The links at the actuator ($\overline{P0P1}$, $\overline{P1P2}$) do not influence the trajectory path but limit the maximum deployable position of the flap. These parameters are of interest when the mass estimation of the flap mechanism is considered. To be able to compare the various

results the actuation system is always accounted for. In almost all optimizations the mass of the mechanisms is calculated but it is not necessarily reflected by the objective function. Additionally, this approach is taken to ensure that the results are not influenced by changes in the parameterization. In terms of computational time within the design processes shown in section 2.3, the estimation of the mass of the mechanism plays an insignificant role. Hence, there is no drawback from the time perspective in the evaluation of this discipline.

2.6 Swept Wing Transformation

The planform of a typical wing of a commercial airplane has a swept leading and trailing edge. This typical planform of a wing is sketched in Figure 14. β is the leading edge sweep angle. This figure shows additionally the reference cut plane used in this work to extract the airfoil shape (Plane 1). Further on, the two-dimensional computational domain is shown used for the CFD computations of the aerodynamics. This domain has two sides and inbetween the airfoil shape and chord length is constant. The on-flow velocity (v_{2D}) is parallel to the sides and it is leading edge normal. Plane 2 represents the plane on which the shape of the airfoil is projected for the two-dimensional computations. According to the theory of swept wings of Busemann [82] only the flow component normal to the leading edge is relevant for the aerodynamics of this airfoil.
To account for the sweep angle within the two-dimensional computations, the following adaptations are done.
First, an adaptation of the airfoil geometry is done and second, the adaptation of the free stream conditions is calculated. To be able to use the aerodynamic coefficients from the two-dimensional computations for the flight mechanics, the coefficients have to be converted back to the line-of-flight system. In a previous project it was found that two-dimensionally

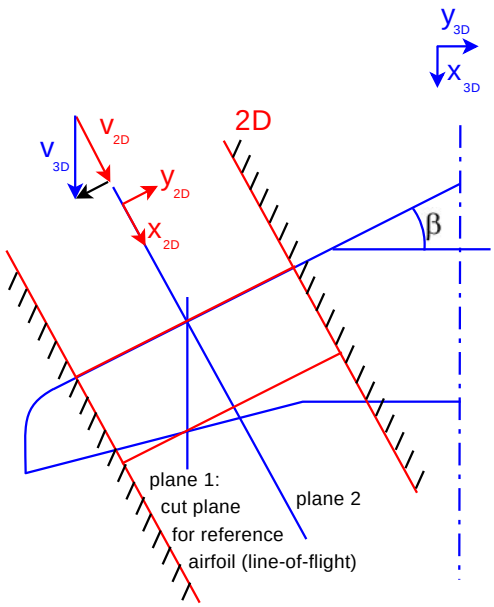

Figure 14: Sketch of the planform of swept wing and illustration of the computational domain for two-dimensional computations. The sides of the computational domain are defined as symmetry planes. The on-flow velocity for the two-dimensional domain is the leading edge normal component of the three-dimensional on-flow velocity.

optimized high-lift shape and setting of a representative wing section are feasible for the three-dimensional wing. The aerodynamic integral coefficients can be predicted by simple relationships for a full span flap and slat, refer to [46].

2.6.1 Adaptation of the Airfoil Shape

Within the context of the adaptation of the airfoil shape for the two-dimensional computations, the deployment procedure for slat and flap has to be explained. The deployment procedure for slat and flap differ, since the planes in which the devices are deployed are not the same. The flap device is deployed parallel to the symmetry plane of the aircraft's wing, i.e. in the line-of-flight plane. This procedure is typical for transport aircraft, in which mechanisms are regularly aligned roughly with the line-of-flight. The symmetry plane is indicated as a blue dashed line in Figure 14. The plane in which the flap device is deployed is plane 1. In contrast the slat device is deployed perpendicular to the leading edge of the wing in plane 2. The deployment of the slat is again based on a realistic aircraft slat deployment, where the elements of the slat are deployed perpendicular to the leading edge.
Within the process chain following procedure is conducted. Firstly the flap is deployed in plane 1. Secondly the reference airfoil shape with retracted slat and deployed flap is mapped to plane 2. For the mapping of the airfoil shape following relationships are applied, which are a simple geometrical projection from plane 1 to plane 2 according to Busemann (refer to [82]):

$$x_{2D} = x_{3D}, \tag{2.22}$$

$$z_{2D} = z_{3D} / \cos(\beta), \tag{2.23}$$

where β is the sweep angle of the leading edge. Finally the slat is deployed in plane 2, i.e. normal to the leading edge.

2.6.2 Adaptation of the Free Stream Conditions

To account for the sweep angle of the wing the free stream conditions need to be adjusted. Only the component of the three-dimensional free stream velocity perpendicular to the leading edge is accounted for the two-dimensional computations. The component along the leading edge is not considered by this approach, since this component has no influence on the pressure distribution of the airfoil. For plane 2 the free stream velocity, Mach and Reynolds number read:

$$v_{2D} = v_{3D} \cdot \cos(\beta), \tag{2.24}$$

$$M_{2D} = M_{3D} \cdot \cos(\beta), \tag{2.25}$$

$$Re_{2D} = Re_{3D} \cdot \cos^2(\beta). \tag{2.26}$$

Based on the mentioned relationships the three-dimensional on-flow conditions presented in Table 2 are therewith converted into the leading edge normal system. These on-flow conditions are presented in the Table 3.

2.6.3 Conversion of Aerodynamic Coefficients

After the aerodynamic computations in the two-dimensional domain are accomplished, the integral coefficients like drag, lift and pitching moment are converted back to the line-of-

Table 3: Flow state conditions for two-dimensional CFD evaluations of the high-lift airfoil in the leading edge normal system. The Reynolds number is based on the clean airfoil chord length.

	Mach number [-]	Reynolds number [10^6]	Remark
Take off:			
Stall	0.215	29.7	$C_{\text{L,max}}$
Climb	0.258	35.7	$C_L = C_{\text{L,max,TO}}/1.13^2$
Ground-roll @ lift-off	0.236	32.7	AoA = 0.0°
Landing:			
Stall	0.159	22.0	$C_{\text{L,max}}$
Approach	0.195	27.1	$C_L = C_{\text{L,max,Ldg}}/1.23^2$
Ground-roll @ touch down	0.183	25.3	AoA = 0.0°

flight plane. The following relationships are applied to convert the coefficients:

$$C_{L,\text{2.5D}} = C_{L,\text{line-of-flight}} = C_{L,2D} \cdot \cos^2(\beta), \tag{2.27}$$

$$C_{D,\text{2.5D}} = C_{D,\text{line-of-flight}} = C_{D,2D} \cdot \cos^2(\beta). \tag{2.28}$$

The simplified relationship for the drag coefficient does not reflect the distinction of pressure and friction drag, which has to be considered individually from a theoretical point of view. However in wind tunnel experiments, refer to [46], it was found, that the shown relationship matches fairly well with these experiments and it is widely used as an engineering approximation. The drag coefficients obtained from the CFD calculations comprise drag due to friction and pressure loss. To account that an increase in the lift-coefficient additionally has an influence on the drag coefficient we add the lift-induced-drag. Thus we obtain a quasi three-dimensional drag coefficient. Note that this is not done due to the sweep angle of the wing. For the lift coefficient no distinction between three- and two-dimensions is done. The following text book relationships are used:

$$C_{L,\text{3D}} = C_{L,\text{2.5D}}, \tag{2.29}$$

$$C_{D,\text{quasi 3D}} = C_{D,\text{2.5D}} + \frac{C_{L,\text{2.5D}}^2}{\pi \cdot e \cdot \Lambda}, \tag{2.30}$$

where e stands for the Oswald factor and Λ for the aspect ratio of the wing.
Note that within this work the Oswald factor is constant. In this work a typical Oswald factor for a commercial long-range aircraft is used and it reads: $e = 0.9$. This provokes that the shape of the lift distribution of the three-dimensional wing is assumed to be constant.

2.7 Simulation of Aerodynamic Flows

Aerodynamics is a subdiscipline of fluid mechanics and it is related to the air as a fluid. The governing equations in fluid mechanics and aerodynamics are the Navier-Stokes equations.

The Navier-Stokes equations in integral, conservative form read:

$$\iiint_V \frac{\partial}{\partial t}\vec{W}dV + \iint_S \overline{\overline{F}} \cdot \vec{n}d\mathrm{S} = \vec{0}, \tag{2.31}$$

where $\vec{W}$ is the vector of conservative state variables $(\rho, \rho\vec{u}, \rho E)^t$. Here ρ stands for density, $\vec{u}$ for the velocity vector and E represents the specific total energy per unit mass. $\overline{\overline{F}}$ is the flux density tensor which is built of the inviscid (convective) and the viscous tensor. V is the control volume which has an outer boundary S and an outer normal vector $\vec{n}$.
The Navier-Stokes equations are a system of integral equations and the first equation corresponds to the conservation of mass, the second to the conservation of momentum and the third to the conservation of energy. In consideration of the law of perfect gases the system of equations is closed. However for practical, turbulent cases the Navier-Stokes equations cannot be solved analytically. Therefore this set of equations is transferred to the Reynolds Averaged Navier Stokes (RANS) equations. Hereby the flow variables are divided into an averaged value and a fluctuation. With the averaged flow variables applied on the Navier-Stokes equations, the RANS equations are obtained. By this approach new unknown variables are established while the number of equations remains constant and hence a closure problem arises. To solve this closure problem turbulence models are applied which model the turbulent behavior of the flow based on empirical/semi-empirical relationships. Various turbulence models are available in literature ranging from eddy viscosity (e.g. one- and two-equation models) to full differential Reynolds stress models. The term eddy viscosity is proposed by Boussinesq, refer e.g. to the textbook of Wilcox [83]. In his proposal a relationship between the turbulent stresses and the mean flow was introduced to close the system of equations (RANS).
Within this work the one-equation turbulence model from Spalart and Allmaras (SAO) [84] is used to close the system of equations. Spalart and Allmaras directly formulate a transport equation for the eddy viscosity. The equation includes a destruction term that depends on the distance to the wall. According to Spalart and Allmaras the turbulence model "*appears to be a good candidate for more complex flows such as high-lift systems*"[5]. Indeed this model is nowadays widely used for the prediction of high-lift aerodynamics, refer to v. Dam et al. [50], Rumsey et al. [85], Murayama et al. [19], Wang et al. [86] and refer to the AIAA-High-Lift Prediction Workshops [22, 23]. Rumsey et al. describe and classify the SAO turbulence model as "*one of the most widely used turbulence models today*"[6] (2002), it is "*extremely robust and does well for 2-D mixing layers, wake flows and boundary layer flows*"[6], but they also state that "*it has a tendency to overdiffuse free vorticity*"[6].

2.7.1 The Flow Solver DLR-TAU code

The DLR-TAU code [77] is a finite-volume CFD solver for unstructured meshes. The code solves the compressible, three-dimensional, unsteady Reynolds averaged Navier-Stokes equations. The spatial approximation is done by a finite-volume method with second order central discretization scheme with scalar artificial dissipation. It is an established code for aerodynamic applications at DLR, industry and university. Discrete equations are integrated explicitly in time by multistage Runge-Kutta schemes or implicitly by a Lower-Upper Symmetric Gauss-Seidel (LU-SGS) scheme, using local time-stepping and multigrid acceleration.

[5] Spalart and Allmaras [84], page 1
[6] Rumsey et al. [24] page 151

Within this thesis two different approaches are used for the computation of the aerodynamics: a progressive and a robust (moderate) one. These two approaches differ in the settings for the acceleration techniques and influence only the convergence rate. Note that according to theory the two approaches achieve identical aerodynamic solutions when the computations are sufficiently converged.
In some cases the progressive approach that is tuned to obtain a high convergence rate, which is unfortunately not as stable, does not lead to a sufficient convergence of the flow variables and aerodynamic coefficients. The robust/conservative approach offers a more stable behavior but less convergence rate.

2.7.2 Computational Mesh

The aerodynamics of a three-element airfoil is complex. For this reason a well resolved mesh with adequate element quality is necessary to predict the complex flow phenomena around the geometrical entities. A focus for the meshing process is laid on the smoothness of the mesh, boundary layer and wake resolution for changing flap and slat settings. Further on, the quality of the mesh should remain at best constant throughout the optimization independently of the slat and flap settings to ensure a physically motivated final, optimized high-lift configuration. A mixed mesh approach is used to mesh the computational space. That means not only one type of mesh element is used to fill the computational space. In this thesis quadrilateral and triangular elements are applied. Figure 15 shows the topology of the mesh. The boundary layer and near-wall region are resolved with quadrilateral (structured) elements (region a-m). Each airfoil element has a C-type mesh with the wake being resolved with quadrilateral elements. In the cove regions of the slat and the main element (region Y,

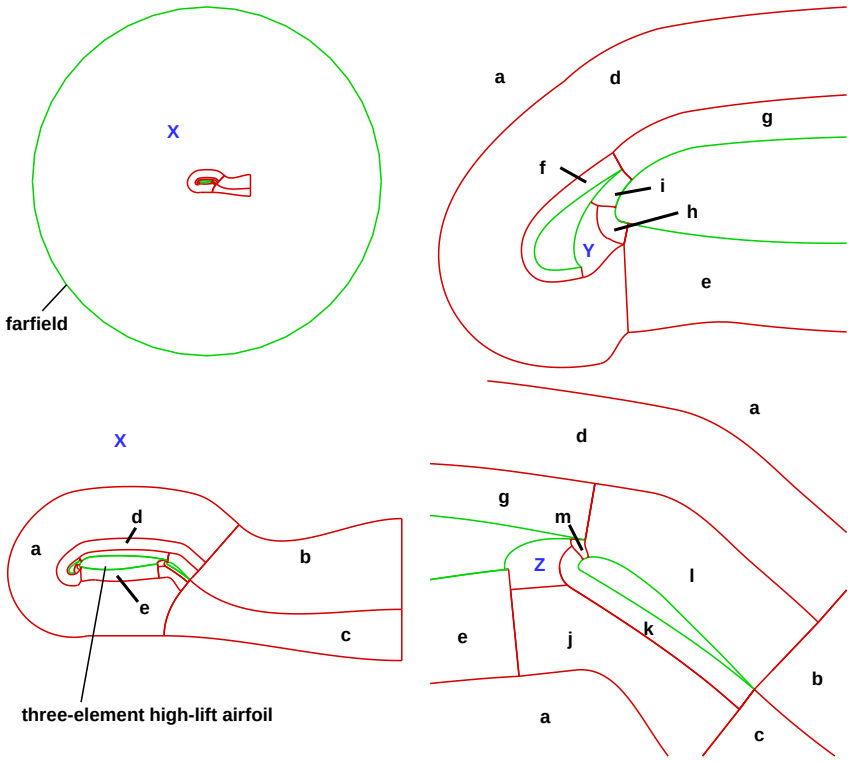

Figure 15: Mesh topology for three-element high-lift configuration. Region a-m: quadrilateral elements. Region X-Z: triangular elements.

Z) triangular (unstructured) elements are used to increase the flexibility of the mesh in order to deal with setting changes of slat and flap, see Figure 16. In the outer field, triangular elements are used as well (region X). On the walls first a sublayer mesh is generated to ensure a sufficient near wall resolution for the turbulence model. In this study the meshes are always generated from scratch and therefore the total number of elements differs in the regions where triangular grid elements are used. For the gaps a maximum cell size is defined, hence the number of cells in the gaps increases when the gap size rises.
For the generation of the computational meshes the mesh generation tool MegaCADs [75] developed at DLR is used. MegaCADs offers in its current version the generation of mixed meshes in the two- and three-dimensional space, refer to Wild [76]. Further on, routines can be created which enable the user to automatize the mesh generation process while the geometry/setting of the elements change but the topology of the structured parts remains constant. Especially for optimization these capabilities are important to ensure an optimized configuration which is motivated by physics of the flow and not by the variation of the quality of the mesh.

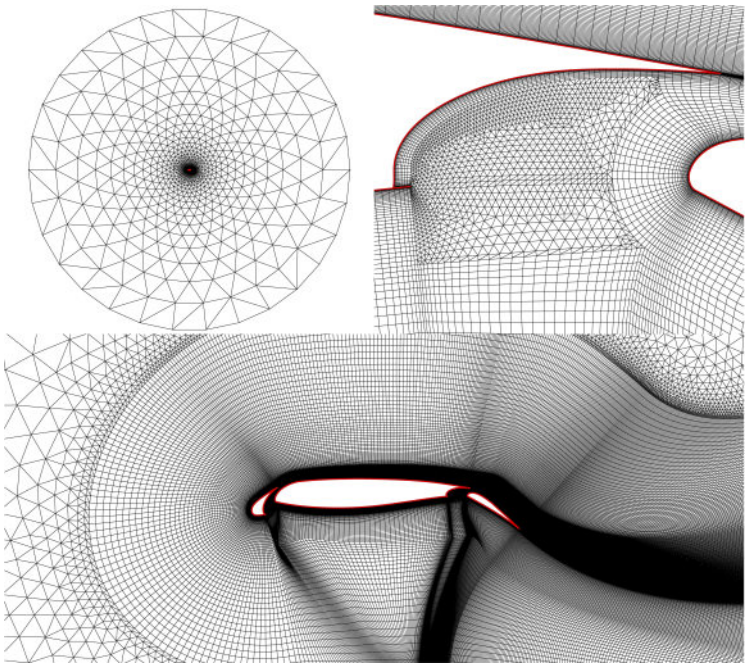

Figure 16: Details of the mixed mesh generated with the mesh generation tool MegaCADs.

2.7.3 Resolution of the Numerical Mesh for the High-Lift Aerodynamics

The time for a turn-around cycle of an optimization loop in aerodynamic shape/setting optimization is mainly dominated in terms of computational time by the computation of the aerodynamics. Within this work the calculations of the kinematics, flight mechanics, mass of the mechanisms and generation of the mesh are almost negligible with respect to the computational time. Therefore, it is highly beneficial to reduce the computational time of the CFD computations by a reduction of the number of cells in the computational domain. However, it has to be ensured that the proper physics of the high-lift flow are still obtained. Before the optimization process is started, a mesh study was performed to minimize the number of elements on the walls and in the gaps in order to decrease the turn-around times

Table 4: Number of total mesh points (two planes) for take-off and landing configuration for different resolutions.

	Take-off	Landing
fine	$\approx 3.4{\cdot}10^6$	$\approx 3.7{\cdot}10^6$
medium-fine	$\approx 3.0{\cdot}10^6$	$\approx 3.2{\cdot}10^6$
medium-coarse	$\approx 2.4{\cdot}10^6$	$\approx 2.5{\cdot}10^6$
coarse	$\approx 1.4{\cdot}10^6$	$\approx 1.5{\cdot}10^6$

for the CFD computations, while the physics are still sufficiently well resolved. Therefore, different computational meshes are compared in the following w.r.t. to the nearwall and wake flow characteristics. The topology of the meshes is not changed, changes are done in the number of boundary elements and in the number of elements to discretize the gaps and the wakes.
To find a suitable mesh resolution, four different meshes are created. Table 4 summarizes the number of cells for the different meshes. According to the mentioned table we can see that the total number of mesh points is more than halved from the finest to the coarsest mesh. The reduction of the boundary elements is roughly 40%. Note that all meshes have the same sublayer resolution to keep the near-wall distribution constant and to ensure a sufficient resolution for the turbulence model close to the walls.
The study is performed according to the free stream conditions presented previously in Table 3. For take-off and landing in each case the stalling condition is evaluated.
To compare the flow solutions on the different meshes the approach by Woodward and Lean [81] is followed. According to Woodward and Lean it is essential for the prediction of the maximum lift capability of a high-lift airfoil to have a proper prediction of the merging of boundary layers and wakes. Consequently, to obtain physically based aerodynamics of a high-lift airfoil it is important to correctly capture the wakes, boundary layer, shear layer, gap flow of the single elements and the merging of them. The merging of boundary layers and wakes can be made apparent by plotting the total pressure distribution normal to the wall. The total pressure coefficient is reduced by the effect of friction which takes place e.g. in the boundary layer.
For the comparison of the different mesh resolutions the total pressure coefficient $c_{p,tot}$ is considered, which is defined as follows:

$$c_{p,tot} = \frac{p_{tot} - p_\infty}{\frac{1}{2}\rho_\infty v_\infty^2}. \tag{2.32}$$

By the analysis of the total pressure distribution at different cuts normal to the surface of the airfoil we can examine the behavior of the high-lift aerodynamics. By this we can determine the resolution of the mesh needed to predict properly the high-lift aerodynamics. Five cuts are investigated, refer to Figure 17 and also to Woodward and Lean [81]. The first cut is located at the trailing edge of the slat; the second cut, approximately in the middle of the suction side of the main element; the third cut at the trailing edge of the main element. Cuts 4 and 5 are located in the middle of the suction side of the flap and at the trailing edge of the flap respectively.
Figure 17 shows the total pressure distribution of the take-off configuration at an angle of attack close to maximum lift. We see deviations between the results of the different meshes. For cut 1 the deviations between the different meshes are small. Only the coarse mesh shows

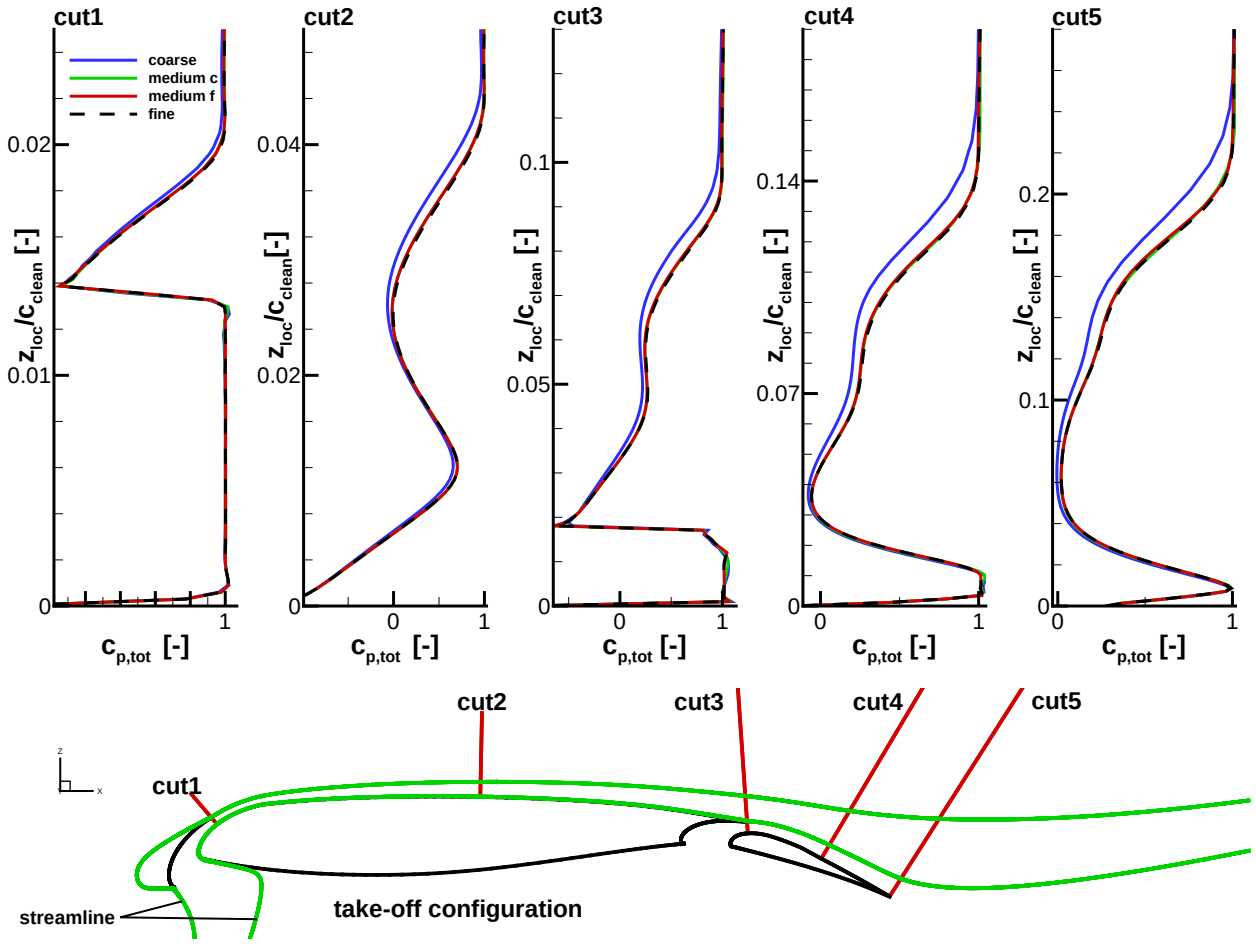

Figure 17: Total pressure coefficient distribution for five cuts normal to the surface of the take-off configuration (baseline configuration).

deviations to the finer meshes. The deviations are recognized at the outer bound of the boundary layer (suction side slat, $z_{\mathrm{loc}}/c_{\mathrm{clean}} \approx 0.02$) to the free stream. The predictions for the gap flow (slat) collapse well. The deviations increase along the chord of the airfoil. The boundary layer of the main element and the wake of the slat merge for cut 2, where the free-stream total pressure coefficient is not reached ($z_{\mathrm{loc}}/c_{\mathrm{clean}} \approx 0.01$). This region and the upper part of the slat wake show deviations for the coarse mesh compared to the finer meshes. On the flap the total pressure coefficient distribution of the coarse mesh differs significantly to the finer meshes. The individual wakes of the main element and the slat are less pronounced than for the finer meshes. A dip in the total pressure coefficient distribution for the wake of the slat element is almost not noticeable anymore. We can recognize the shear layer of the slat and the boundary layer of the main element in cut 1 which merge together and smooth the total pressure distribution of the slat gap flow (cut 2 to 5). For the boundary layers of the flap and main element (cut 3 to 5) no merging is observed.

Figure 18 shows the total pressure coefficient distribution at different stages on the slat, the main element and the flap for the landing setting at an angle of attack close to the maximum-lift coefficient, where no separation is recognized. Globally, the behavior of the different resolved meshes is similar to take-off, but the deviations are less pronounced. Additionally, small deviations are found for the medium-coarse mesh on the flap.

Cuts 1 to 3 are in good accordance for the differently resolved meshes. Only small devia-

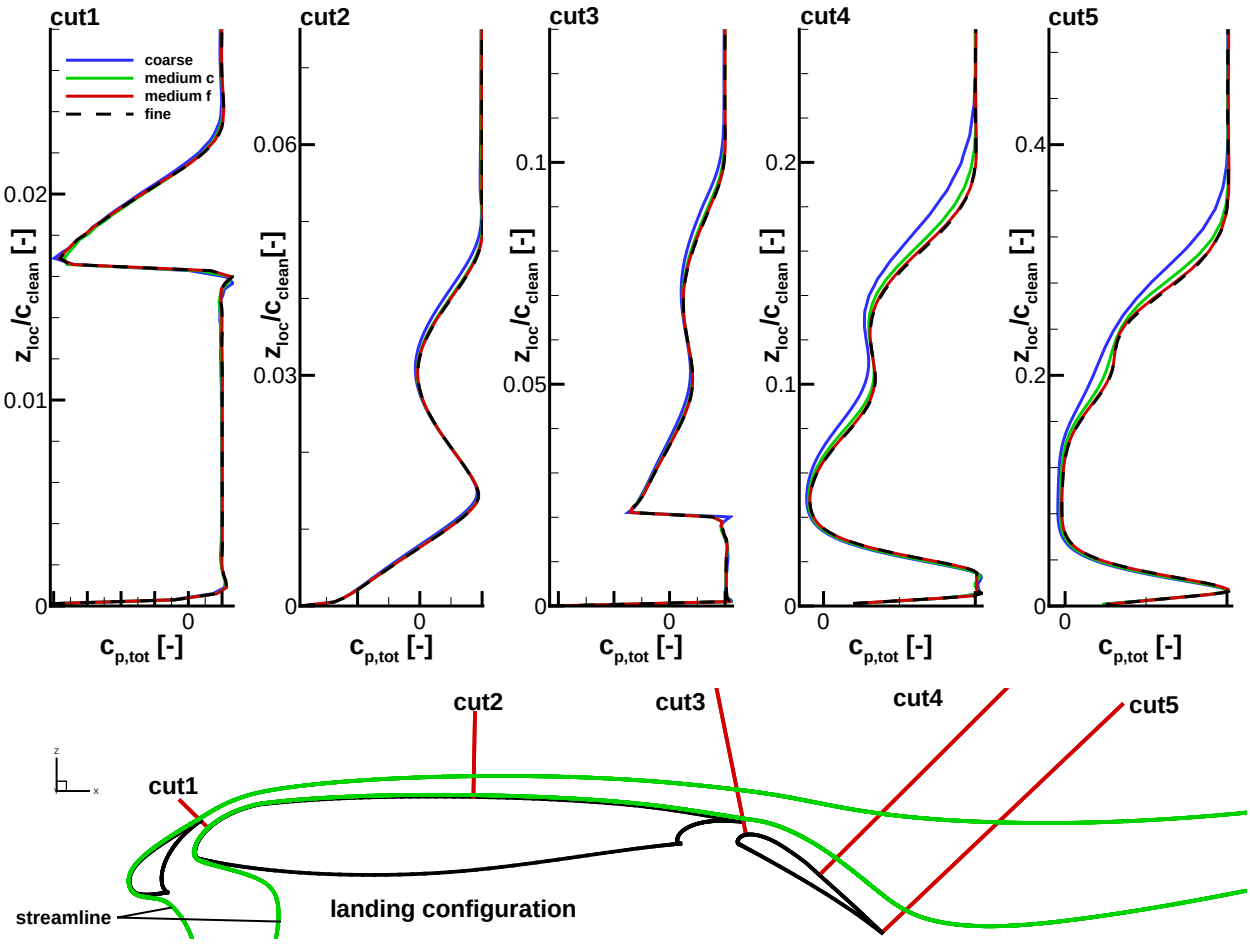

Figure 18: Total pressure coefficient distribution for five cuts normal to the surface of landing configuration (baseline configuration).

tions are recognizable in the wake of the suction side of the slat for cut 2 ($z_{\text{loc}}/c_{\text{clean}} \approx 0.04$) and 3 ($z_{\text{loc}}/c_{\text{clean}} \approx 0.08 - 0.1$) for the coarse mesh.
Cuts 4 and 5 show stronger deviations for the wake of the slat and for the main element, for the coarse mesh. For the medium-coarse mesh small deviations are recognized for these wakes. The finer meshes are in good agreement. Coarser meshes are naturally more dissipative, which results in a smoothed distribution of the total pressure coefficient and less distinct wakes. This is especially obvious for the coarse mesh, which shows almost no peak for the slat gap flow ($z_{\text{loc}}/c_{\text{clean}} \approx 0.2$) in cut 5.
For the further work meshes are generated with the resolution of the medium-coarse approach. This is a good compromise between computational cost and accuracy. This resolution approach resolves the wakes still sufficiently and reduces the time per computational iteration by roughly 24%.

2.7.4 Determination of Maximum Lift Coefficient

In high-lift aerodynamics the maximum lift coefficient determines the stall speed. Therefore one goal of the simulation of the high-lift system is to be able to determine the maximum lift coefficient for the different flap/slat settings accurately. In this work the approach described

by Wild [38] and Hain [87] is used. Figure 19 illustrates the procedure of the maximum lift coefficient determination. The first step of this process is to increase the angle of attack by

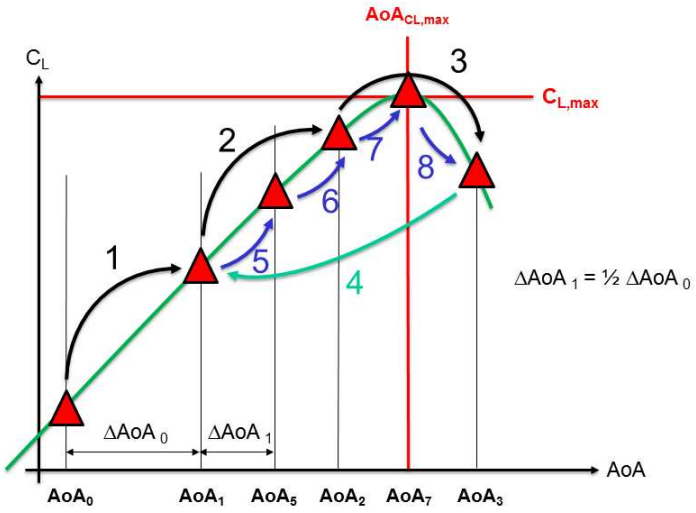

Figure 19: Sketch to illustrate the process to determine the maximum lift coefficient, according to the procedure developed by Wild [38] and Hain [87].

a given increment (ΔAoA_0) until the lift coefficient of the configuration decreases (step 1 to 3, computation of angles of attack: AoA_0, AoA_1, AoA_2, AoA_3). The next step (step 4) is to reinitialize the computation at the angle of attack AoA_1. This angle of attack is below the angle of attack where the lift coefficient decreases (AoA_3) with two angles of attack increments. Further on, the angle of attack increment is reduced, such as $\Delta AoA_1 = 0.5 \cdot \Delta AoA_0$. Then this procedure is repeated (step 5 to 8, computations of angles of attack: AoA_5, AoA_2, AoA_7, AoA_3). The computation for each angle of attack does not start from scratch, except the first angle of attack. The solution of the last calculated angle of attack is used, except when the angle of attack is reduced. Here an "old" solution for this angle of attack is loaded as restart to avoid hysteresis effects. The iterative determination of the maximum lift coefficient stops when the angle of attack increment underruns a predefined limit. In this work the predefined limit reads $\Delta AoA_{\text{min}} = 0.25°$. In this illustration the procedure stops after recomputing angle of attack AoA_3 because first, the lift decreases compared to angle of attack AoA_7 and second, the lower limit of the angle of attack increment reads $\Delta AoA_{\text{min}} = \Delta AoA_1$. Therefore the maximum lift is achieved at angle of attack of AoA_7. The last step is to fully converge the angle of attack at maximum lift.
This approach uses the Cauchy criterion, see equation (2.33), to decide whether the single computations are sufficiently converged. The Cauchy criterion reads:

$$\max |C^i_{L,2D} - C^{i-k}_{L,2D}| \leq \Delta C_{L,2D},\ k = 1, \ldots, P, \tag{2.33}$$

where i is the current number of solver evaluations and P is the number of Cauchy samples. Hain [87] gives a recommendation for the ratio $P/\Delta C_{L,2D}$ for two-dimensional high-lift configurations. Within this work the ratio is set to: $P/\Delta C_{L,2D} = 1 \cdot 10^6$ and it was determined for the chosen mesh fineness of the mesh study, refer to previous section.

2.8 Mass Estimation of Flap and Slat Mechanism

In the literature, Pepper et al. [56] present basic relationships for the estimation of the mass of high-lift systems. Within the context of the current work the method of Pepper is not suitable, since it estimates the mass of the mechanism due to the type of mechanism and its Fowler capability, but the influence of aerodynamic variations while considering the same type of mechanism is not captured. Hence Pepper presented a preliminary approach for the estimation of the mass of flap mechanisms. The aim of Pepper's work is to be able to investigate variations of the type of flap mechanism and its impact on the aircraft. A more sophisticated but still preliminary design related method TEFlaMeS is presented by Holert [53, 54, 72]. This method is capable to deal with minor changes of the geometry of a flap mechanism and it can estimate the impact on the mass of the mechanism. Additionally, this method is well validated and it showed good capabilities for the prediction of the mass of real-life flap mechanisms. In this work we therefore follow the method developed by Holert.
For the estimation of the mass of the slat mechanism no suitable method for this work was found. To overcome this issue a method was developed in close cooperation with ASCO industries[7]. ASCO industries is a leading company with broad experience in the design and manufacturing of slat tracks for a wide range of commercial aircraft. This method covers basic structural mechanical relationships to estimate the mass of the slat track and the rollers. The actuation is estimated based on the method of Holert. This method to determine the mass of the slat mechanism could only be checked w.r.t. the plausibility of results, but no real-life test case could be applied, because of the lack of a suitable data base.
The estimation of the mass of the flap and slat mechanism can be divided into two processes. The first process is the kinetostatic analysis of the system which includes the determination of the forces and moments at the links. The second one is the mass estimation based on the loads acting on each element. The mass estimation is partly related to a physical motivated stress analysis and to empirical relations.
The kinetostatic analysis is part of the classical mechanics discipline and covers the determination of the loads acting on elements of e.g. a planar gear/mechanism in motion based on outer forces. Dynamic loads appear since the mechanism is in motion and they depend on the mass, mass distribution and on the acceleration of the elements, hence the kinematic analysis w.r.t. to the motion of the mechanism (location, speed and acceleration of the each element) has to be conducted prior.
As stated by Holert [54], the dynamic loads acting on the deployment mechanisms of slats and flaps are small in contrast to the outer aerodynamic loads, since the actuation speed and the accelerations in the mechanism are small. Therefore the negligence of dynamic loads for the calculation of the forces and moments acting on the elements is valid for the kinetostatic analysis of slat and flap mechanisms. The perspective here is equal to a quasi-static view without the consideration of the mass and mass distribution of the elements. Nevertheless, the kinematic analysis has to be performed prior to know the location of the elements during the deployment.
In aeronautics, structures are designed according to two design philosophies, fail-safe and safe-live. The principle in the safe-live philosophy is to ensure that no primary failure in the life cycle of the component occurs. This principle is realized by high safety factors and hence overdimensionized components. Fail-safe is realized by a redundant design of the component. The loads are sustained by independent structures and the failure of an individual

[7] www.asco.be, [88]

structure does not lead to a complete failure of the component. The individual structures are designed to be able to solely sustain the acting loads.
Both design philosophies are considered in this work. For example, for beams the safe-live and for links the fail-safe approach is employed. The distinction whether the fail-safe or safe-live philosophy is used for the components is made according to Holert [54].
The design of the components of the mechanism is focused on the fatigue behavior of the structure. Fatigue behavior of a structure is mainly dominated by the maximum inner stress. In other words, if the geometry and the outer forces are varied but the maximum inner stress is constant, than the fatigue behavior would be the same. The maximum inner stress is calculated based on the v. Mises equivalent stress. However for the sizing of a structure also crack propagation is important. To withstand also crack propagation minimum geometrical conditions are set to avoid too thin components.

2.8.1 Mass Estimation Module for Flap Mechanisms

The bearing loads are calculated based on the outer aerodynamic forces. For the kinetostatic analysis of the flap mechanism the mechanism is cut free (see Figure 20) and the equilibrium of forces and moments is set up for each component. The equations are summarized

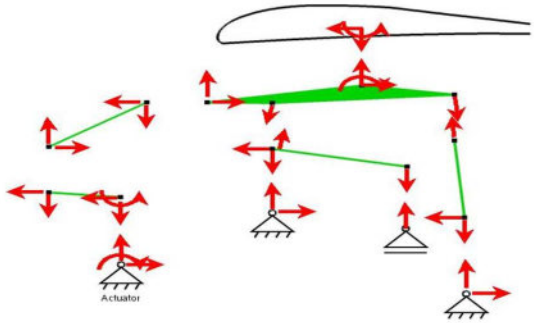

Figure 20: Sketch of the high-lift system cut free at each component. Forces and moments are illustrated as red arrows at the bearings/connections of each component.

in a linear system of equations and the system is solved with a LUPivot decomposition algorithm provided by a mathematical C-library [89]. This procedure is looped to obtain the loads for each discrete position of the mechanism during the deployment. Since the outer, aerodynamic forces are only known for discrete positions (retracted, take-off, landing), the outer forces are linearly interpolated w.r.t. the deflection angle of the flap. By this we obtain for every discrete position of the mechanism an approximated outer load.
The next step after the determination of the loads on the elements is the mass approximation that goes back on a method developed by Holert [54]. Holert developed empirical and semi-empirical (physically motivated) relationships for the mass estimation of each component in a flap mechanism. Linear, quadratic, cubic fit functions are established with empirical data of several airplanes of Airbus for the mass of rotary, linear actuators, carriage and links. The beams are sized based on a stress analysis for a straight beam. If needed for these beams flanges can also be accounted. For this type of component the normal, shear and bending stress distribution are calculated. The dimensions of the beam are assessed with material data and with the v. Mises equivalent stress. Figure 21 sketches the idealized beams for a track-linkage mechanism. In total four beams are recognized. The first beam connects the mechanism with the main element at bearing 1 and bearing 2. This beam is named in the

following main beam. It has flanges to connect the track, the actuator and bearing 2. The second beam is the track on which the carriage moves. This beam has no flanges. On the third beam the flap element is mounted and it is connected with the drive strut, the rear link and the carriage. This beam is named flap beam in the following and it has flanges. The fourth beam connects the actuator with the drive strut and it has no flanges. This beam is called actuator beam.

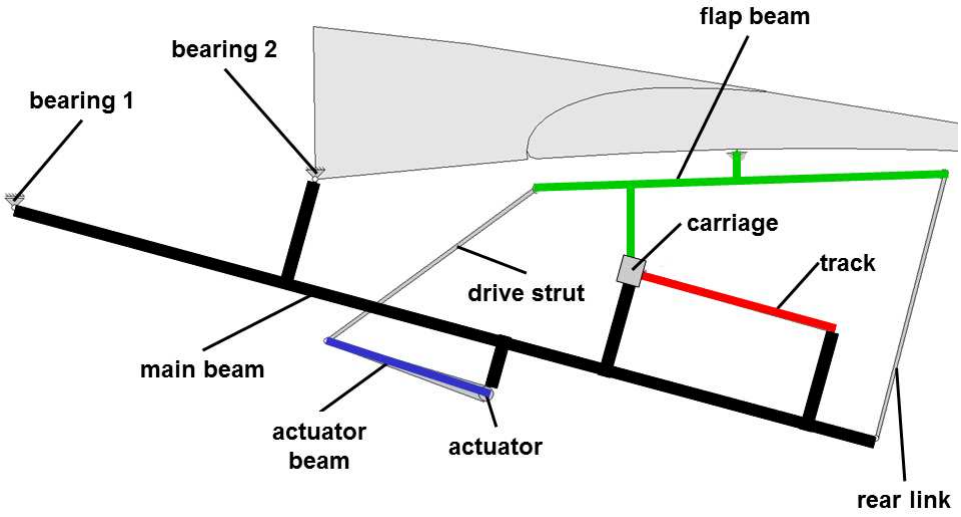

Figure 21: Sketch of the idealized beams of the track-linkage system. The high-lift system is mounted at the main element at two sketched bearings (bearing 1,2).

Now some relationships of the method developed by Holert are shown exemplarily.
First, two empirical relationships are presented to estimate the mass of a rotary actuator and of the carriage. The mass of the rotary actuator is calculated as follows:

$$m_{RA} = \lambda_{RA1} \cdot M_{RA,\max} + \lambda_{RA2}, \tag{2.34}$$

where λ_{RA1} and λ_{RA2} are constant coefficients. $M_{RA,\max}$ is the maximum of the moment acting at the actuator during deployment. The relationship to estimate the actuator mass is based on a linear fit of several actuators used on Airbus aircraft.
The mass of the carriage is approximated by:

$$m_{CA} = \lambda_{CA1} \cdot F^2_{CA,\max} + \lambda_{CA2} \cdot F_{CA,\max} + \lambda_{CA3}, \tag{2.35}$$

where λ_{CA1}, λ_{CA2} and λ_{CA3} are constant coefficients. $F_{CA,\max}$ is the maximum of the force acting on the carriage during deployment. The mass of the carriage is estimated by a quadratic fit of several carriages that fly on Airbus aircraft. The Equations (2.34) and (2.35) are presented here as published by Holert [54]. The coefficients are taken from the documentation of TEFlaMeS [72] which is not publicly accessible.
Second, the estimation of the mass of a beam is described. The geometry of the beams is defined according to DIN 1025 T1 [90]. The parameterization of the beam is shown in Figure 22. According to this figure only one parameter defines the dimension of the cross-section of the I beam. As said, the shear, normal force and bending moment distribution are calculated for each discrete position of the mechanism during deployment. Based on these distributions and by applying the hypothesis of v. Mises the parameter s_B (beam height) is determined iteratively by aiming at the maximum possible, tolerable stress in the beam

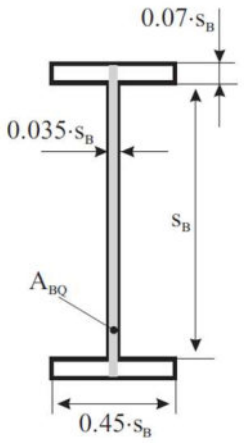

Figure 22: Sketch of the parameterized, idealized cross-section of the I beam for the mass estimation; source: Holert [54].

for the material. For each beam, including its flanges, the beam height is determined and this height is constant along the whole beam. To calculate the mass of the beam following equation is applied:

$$m_B = \lambda_B \cdot s_B^2 \cdot \rho \cdot l_B, \tag{2.36}$$

where λ_B is a constant coefficient, ρ the density of the used material and l_B the length of the beam. For a beam with flanges the length l_B includes naturally the lengths of all flanges. In contrast to a real-life design the beam is constant in its cross-section dimension along the whole beam. This simplification increases the mass of the beam component. Additionally, in a real-life application these beams would most likely not be realized by a main beam with flanges. Further on, the beam is realistically not designed with only one material. A detailed design with several materials involved can reduce the mass of the beam component. However, for a realistic design increased stresses arise (stress concentrations). These stress concentrations are located at the ends of the beams where the loads act or where the flanges are connected to the main beam. For these locations enlarged cross-sections would be considered during a realistic design and increase the mass of the beam component. According to Holert, these effects roughly compensate each other. Overall, this method aims to obtain in a simple way a beam that sustains the loads, that achieves the geometrical requirements and that is realistic in its mass. All aspects are gained by this approach according to Holert. For the detailed description of the method and the relationships for the different components refer to Holert [53, 54, 72]. The total mass of the mechanism is consequently obtained by the sum of the masses of each component.

2.8.2 Validation of Mass Estimation Module for Flap Mechanisms

For the validation of the mass estimation module the software TEFlaMeS and real aircraft data are used. The test case for the validation is the Airbus A340-600 flap mechanism at track three. The outboard flap of the Airbus A340-600 is controlled by three tracks, where track three is approximately in the middle of the outboard flap in spanwise direction. The definition of the geometry of the mechanism, the airfoil geometry, the aerodynamic loads and the mass of the components of the flap mechanism are described in the documentation of TEFlaMeS [72]. The validation Holert presents is on the basis of load distributions that

are provided by Airbus. Here the spanwise distribution of the aerodynamic loads on the flap are considered and also the load cases that drive the design of the mechanism. Hence, to check the plausibility and to validate the method, implemented by the author, the aerodynamic input data, airfoil geometry and geometry of the mechanism are all taken from the documentation of TEFlaMeS.
For the validation we start with the comparison of the input load distribution on the flap. The corresponding coordinate system is depicted in Figure 23. This figure shows a track-linkage system. Additionally, the forces and moment at the actuator and the outer aerodynamic forces and moment at the flap hinge point are sketched. The coordinate system for the forces and moment at the flap link are not body fixed to the flap. Hence, the direction of the forces in x- and z-axis are always parallel to the forces at the actuator (P_0) during the deployment of the flap. Figures 24 and 25-left show the distribution of the aerodynamic forces ($F_{x,8}$, $F_{z,8}$) and moment ($M_{y,8}$) acting on the flap versus the deflection angle of the flap. The discrete aerodynamic data set is interpolated w.r.t. the deflection angle of the flap in a linear manner. Both models are in good accordance for the force in x-direction and for the pitching moment at the flap. In the distribution of the force in z-direction differences are recognizable in the interpolated domain at moderate deflection angles. For smaller and higher deflection angels the force distribution collapses. The peaks in the forces and moment distribution for the retracted flap ($\delta_{\text{Flap}}/\delta_{\text{Flap, max}} = 0$) are related to the dive case. According to the documentation of TEFlaMeS [72] all forces are interpolated linearly w.r.t. the flap deflection angle. In the domain of moderate deflection angles for the force distribution (z-direction) the description of the documentation and the results obtained from TEFlaMeS show dicrepancies. Obviously at these moderate deflection angles a non-linear behavior is observed inbetween the predescribed discrete aerodynamic loads.
Figure 25-right and Figure 26 show the forces and moment at the actuator versus the flap deflection angle. The force and moment distributions collapse well. Only at moderate deflection angles, between the discrete settings for which the aerodynamic outer loads are given, small deviations are recognizable for the distribution of the force in x-direction and for the moment. These deviations are originated by the difference in the interpolation of the aerodynamic force in z-direction on the flap.
Overall, the forces in x-, z-direction and the moment for the flap link and the actuator of the two models agree well. Only small deviations are noticed, which are related to the interpolation of the outer forces and moment.
Since we have shown that the forces and moment for the input (flap link) and output (actuator) are reliable we can validate the mass estimation of each component. The mass estimation of the mechanism is conducted based on the forces and moments acting on the components. Table 5 summarizes the percentual variation of the estimated mass of each component of the flap mechanism w.r.t. to the overall mass of the mechanism for the real aircraft. The girders comprise the flap beam and the track. The rods cover the drive strut and the rear link. In the actuator mass the mass of the actuator beam is comprised.
Pronounced deviations are recognized between the masses for girders, joints and rods predicted by TEFFlaMeS and the mass estimation tool. These deviations are related to a different implementation of the two tools. The tools differ in the way which parts of the components are covered by which component. For example, from the documentation of TEFFlaMeS it could not be fully verified which part of the joints are covered in the mass of the joints, in the mass of the girders and in the mass of the rods, respectively. The definitions of the mass estimation of joints, girders and rods are followed, but how the masses are divided is not fully identical for both methods.
In total, we see that the mass estimation tool overpredicts the total mass of the mechanism

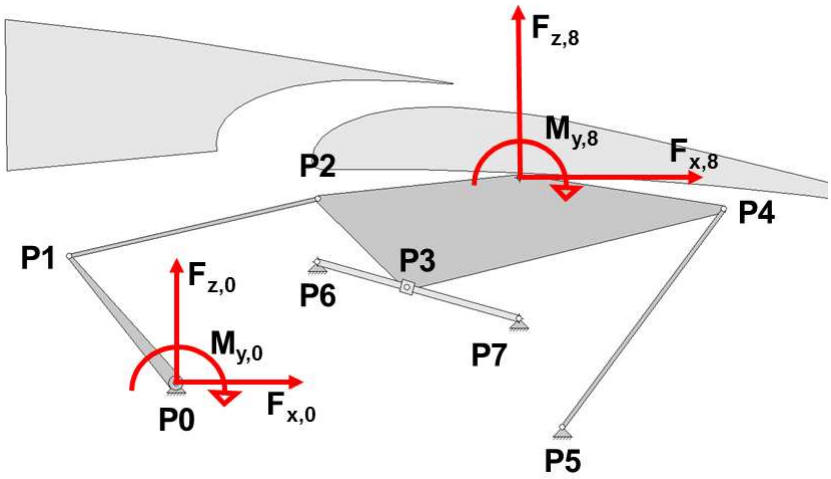

Figure 23: Illustration of the coordinate system for the loads at the flap and the actuator.

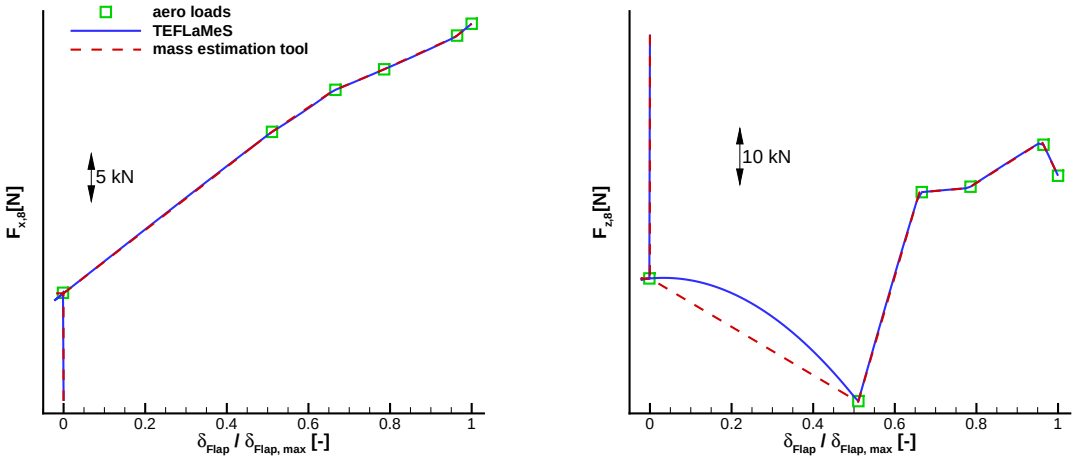

Figure 24: Aerodynamic force in x-direction and z-direction at the flap link.

by 7.4%. The overprediction of the total mass by TEFFlaMeS is less (5.4%). In total the predictions of both methods for the overall mass are acceptable, especially when taking into account that the method can be classified as a low-fidelity method. When considering the individual masses of each component of the mechanism, the deviations are substantial, refer to Table 6. This table shows the variation of the individual mass of the components w.r.t. to the corresponding mass of the real aircraft. The mass of the rods are drastically underestimated by the mass estimation tool, but this is related to the above mentioned implementation issue. The components that cover percentual three-fourths of the overall mass, i.e. beam and actuator are in quite good accordance. The carriage is significantly overestimated.
During this investigation it was found that the load cases related to the retracted flap setting are insignificant for the mass estimation of the flap mechanism. The negligence of these load cases leads to a decrease of the mass of the mechanism by 0.01%.
Overall, the variations in the masses of the components between the two methods and the real aircraft data are sufficiently accurate for a low-fidelity approach. These achievements have to be seen in the context, that the relationships developed by Holert are founded on a data base provided by Airbus. The significance of this validation is therefore limited. But the plausibility of the methods and their implementation is verified. To enhance the signif-

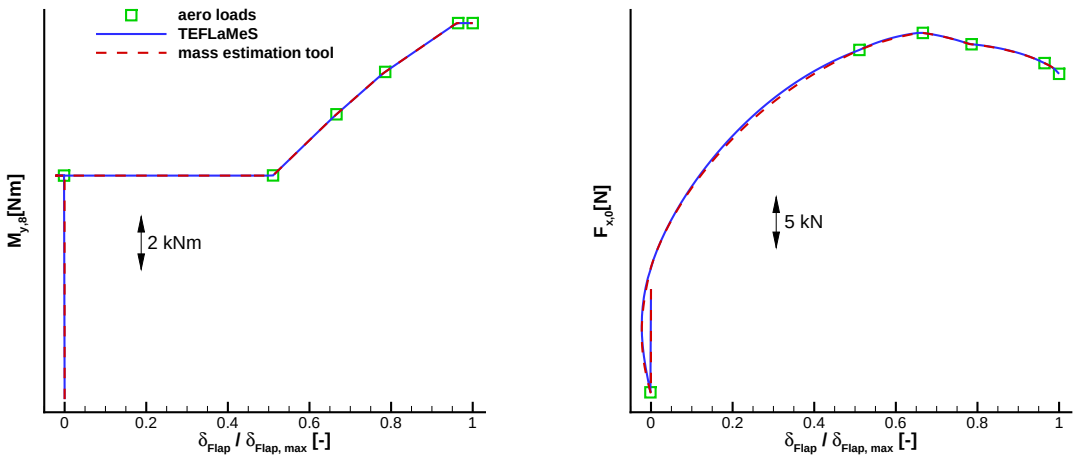

Figure 25: Left: pitching moment acting at flap link. Right: force in x-direction acting at the actuator.

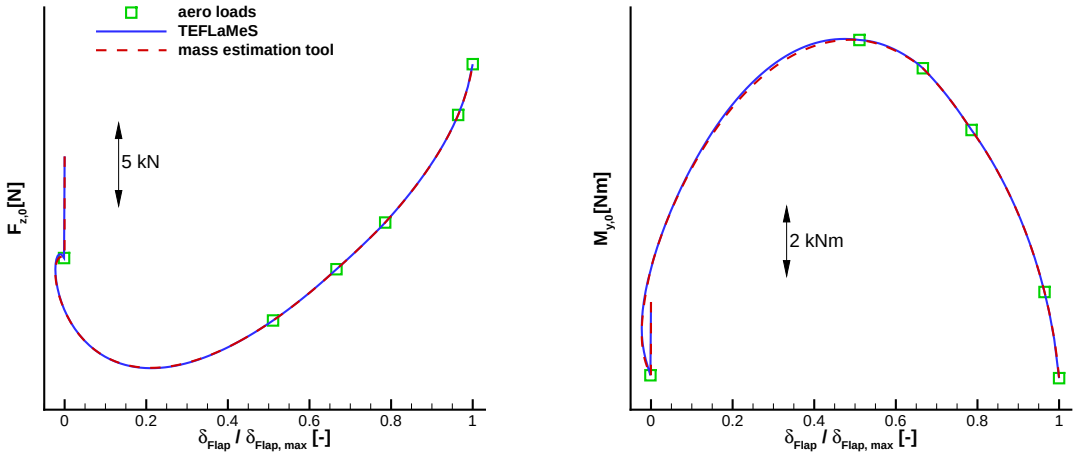

Figure 26: Force in z-direction and torque acting on the actuator.

icance of this validation an aircraft of Boeing should be used, but due to lack of sufficient data this is not possible.
In the documentation of TEFlaMeS it is stated that this method/tool is applicable on systems/airplanes that are in the range of Airbus A320 to Airbus A340, where an accuracy of $+/-15\%$ can be expected. Further on for optimization purposes, the trends of the mass estimation has to be reflected well, which is the case for this method according to Holert. We can summarize that by the same given input data (geometry, discrete load distribution) we receive for both models output data (e.g. forces, moments at the actuator, mass of the components) that are in good accordance.

2.8.3 Mass Estimation Module for Slat Mechanisms

The kinetostatic analysis is performed to obtain the loads on the elements of the slat mechanism based on the outer aerodynamic loads. The elements considered here are the constant radius track, the rollers and the actuator, for illustration refer to Figure 4. The stress analysis

Table 5: Percentual part of each component of the overall mechanism w.r.t. the overall mass of the mechanism of the real aircraft.

Component	real a/c [%]	TEFFlaMeS [%]	Mass estimation tool [%]
Beam	55.3	58.5	58.9
Girders	6.6	6.3	7.7
Joints	-	3.7	5.5
Rods	3.6	2.7	1.5
Carriage	10.4	14.3	14.0
Actuator	19.2	19.9	19.8
Consumbles	4.9	-	-
Sum	100.0	105.4	107.4

Table 6: Percentual deviation of the mass for each component predicted by the mass estimation tool compared with the corresponding component of the real aircraft.

Component	$\Delta m_{\text{Mass estimation tool, real a/c}}$
Beam	+6.7
Girders	+15.4
Joints	-
Rods	-58.6
Carriage	+33.8
Actuator	+3.2
Consumbles	-
Total mass	+7.4

of the constant radius track is conducted only at four discrete, critical cross-sections of the slat. The regarded cross-sections are at the head of the track, at the position of the actuator and at the positions of the rollers. It is assumed that each pair of rollers (upper and lower roller) lay in one cross-section plane. The inner stresses (normal, shear and bending stress) for these cross-sections are calculated. The dimension of the pi-section (refer to Figure 27) is assessed with the v. Mises equivalent stress and material data. A target equivalent stress is pre-defined based on the material to assess the dimension of the pi-section. The rollers are sized by a contact stress analysis. The estimation of the mass of the pinion drive (rotary actuator) follows the approach of Holert. In the retracted position, the estimation of the pinion drive is deactivated since here breaks are applied. The pi-section is scaled in this work only with one parameter for the simplification of the automated process to size the section, similar to the procedure described above for the beam of the flap mechanism. Further on, we assume that the pi-section does not vary along the arc track. In a realistic design process the pi-section is not scaled but varied based on the acting stress distribution and along the arc track the size of the pi-section may vary as well.
The current approach assumes that the fatigue behavior of the beam remains constant when the target stress (v. Mises equivalent stress) in the component is met for varied geometry

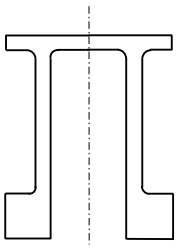

Figure 27: Sketch of the cross-section of the slat track beam, namely pi-section.

and outer forces. The fatigue behavior depends on the maximum inner stress which is kept constant. However for the sizing of the component additionally crack propagation is important. By this approach only the fatigue behavior and not the behavior in regard of crack propagation of the beam is analyzed. The analysis with respect to crack propagation is more sophisticated and would require a more elaborated tool.
Typical relations for the pi-section and as well the geometry of the track which are used for the initial geometry are provided by ASCO industries.
For the validation process real aircraft data, geometrical data and corresponding aerodynamic loads were unfortunately not publically available. Therefore the validation of this module is done by tests concerning the plausibility of the results in close collaboration with ASCO industries. By these tests it was shown that the module works properly. For example the force vectors acting on the slat track, rollers and torque at the actuator were well distributed w.r.t. length and direction. The geometry and the material of the slat track used in this work are representative for a commercial aircraft and were provided by ASCO industries [88].

2.9 Flight Mechanics - Aircraft Performance for Take-Off and Landing

Aircraft performance is a subdivision of flight mechanics and it is used in this work to assess the high-lift system according to its aerodynamic properties and based on its system mass (the mass of the flap and slat mechanisms). Maneuvers, influence of gusts and lateral movement of the aircraft are not considered in this thesis. The aircraft performance is evaluated by the take-off and landing distance. Schematics of the take-off and landing procedure are shown in Figures 28, 30. Note, for the estimation of the take-off and landing distance we use the quasi three-dimensional aerodynamic coefficients in the line-of-flight system. The stall speed is calculated based on the maximum lift coefficient. However, maximum lift is predicted for all samples with the same free stream conditions. We assume that small variations in the Mach and Reynolds number have minor influence on the resulting aerodynamic data, like maximum lift or lift polar curve. The ground effect on the aerodynamics of the high-lift system is not accounted within this thesis: According to the textbook of McLean [91] the ground effect depends on the height of the airfoil above the ground. The aircraft from its characteristics, like wing span, wing size, length of landings gears etc. is considered as constant in this work. Hence, the height of the airfoil above the ground does not change and thus the main influence quantity for the ground effect is constant. Subsequent the ground effect does not play a significant role and can be neglected in this work.

2.9.1 Take-Off Run

Figure 28 schematically shows the take-off run. The first phase of the take-off procedure is

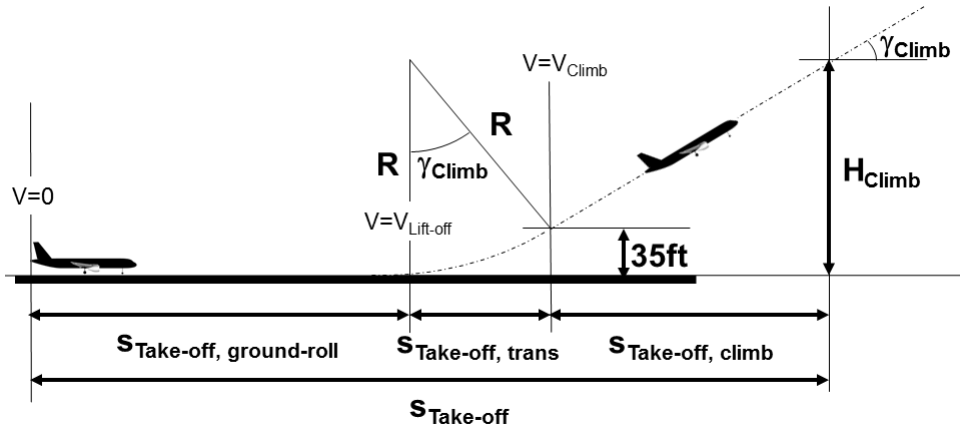

Figure 28: Schematic of the take-off procedure.

the **ground-roll**, which is defined as the distance from standstill until lift-off. The evaluation of the flight mechanics uses the two-dimensional aerodynamic data converted into quasi three-dimensional data. The geometrical relationships for gear and tail are not defined, thus tail strike is not a limiting case here and hence the rotation phase during ground-roll is neglected. We assume that the airplane rolls until lift-off without any change in the angle of attack. The lift-off speed is approximated based on the stall speed of the take-off configuration (refer to Table 1 which includs the safety factors derived from the regulations).
Subsequent to the ground-roll the **transition to climb** phase takes place. In this phase the airplane accelerates from the lift-off to the climb speed. This phase is approximated by an arc track. To estimate the radius of the arc track the load factor (n) is set to a standard value[8] for commercial aircraft and it reads $n = 1.2$. This phase ends when the aircraft reaches a height of 35ft above the runway level. The **climb phase** follows the transition phase and ends at the height H_{Climb}. We assume that during take-off ground-roll the thrust remains constant.
Following, the formulas are presented to calculate the components of the take-off distance, refer to Raymer[74]. The basic equation to calculate the distance of accelerating a body from the speed v_1 to speed v_2 is:

$$s = \int_{v_1}^{v_2} \frac{v}{a} dv, \tag{2.37}$$

where a is the acceleration and v the speed of e.g. the aircraft. To simplify the integration of Equation (2.37) a mathematical trick is used. Hereby, the integration is done with respect to v^2 instead of v. Then the integration reads,

$$s = \frac{1}{2} \int_{v_1}^{v_2} \frac{1}{a} d(v^2), \tag{2.38}$$

The acceleration of the aircraft is generally derived from the force balance at the aircraft and it reads:

$$a = \frac{g}{W} \left[T - D - \mu_r \left(W - L \right) \right], \tag{2.39}$$

[8] Raymer[74] page 488

where g stands for the gravitational constant, W for weight of the aircraft, T for the thrust force, D for the aerodynamic drag force, μ_r is the friction coefficient[9] and L is the aerodynamic lift force. In the following the lift force, drag force, thrust force, the weight of the aircraft and friction coefficient are constant for each segment. The integration of formula (2.38) leads then to following formula for the **ground-roll** distance during take-off from stand still to the lift-off speed ($v_{\text{Lift-off}}$):

$$s_{\text{Take-off, ground-roll}} = -\frac{1}{\rho \cdot g} \cdot \frac{1}{C_2} \cdot \ln\left(1 - \frac{C_2}{C_1} \cdot \frac{\rho}{2} \cdot v^2_{\text{Lift-off}}\right), \tag{2.40}$$

ρ stands for the density. C_1 and C_2 are defined as follows:

$$C_1 = \frac{T}{W} - \mu_r, \tag{2.41}$$

$$C_2 = \frac{1}{\frac{W}{S}} \cdot \left[C_{\text{D, quasi 3D}}(AoA = 0.0) - \mu_r \cdot C_{\text{L, 2.5D}}(AoA = 0)\right]. \tag{2.42}$$

$\frac{T}{W}$ is the thrust to weight ratio, μ_r is the friction coefficient, $\frac{W}{S}$ is the wing loading, $C_{\text{D, quasi 3D}}(AoA = 0.0), C_{\text{L, 2.5D}}(AoA = 0.0)$ are the drag and lift coefficient at zero angle of attack.

For the calculation of the distance for **transition to climb** we distinguish two cases. In the first case the aircraft flies on the arc track until the obstacle height of 35ft is reached. Whereas for the second case, the obstacle height is reached after the aircraft leaves the arc track and climbs with a constant climb angle. The vertical distance in which the aircraft climbs with a constant climb angle is indicated by H_2. The two mentioned cases are illustrated in Figure 29, where only the transition phase of the take-off run is shown. The distance for the transition to climb phase is calculated as follows:

$$s_{\text{Take-off, trans}} = \begin{cases} R \cdot \sin\left(\gamma_{\text{required}}\right), & \text{if} \gamma_{\text{required}} \leq \gamma_{\text{Climb}} \\ R \cdot \sin\left(\gamma_{\text{Climb}}\right) + \dfrac{H_2}{\tan\left(\gamma_{\text{Climb}}\right)}, & \text{if} \gamma_{\text{required}} > \gamma_{\text{Climb}} \end{cases}, \tag{2.43}$$

where the radius of the arc track is R, γ_{required} is the required glide path angle and γ_{Climb} is the climb path angle.

The required glide path angle and the climb path angle are defined as follows:

$$\gamma_{\text{required}} = \cos\left(1.0 - \frac{35\text{ft}}{R}\right), \tag{2.44}$$

$$\gamma_{\text{Climb}} = \frac{T}{W} - \frac{C_{D,\text{quasi 3D,climb}}}{C_{L,2.5D,\text{climb}}}. \tag{2.45}$$

The required glide path angle depends on the obstacle height and the radius of the arc track. The climb path angle is determined by the thrust to weight ratio and the aerodynamic performance of the aircraft during climb. The radius of the arc track is a function of the speed and the load factor. The radius of the arc track R is defined as:

$$R = \frac{v^2_{\text{Trans}}}{(n-1) \cdot g}. \tag{2.46}$$

[9] $\mu_r = 0.04$, according to Raymer[74]

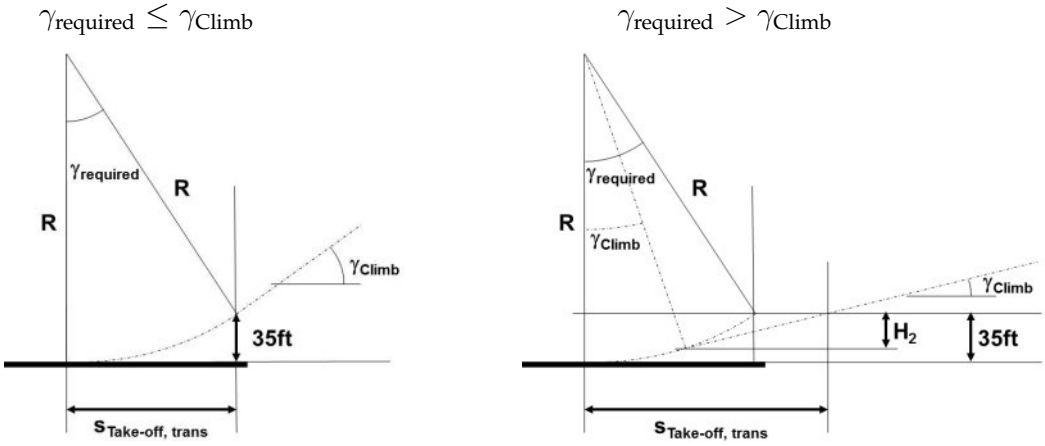

Figure 29: Schematic of the two different transition cases for the take-off procedure.

In the second case the vertical distance (H_2) is defined as follows:

$$H_2 = 35\text{ft} - R\left[1.0 - \cos\left(\gamma_{\text{Climb}}\right)\right]. \tag{2.47}$$

$$\tag{2.48}$$

At height ($35\text{ft} - H_2$) the aircraft transits from the arc track to the climb path with constant climb angle.
Finally, the formula for the distance of the **climb phase** reads:

$$s_{\text{Take-off, climb}} = \frac{H_{\text{Climb}} - 35\text{ft}}{\tan\left(\gamma_{\text{Climb}}\right)}. \tag{2.49}$$

A constant climb path angle is foreseen and this phase starts at a height of 35ft and ends at the height H_{Climb}. For the height H_{Climb} three different values are analyzed in this thesis (400ft, 1500ft, 3000ft).
The **overall take-off distance** is finally the summation of the distances for ground-roll, transition and climb phases.

$$s_{\text{Take-off}} = s_{\text{Take-off, ground-roll}} + s_{\text{Take-off, trans}} + s_{\text{Take-off, climb}}. \tag{2.50}$$

Finally the flight speeds during take-off are calculated as follows:

$$v_{\text{Lift-off}} = v_{\text{Stall, 1g, take-off}} \cdot 1.1, \tag{2.51}$$

$$v_{\text{Climb}} = v_{\text{Stall, 1g, take-off}} \cdot 1.13, \tag{2.52}$$

$$v_{\text{Trans}} = \frac{v_{\text{Lift-off}} + v_{\text{Climb}}}{2}. \tag{2.53}$$

The speed for transition is in accordance with the text book of Raymer[10]. These speeds depend on the stall speed of the take-off configuration, which reads:

$$v_{\text{Stall, 1g, take-off}} = \sqrt{\frac{2}{\rho \cdot C_{\text{L, 2.5D, max, take-off}} \cdot \left(\frac{W}{S}\right)_{\text{Take-off}}}}. \tag{2.54}$$

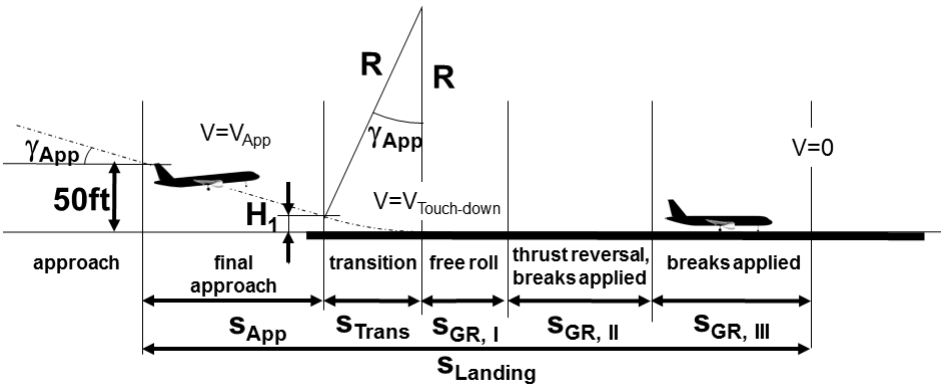

Figure 30: Schematic of the landing run.

2.9.2 Landing Run

Figure 30 depicts the landing run. The landing distance analysis considers first the **final approach** phase. A typical glide slope angle of $\gamma_{App} = 3°$ for commercial airliners[11] is defined for the approach and the final approach phase. The final approach phase starts at the obstacle height of 50ft and ends when the **transition to flare** phase begins. The airplane decelerates in the transition to flare phase from the final approach to the touch-down speed. The flight path is estimated by an arc track. To estimate the radius of the arc track the load factor is again set to the standard value[12] of $n = 1.2$. The **ground-roll** follows the transition phase. We separate the ground-roll phase into three parts.
Part I ($s_{\text{GR, I}}$): free ground-roll without brakes and thrust reversal for several seconds ($t_1 = 2s$)[13].
Part II ($s_{\text{GR, II}}$): ground-roll with breaks applied and thrust reversal activated if the speed of the aircraft is higher than 50kt. Thrust reversal is set to $T_{\text{rev}} = -0.45 \cdot T_{\text{Take Off}}$[14]. Breaking is considered by an increased friction coefficient[15].
Part III ($s_{\text{GR, III}}$): ground-roll with breaks applied until standstill of the airplane, no thrust reversal is accounted ($T = 0$N).
In the following the formulas to calculate the landing distance are presented. We start with the formula for the **final approach** phase:

$$s_{\text{App}} = \frac{50\text{ft} - H1}{\tan\left(\gamma_{\text{App}}\right)}. \tag{2.55}$$

The final approach is evaluated here from the obstacle height of 50ft until the height H_1 at which the transition phase starts. The glide slope angle is constant for this phase. The height H_1 is a function of the radius R for the arc track of the transition phase and the glide slope angle of the final approach phase. Although a constant glide slope angle is applied the distance for the final approach varies with the maximum lift coefficient. The height H_1 reads:

$$H_1 = R\left[1 - \cos\left(\gamma_{\text{App}}\right)\right]. \tag{2.56}$$

[10] Raymer [74] page 487
[11] Rudolph [5] page 41
[12] Raymer [74] page 490
[13] medium value taken from Raymer [74] page 490
[14] medium value taken from Raymer [74] page 491
[15] $\mu_r = 0.4$, according to Raymer[74]

The formula to calculate the radius for the transition phase reads:

$$R = \frac{v_{\text{Trans}}^2}{(n-1)\cdot g}. \tag{2.57}$$

The distance for **transition to flare** is calculated according to following formula:

$$s_{\text{Trans}} = R \cdot \sin\left(\gamma_{\text{App}}\right). \tag{2.58}$$

The **ground-roll** is separated into the three mentioned parts.
The formula to calculate Part I ($s_{\text{GR, I}}$) reads:

$$s_{\text{GR, I}} = v_{\text{Touch-down}} \cdot t_1. \tag{2.59}$$

For this part we follow Raymer [74] who considers a constant speed for this part, i.e. the influence of the aerodynamic drag force and the friction drag are not accounted for this part.
The formula to calculate Part II ($s_{\text{GR, II}}$) is based on the Equation (2.38) and it reads:

$$s_{\text{GR, II}} = \begin{cases} 0m, & v_{\text{Touch-down}} \leq 50\text{kt} \\ \frac{1}{\rho\cdot g}\cdot\frac{1}{C_2}\cdot\left[\ln\left(1-\frac{C_2}{C_1}\cdot\frac{\rho}{2}\cdot v_{\text{Touch-down}}^2\right)\dots\right. & \\ \left.\dots-\ln\left(1-\frac{C_2}{C_1}\cdot\frac{\rho}{2}\cdot(50\text{kt})^2\right)\right], & v_{\text{Touch-down}} > 50\text{kt} \end{cases}. \tag{2.60}$$

The formula to calculate Part III ($s_{\text{GR, III}}$) is again based on Equation (2.38) and it reads:

$$s_{\text{GR, III}} = \frac{1}{\rho\cdot g}\cdot\frac{1}{C_2}\cdot\ln\left(1-\frac{C_2}{C_1}\cdot\frac{\rho}{2}\cdot v_{\text{GR,III}}^2\right) \tag{2.61}$$

$$v_{\text{GR,III}} = \min\left(50\text{kt}, v_{\text{Touch-down}}\right) \tag{2.62}$$

For the definition of the constants C_1 and C_2 for Part I and Part II refer to Equations (2.41), (2.42). The overall ground-roll distance is the sum of the three parts:

$$s_{\text{GR}} = s_{\text{GR, I}} + s_{\text{GR, II}} + s_{\text{GR, III}} \tag{2.63}$$

The **overall landing distance** is a summation of the three phases of the landing run:

$$s_{\text{Landing}} = s_{\text{App}} + s_{\text{Trans}} + s_{\text{GR}}. \tag{2.64}$$

The various flight speeds are calculated as follows:

$$v_{\text{App}} = v_{\text{Stall, 1g, landing}} \cdot 1.23, \tag{2.65}$$

$$v_{\text{Touch-down}} = v_{\text{Stall, 1g, landing}} \cdot 1.15, \tag{2.66}$$

$$v_{\text{Trans}} = \frac{v_{\text{App}} + v_{\text{Touch-down}}}{2}. \tag{2.67}$$

The speed for transition is in accordance with the text book of Raymer[16]. These speeds depend on the stall speed of the landing configuration, which reads:

$$v_{\text{Stall, 1g, landing}} = \sqrt{\frac{2}{\rho\cdot C_{\text{L, 2.5D, max, landing}}\cdot\left(\frac{W}{S}\right)_{\text{Landing}}}}. \tag{2.68}$$

[16] Raymer [74] page 490

3 Results and Discussion

This chapter presents and analyses the data that are gained with the previously described process chains within various optimizations. In the first place the generation of data is explained, e.g. how many optimizations were conducted with which kind of involved disciplines and constraints. Note, for this thesis the optima of the various optimizations are not of high interest, since for the analysis of the interrelation of the disciplines the data samples are merged together to one single overall data base; the origin of each sample and its quality in the underlying optimization are irrelevant for this point of view. Therefore these optima are only mentioned briefly and they are not discussed. In Section 3.2 the distribution of the data samples is explained for each sub data set. The results in this section are based on the previously mentioned optimizations, but here the notation "sub data set" is introduced. A brief explanation of the difference between the notation optimization and sub data set is given here now. The data base of the each optimization covers all samples that are generated within the corresponding optimization run. In contrast the sub data sets cover not all data samples of the underlying optimization. For example data samples are omitted because the size of parameter spaces has changed. Additionally, all data samples that form the sub data sets are re-evaluated by the flight mechanics module to ensure that all samples are assessed with the same properties for the take-off and landing run. This means that the values for the flight mechanics performance may differ between the optimizations and the sub data sets. The aerodynamic data of each sample that resulted from the numerical computations (CFD) within the optimizations are untouched. All sub data sets and their individual samples are compared with the baseline configuration. The baseline configuration is a highly sophisticated, elaborated industrial developed design for a commercial aircraft in service provided by industry. In Section 3.3 all data samples of the sub data sets are merged together. Additionally, data samples are selected that show beneficial behavior concerning their flight mechanics performance. These samples are discussed in depth in the subsequent sections from the perspectives of the different involved disciplines (kinematics: Section 3.4, aerodynamics: Section 3.5, flight mechanics Section 3.6 and mass estimation of mechanisms: Section 3.7).

3.1 Generation of Data

The process chains described in the previous chapter were used to perform optimizations of the high-lift system. Table 7 summarizes the main properties that were used during these various optimizations. The table reflects for each optimization: First, the upper bounds of the slat deflection angle for take-off and landing. Second, the thrust ratio of ground-roll and climb during take-off is shown. Third, whether or not the mass of the slat and flap mechanism were considered during the evaluation of the flight mechanics. Fourth, until which height the take-off was evaluated. For illustration of the take-off height, refer to Figure 28.

Table 7: Overview of main properties of the different optimizations.

Opt.	$\delta_{\text{Slat, max}}$ for take-off [deg]	$\delta_{\text{Slat, max}}$ for landing [deg]	$\frac{T_{\text{Take-off, ground-roll}}}{T_{\text{Take-off, climb}}}$	MTOW = const. & MLW = const.	Climb height H_{Climb}	Consideration of kinematical relationships for the flap
1	30	30	0.7	no	400ft	yes
2	30	30	0.7	no	1500ft	yes
3	24	24	1.0	yes	1500ft	yes
4	24	24	1.0	no	1500ft	yes
5	24	24	1.0	no	1500ft	yes
6/7	24	24	1.0	yes	1500ft	no

Fifth, whether or not the kinematical relationships for the flap were accounted.
The setting of the slat is influenced by the maximum slat deflection angle. The flap setting is affected whether or not the kinematical relationships for the flap are considered. All other properties of Table 7 are related to the flight mechanics evaluation and can easily be changed within a postprocessing step after the data base is generated.
After the optimizations 1 and 2 were accomplished, clashes of the constant radius track with the outer wing skin for the retracted slat were detected. Therefore, the parameter spaces for the parameters related to the maximum slat deflection were reduced for the further generation of data to avoid unrealistic designs.
Five optimizations (1-5) were generated with the previously described most elaborated process chain (refer to Section 2.3). The mass of the mechanisms was always evaluated for these five optimizations but not necessarily considered for the evaluation of the take-off and landing performance. This was done to ensure that the optimizer is not focusing on the influence of the mass of the mechanisms on the flight mechanics performance. Further on, the idea is to have samples optimized for both approaches with and without the consideration of the mass concerning their flight mechanics performance. The computational effort for the evaluation of the mass of the mechanisms is compared to the aerodynamic simulations negligible. Hence, no significant additional computational time has to be tolerated when the mass is evaluated without using it for the assessment of the flight mechanics performance during the single optimizations. For optimization 3 the maximum take-off weight and the maximum landing weight were defined to be constant during the evaluation of the flight mechanics.
Optimizations 6/7 were generated with the aerodynamic process chain (refer to Section 2.3). Hence, the kinematical relationships of the trailing edge mechanism were neglected and naturally the masses of the aircraft during take-off and landing were constant. The settings for the CFD solver were not changed during the evaluation of these seven optimizations. For the optimizations the Subplex [66] was used as algorithm. For the optimization algorithm the standard settings for the Subplex algorithm were used and for all optimizations the same settings were applied. From experience, substantial improvements are achieved during the first two Subplex cycles at the beginning of the optimization run. Figure 31-left shows the convergence behavior of the objective function for optimization 1 for which four complete Subplex cycles were performed. According to this figure, substantial improvements for the

objective function value are achieved during the first Subplex cycle. Within the second Subplex cycle strong variations in the objective function value are recognizable, but the improvements of the objective function value are small. Thereafter, the objective function value is only minorly improved and also the variations in the objective function value decrease. This means, the objective function value roughly levels out. Now, we take into account the convergence behavior of e.g. parameter 3, refer to Figure 31-right. This parameter exemplarily shows a representative behavior for the parameters. This plot shows the parameter value versus the iteration count during data generation. Within each cycle an exploration phase and a phase with merely constant parameter value are recognized. The exploration phase is noticed by the spread data samples, e.g. refer approximately to iteration #60, #180 and #390 in Figure 31. The peaks in the values of the parameters of each exploration phase reduce while the Subplex cycle number increases. After each exploration phase the parameter value is constant. The important information for convergence behavior are the parameter values at the beginning and at the end of each cycle. In the first Subplex cycle the parameter value is changed significantly. The parameter value drops. In the second Subplex cycle the parameter value changes not that distinctly any more but still a variation is recognized. Thereafter, the changes are insignificant and the parameter value levels out.
For reasons of computational effort, optimizations are not necessarily performed by more than two Subplex cycles to achieve substantial improvements. As shown, the variations in the objective function and in the parameter values are minor after two Subplex cycles. As conclusion, we can state that after two Subplex cycles the optimizations achieve a satisfying level of convergence.
Besides optimization 5, all other optimizations were started from the baseline configuration with at least two Subplex cycles. Optimization 5 was generated by a restart at the best sample of a previously conducted optimization and it was performed only one full Subplex cycle.

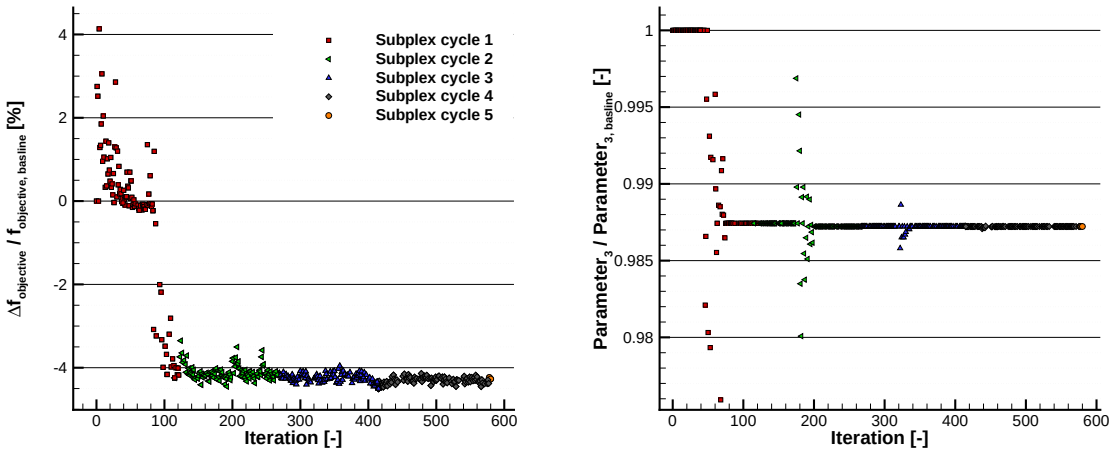

Figure 31: Left: history of the objective function for optimization 1. Objective function according to Table 8 optimization 1.
Right: history of parameter 3 for optimization 1.

Table 8 shows the definition of the objective function used for the optimizations. For optimization 1 the sum of the distances were equally weighted and it forms the objective function. For optimizations 2 to 5 the objective function was formed with the equally weighted normalized sum of the take-off and landing distance. Optimization 6 was performed to

Table 8: Overview of the definition of the objective function for the different optimizations.

Optimization	$F(\vec{x})$
1	$\frac{1}{2} \cdot \left(s_{\text{Landing}} + s_{\text{Take-off}}\right)$
2 - 5	$\frac{1}{2} \cdot \left(\frac{s_{\text{Landing}}}{s_{\text{Landing, baseline}}} + \frac{s_{\text{Take-off}}}{s_{\text{Take-off, baseline}}} \right)$
6	$s_{\text{Take-Off}}$
7	s_{Landing}

achieve optimal high-lift setting for take-off and optimization 7 to gain the optimal landing setting. Hence, the objective function was formed only by the distance that is relevant for the setting.
For optimizations 3 to 5 constraints were implemented to penalize the loss in take-off and/or landing performance in comparison to the performance of the baseline configuration. These constraints were implemented to avoid that gains in the landing performance can trump the loss in the take-off performance and vice versa. For such configurations the objective function value reflects an improvement in the overall performance (blended take-off and landing performance) in comparison to the baseline configuration. However, the configuration shows only in one component of the overall performance and blended objective function an improvement, respectively. When the constraints are active, these samples are artificially worsened and the overall performance does not show a gain in comparison to the baseline configuration anymore. These constraints are considered by the penalty method, refer to Section 2.1. The constraints are implemented to force the optimizer to head for improvements both for take-off and landing.

3.2 Distribution of Data

In the following, the origin of the overall data base and its distribution are qualitatively discussed. The overall data base is a compilation of six sub data sets. These six sub data sets are based on the seven optimizations, described in the previous section. In contrast to the optimizations, the sub data sets does not cover all samples that are generated during the optimizations due to a parameter space shrinking for the deflection angle of the slat element.

The nomenclature of the sub data sets is similar to the nomenclature of the optimizations, meaning sub data set 1 corresponds to optimization 1 etc.. The only exception forms sub data set 6, which comprises the optimizations 6 and 7. To have a comparable overall data base all samples of the optimizations were postprocessed with the same properties. Table 9 summarizes these properties. This postprocessing step covers simply the re-evaluation of the flight mechanics performance of the aircraft during take-off and landing based on the aerodynamic, integral coefficients of each data sample. Additionally, for each data sample the parameter values of the slat deflection angle for take-off and landing were checked. Subsequently, data samples were omitted that are outside the finally defined parameter spaces. In the following the sub data sets only cover the postprocessed data samples of the optimizations, which are within the parameter spaces shown in Table 9.

In the following, the sub data sets are discussed according to their main properties and how

Table 9: Main properties used to postprocess the overall data base.

$\delta_{\text{Slat, max}}$ for take-off [deg]	$\delta_{\text{Slat, max}}$ for landing [deg]	$\frac{T_{\text{Take-off, ground-roll}}}{T_{\text{Take-off, climb}}}$	MTOW = const. & MLW = const.	Climb height H_{Climb}
24	24	1.0	yes	1500ft

these impact the distribution of data samples. Let's start with the discussion of sub data sets 1 and 2.

3.2.1 Sub Data Sets 1 & 2

These sub data sets were generated during a pre-study (optimizations 1 and 2). During this pre-study the objective function, the boundary condition for climb (climb height) and also the parameter spaces were defined differently in comparison to the definitions shown in Table 9. For these sub data sets various data samples are omitted during postprocessing due to the shrinking of the parameter spaces for the slat deflection angle for take-off and landing. During the generation of these two sub data sets the main difference between them is the height until the climb phase is evaluated. Additionally, the evaluation of the objective function value differs. For sub data set 1 the distances were not normalized for the objective function, whereas for sub data set 2 the distances were normalized with the distances of the baseline configuration. MTOW and MLW were adapted according to the mass of the mechanisms during the generation of the samples. The thrust during ground-roll at take-off was reduced by roughly 30% in contrast to the thrust during climb, i.e. a flex thrust procedure was performed. Figure 32 shows the distribution of the samples of sub data sets 1 and 2. These two sub data sets have strongly clustered samples for improved landing performance but with reduced take-off performance compared to the baseline configuration. No sample is found that improves the take-off performance compared to the baseline configuration for sub data sets 1 and 2. The clustering of the samples of the sub data set 2 is located at shorter take-off distances. The overall improvement for the landing distance is higher for sub data set 2 than for sub data set 1.
To understand why these sub data sets are not heading towards improved take-off performance for the currently applied criteria (refer to Table 9), we have to take into account the boundary conditions of the flight mechanics during data generation. For sub data set 1 the take-off distance, that is covered by the objective function, is evaluated up to a climb height of 400ft. Additionally, the thrust for ground-roll was reduced in the evaluation of the take-off run for the flight mechanics module (flex thrust procedure). Therewith, the ground-roll dominates the take-off distance during data generation. The ground-roll covers roughly 69% of the overall take-off distance, whereas for higher thrust setting and a climb altitude of 1500ft the ground-roll covers only 32% of the overall take-off distance. Hence, the focus of sub data set 1 lies during data generation on a reduction of the ground-roll distance instead of a decrease of the climb distance. A performance loss in the climb phase affects the overall take-off distance for this scenario to a small extend. The aircraft takes off after a shorter distance, but climbs with a shallower climb angle. However, it has to be stated here, that the bulk data of the underlying optimizations is not shown in the graph. The bulk data lies outside the finally defined parameter space for the slat deflection angle during take-off and

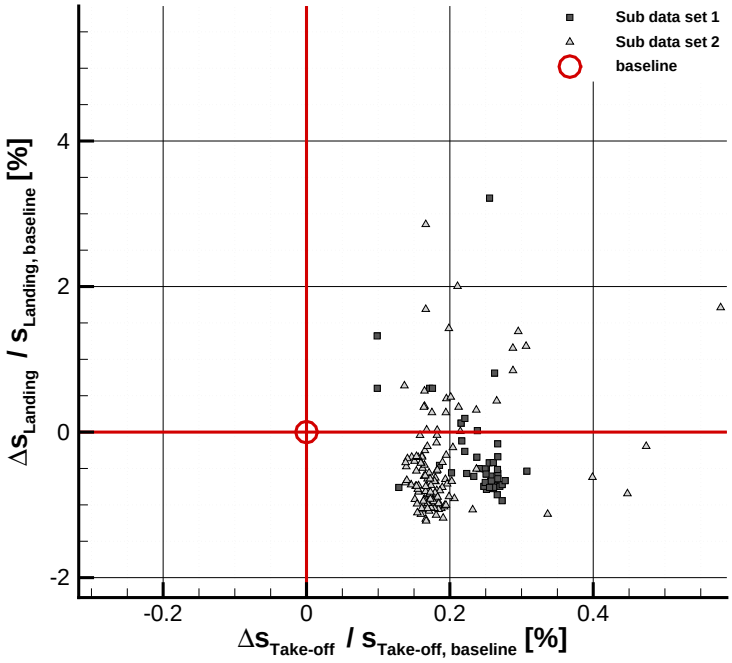

Figure 32: Distribution of samples of sub data sets 1 and 2 for percental variation of the normalized landing distance versus the percental variation of the normalized take-off distance. Both MTOW and MLW are constant. Data samples are postprocessed according to Table 9.

landing used for the postprocessing step. Consequently, these data samples are omitted and not covered by the sub data sets. This holds also for the optimum of the optimization 1, which is omitted during postprocessing.
For sub data set 2 a similar scenario is recognized, however the climb phase was evaluated until 1500ft during data generation. The results show again a higher impact of the ground-roll distance compared to the climb distance on the overall take-off distance. The ground-roll covers roughly 42% of the overall take-off distance, whereas for higher thrust setting the ground-roll covers only 32% of the overall take-off distance. The same behavior as for the previously discussed optimization is found. The take-off distance is reduced by a reduction of the ground-roll distance, while an enlargement of the climb distance does not affect the overall take-off distance significantly. Here again, it has to be stated that the bulk data of this sub data set is not shown here, due to the parameter space shrinking during postprocessing. This includes again the optimum of the optimization 2, which is omitted during postprocessing.
By a comparison of the two discussed clustered regions, a distinct influence of the climb altitude is recognized. The increase of the climb altitude (sub data set 2) leads to a clustering of the samples that are located at shorter overall take-off distances, whereas the samples for the optimization with the lower climb altitude (sub data set 1) are clustered towards higher overall take-off distances.
Naturally, the higher the percentage of the ground-roll distance of the overall take-off distance is, the more the optimizations focus on this part of the take-off while a loss in the climb performance is tolerated.
Finally, the landing performance for these two sub data sets is studied. It is recognized that

both sub data sets achieve remarkable landing performance. Sub data set 2 reaches the best landing performance for the overall data base when the mechanism of the flap is accounted for. Note that this data sample does not exceed or reach the landing performance of the aerodynamic optimization without the consideration of the flap mechanism (sub data set 6). Within these optimizations, the reference take-off performance was significantly changed for the evaluation of the objective function and no boundary conditions were applied, which imply an improvement for both take-off and landing performances. By this, the gains in landing can trump the loss of the take-off performance. Overall the configuration shows improvements w.r.t. the objective function value. The system can adapt much better to the requirements needed to improve the landing performance. Therewith, more pronounced improvements can be achieved. Both aspects (negligence of the boundary conditions and thrust ratio equals 0.7) seem to be beneficial for the achievable gains for the landing configuration. After postprocessing it is shown, that when activating the boundary conditions and setting the thrust according to Table 8, the take-off performance is judged significantly less beneficial and hence, the configuration shows disadvantageous performance.

3.2.2 Sub Data Sets 3, 4 & 5

For the generation of the sub data sets 3 to 5 the parameter spaces, the climb height and the thrust setting were set according to the final values, refer to Table 9. For sub data sets 4 and 5 the mass of the slat and flap mechanism were fed into the flight mechanics tool. Additionally, these three sub data sets have the same objective function (equally weighted normalized distances, refer to Table 8) and the constraints were implemented to penalize the loss in take-off and/or landing performance compared to the baseline configuration.
Figure 33 shows the distribution of the data samples for sub data sets 3 to 5. The samples shown in this graph are again postprocessed according to Table 9. However, this means only that the influence of the mass of the mechanisms on the flight mechanics performance during take-off and landing was removed from sub data set 4 and 5 for the shown graph.
Globally, for the samples of the sub data sets all performance combinations are found. Increase or decrease of take-off performance in combination with increase or decrease of landing performance, always in comparison with the baseline configuration. The interesting part is naturally where at least one performance component is enhanced. However, the sub data sets show a huge number of clustered data samples in the domain where for both the take-off and the landing performance improvements are gained. Additionally, around the baseline configuration a clustered region of samples is located. In the following, we will concentrate on the third quadrant in which the take-off and landing performance are both enhanced. The distribution of samples there is depicted in Figure 34.
According to the distribution of the data samples in this figure, there is, as expected, not one individual sample that indicates optimality for both take-off and landing. Hence, the optimal design depends on the definition of the weights for take-off and landing for the objective function.
The clustered samples of sub data set 3 show the highest gains in the take-off but the lowest gains in the landing performance. Samples of sub data set 5 show opposite behavior. The samples of sub data set 4 exhibit medium improvements in take-off and landing compared to the bulk of the samples of sub data sets 3 and 5.
For sub data set 4 one main region of clustered samples is recognized. Additionally, some samples show almost constant landing performance while their take-off performance differs. Between these two regions a gap in the distribution of samples is recognized. The

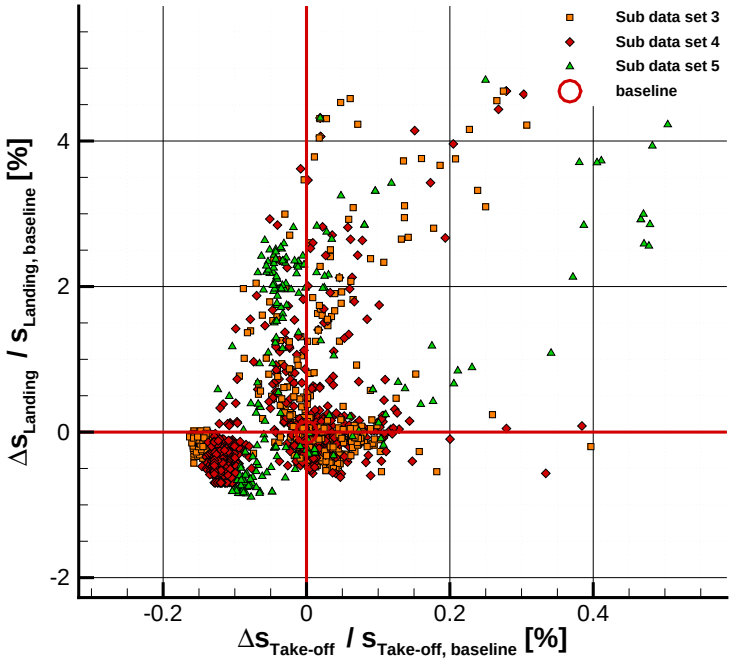

Figure 33: Distribution of samples of sub data sets 3, 4 and 5 for percental variation of the normalized landing distance versus the percental variation of the normalized take-off distance. Both MTOW and MLW are constant. Data samples are post-processed according to Table 9.

optimizer focuses on the "line-clustering" but is not able to reproduce more samples there. It seems that this domain is not robust, since small variations in the parameters lead to samples that are located in the other clustered domain. The samples on the Pareto front are recomputed completely, meaning CFD (with refined polar curves, higher accuracy) and flight mechanics analyses. The data showed the same behavior, hence we can conclude that the gap in the distribution of data samples is not based on a numerical artefact. Figure 34 shows the optima, which were detected during the corresponding optimizations.

3.2.3 Sub Data Set 6 - Aerodynamic Optimization

The last sub data set covers the two optimal samples that are found during the aerodynamic optimizations (optimization 6/7). Two independent optimizations were performed; one to achieve the optimal take-off setting and the other to find the optimal landing setting. During these optimizations the setting of the flap is defined according to the aerodynamic parameterization, i.e. dz, O/L and deflection angle define the setting, refer to Subsection 2.5.2. The parameterization of the slat still follows the kinematic based approach. This approach neglects the restrictions for the flap setting that are originated in the kinematical relationship of the trailing edge mechanism. In the following the optimal settings for take-off and landing are seen as one sample (Design (aero opt.)).

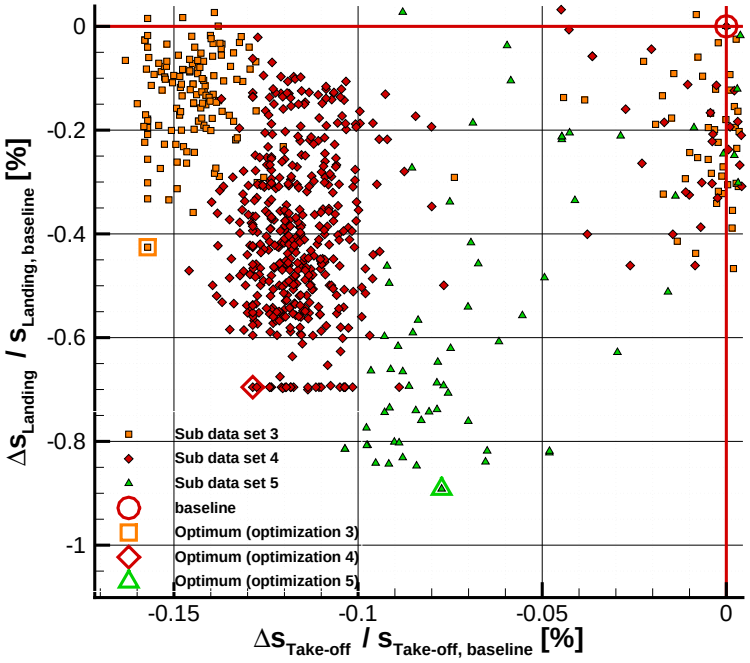

Figure 34: Distribution of samples of sub data sets 3, 4 and 5 in the third quadrant for percental variation of the normalized landing distance versus the percental variation of the normalized take-off distance. Both MTOW and MLW are constant. Data samples are postprocessed according to Table 9.

3.3 Global Overview of Data

The overall distribution of the samples of sub data sets 1 to 5 is covered in Figure 35. These data samples are the ones presented in the previous section, i.e. the samples are postprocessed according to the conditions presented in Table 9. Additionally, the optimal samples of the aerodynamic optimizations (sub data set 6) are indicated. This figure shows the normalized take-off distance variation versus the normalized landing distance variation. The distance variations are normalized with the properties of the baseline configuration. According to this figure, the improvements achieved for take-off are small in comparison to the achievements gained for landing. Overall, the highest achievements for both take-off and landing are achieved for the aerodynamic sub data set. For these configurations the take-off distance is reduced by -0.25% and the landing distance by -1.37%. When taking the mechanism of the flap into account the gains for both take-off and landing are smaller. The overall landing distance can be reduced by roughly -1.22% at minimum, while for the overall take-off performance the maximum reduction is -0.16%. When aiming at a design which enhances both take-off and landing, the highest reduction of the landing distance is approximately -0.89% and the reduction for take-off is again -0.16%.
The higher gains of the aerodynamic sub data set compared to sub data sets 1 to 5 are related to the parameterization of the high-lift system. The aerodynamic parameterization has a higher flexibility to position the flap, whereas the parameterization related to the kinematics has restrictions that originate from the type and geometry of the mechanism of the flap. Hence, it is plausible that the aerodynamic data (sub data set 6) can achieve higher

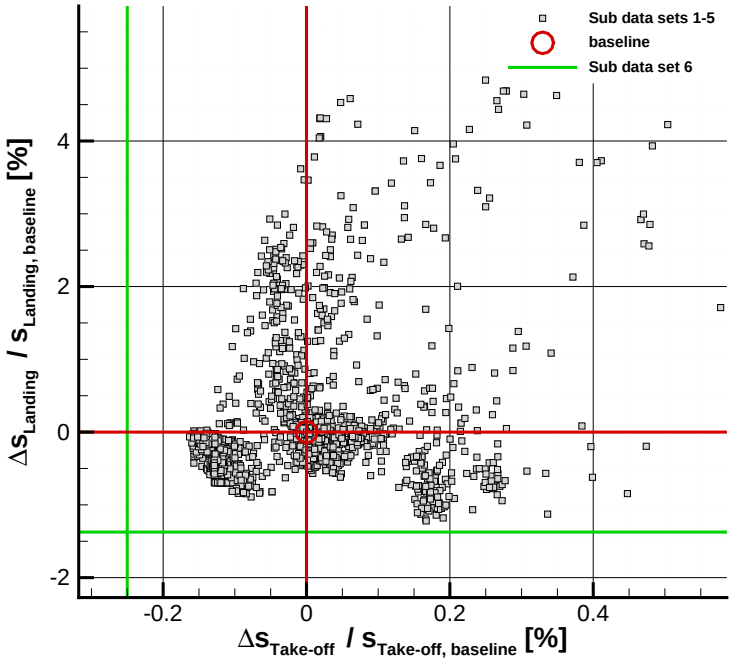

Figure 35: Distribution of samples of overall data base for percentual variation of the normalized landing distance versus the percentual variation of the normalized take-off distance. Both MTOW and MLW are constant. Data samples are postprocessed according to Table 9.

performance improvements than what is found for the sub data sets 1 to 5 which cover the restrictions of the flap mechanism. Detailed explanations on why the aerodynamically optimized configuration is not reached with a kinematic based approach are given in Section 3.4.

In the following, we concentrate on the data samples of the third quadrant. These samples reduce both the take-off and landing distance. Figure 36 depicts the third quadrant and additionally highlights samples (Design01 to Design04, baseline and Design (aero opt.)). These samples are investigated in the following sections from the different perspectives of the involved disciplines in the design process. Note that Design02 is the optimum of optimization 3, Design03 of optimization 4 and Design04 of optimization 5. Figure 36 shows also the Pareto front of the data base. The shown blue iso-lines are for percentual reduction of the overall objective function. The objective function that is applied here reads:

$$F(\vec{x}) = \frac{1}{2} \cdot \left(\frac{s_{\text{Landing}}}{s_{\text{Landing, baseline}}} + \frac{s_{\text{Take-off}}}{s_{\text{Take-off, baseline}}} \right). \tag{3.1}$$

It has to be pointed out that the algorithm used within this work is not designated to evaluate the Pareto front of the optimization problem. The Subplex algorithm is an optimization algorithm for single objective unconstrained optimization problems. Within this work the optimizer "sees" only a merged scalar value as objective function. Hence, the shown Pareto front may not be representative for the dual objective optimization problem, it represents only the Pareto front of the overall data base.

The shape of the Pareto front indicates that there is not one single individual sample that shows optimality both for take-off and landing. Which would be the case when it has the

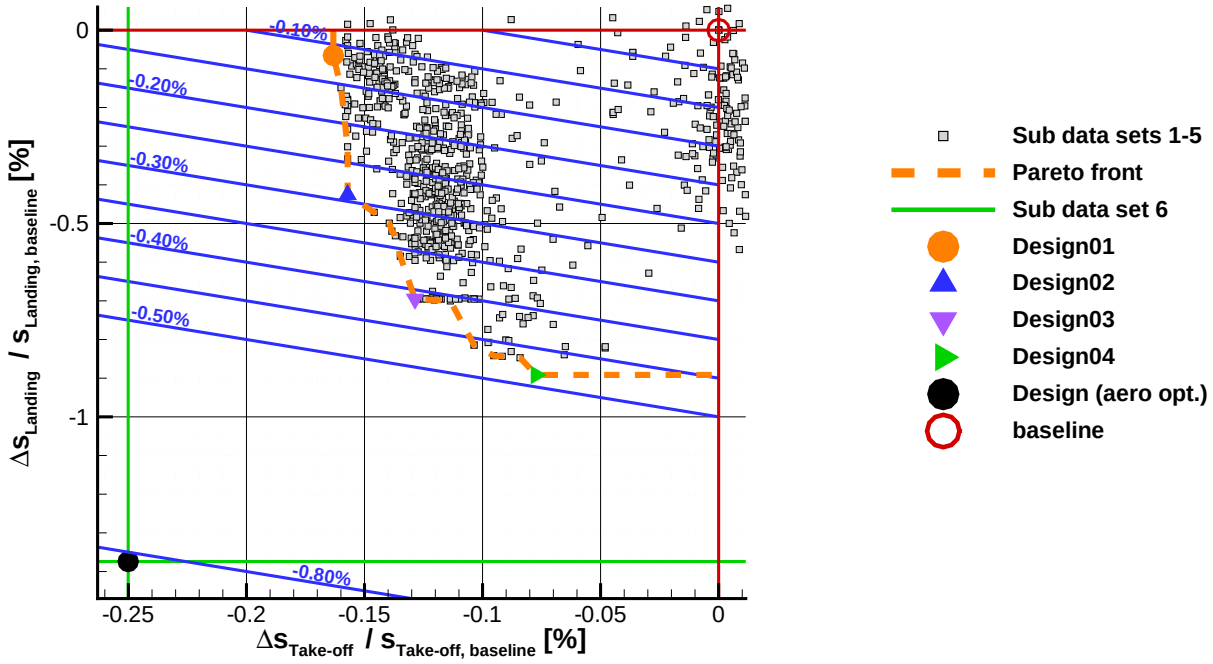

Figure 36: Distribution of samples of the overall data base in the third quadrant for percentual variation of the normalized landing distance versus the percentual variation of the normalized take-off distance. Both MTOW and MLW are constant. Data samples are postprocessed according to Table 9. Iso-lines illustrate the percentual improvement for the objective function, refer to Equation (3.1). The Pareto front of the sub data sets 1-5 is depicted additionally.

so-called "L-shaped" appearance (refer to [44, 48]) which has a tendency towards one single solution of the problem. Consequently, for this data base the optimal design changes when the weights for take-off and landing are varied.
When the mechanism for the flap is considered, Design01 on the Pareto front represents the highest improvements for take-off without degrading the landing performance. The optimal sample w.r.t. landing performance is not indicated in this figure as it is outside the domain shown in Figure 36.
According to the weighted objective function the optimal setting, under consideration of the trailing edge mechanism, is Design04. The improvement achieved for the objective function by this configuration is roughly -0.48%. This configuration shows also the highest improvements for the landing performance of the samples in the third quadrant. By the negligence of the mechanism of the trailing edge high-lift system the overall improvement for the objective function is higher and it reaches roughly -0.81%, see Design (aero. opt).

3.4 Trajectories and Slat, Flap Settings

In this section we investigate where the differences of the settings for slat and flap for the different designs are coming from. In the following, we have a look on whether or not the changes in the setting of the flap are related to changes in the geometry of the mechanism

or whether they are related to changes in the position on the trajectory of flap mechanism. Additionally, it is examined here, why the aerodynamic optimized setting is not found for the sub data sets which cover the mechanisms to deploy the flap.

3.4.1 Slat Settings

The trajectory path of the slat mechanism is constant for all investigated samples, since the radius and the hinge point of the constant-radius track are not changed within this work (refer to Subsection 2.5.1). The trajectory path of the slat from retracted position until maximum deployed position is shown in Figure 11. Figure 37 depicts a portion of the domain of the trajectory of the slat. Additionally, this plot shows the settings for the baseline, the settings of the designs on the Pareto front and the optimal setting of the aerodynamic optimization indicated by symbols. The settings that are related to take-off and landing are

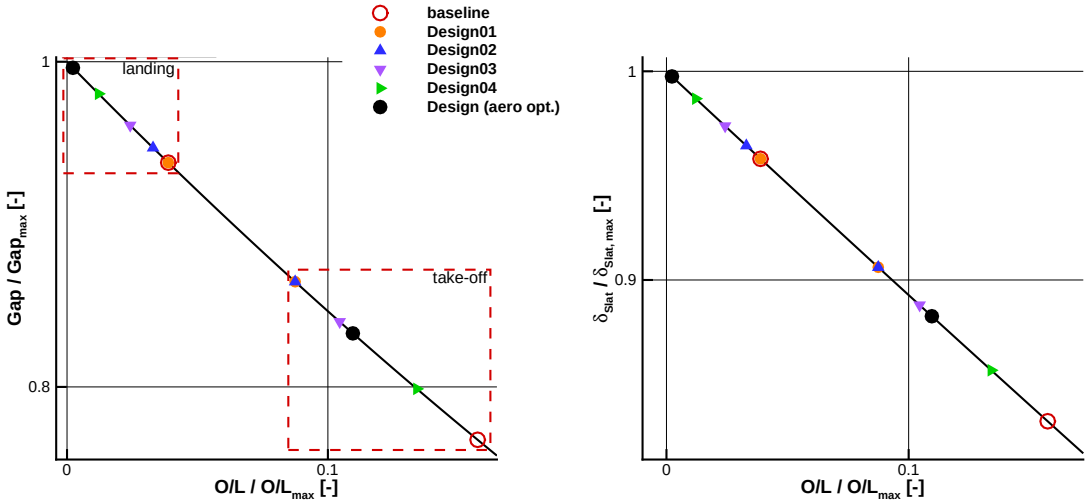

Figure 37: Detail of trajectory path of slat mechanism.
Left: gap versus overlap. Right: deflection angle of slat versus overlap.

boxed for illustration, respectively.
For landing, a gradual deployment of the slat is recognized starting from baseline design, Design01 via the samples on the Pareto front (Design02 - Design04) and ending with the highest deflection for the aerodynamic optimized setting (Design (aero opt.)).
At take-off, the slat deflection angle increases from the baseline configuration via the samples on the Pareto front (Design04 - Design01) but here the aerodynamic optimized setting does not follow this trend. The deflection angle of this setting is in the medium range of the different samples.
The increase of the deflection angle leads to an increase of the gap whereas the overlap decreases.
For take-off the spread of the settings for the slat device is more pronounced than for the landing setting. However, the variations in the overall take-off distance are much smaller in comparison to the variations in the overall landing distance. From this point of view, the slat deflection angle is insensitive towards the take-off distance.
The settings for the slat for Design01 and Design02 almost collapse for take-off. Minor variations are discernible for the take-off distance of these settings. Hence, they share not the same flap setting.

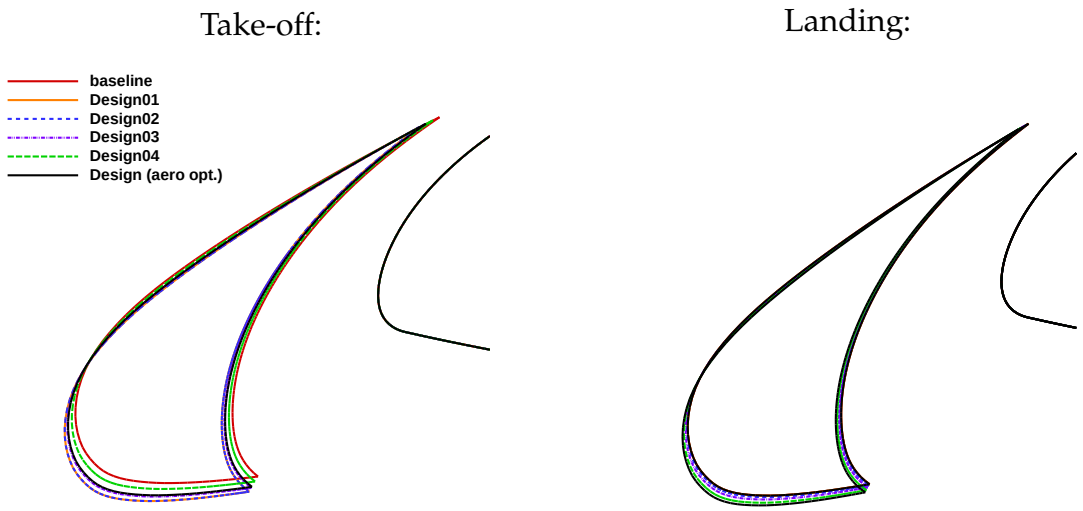

Figure 38: Setting of slat for take-off and landing.

For the sake of completeness the settings are shown in Figure 38 again but from an aerodynamics point of view. These plots give an impression how the settings change geometrically and the relations of the changes w.r.t. the size of the slat element are more obvious.
The variations of the deflection angle are stronger for take-off than for landing, as seen before. The variations in gap and overlap are recognizable, but they are small for take-off. For landing this impression is less evident, the changes in overlap and gap are almost not noticeable according to this figure.
As a conclusion one can say, that the process started with a good, robust baseline configuration. Since only small variations of the slat setting are achieved in this thesis. Further on, these small variations lead only to minor enhancements in the flight mechanics performance.

3.4.2 Trajectories of Flap Mechanisms

Figure 39 shows the gap and deflection angle of the flap versus the overlap, respectively.
At maximum overlap (O/L / O/L_{max}=1) the flap is retracted. In the first phase during deployment the deflection angle of the flap is decreased, i.e. the deflection angle gets slightly negative. At the beginning of this phase the spoiler of the configuration is minorly pushed upwards, since the value of the gap gets slightly negative. This behavior is typical for such a type of mechanism and it is not penalized during the deployment as a clash. The first part of the trajectory exhibits a Fowler motion[1] without significant increase of the deflection angle, which is beneficial for take-off according to literature, refer to Rudolph [5].
In the next phase, after the deflection angle reaches again its initial value, the flap is rotated and its deflection angle is increased. The steepness of the gradient for the deflection angle increases while the overlap decreases. This means, while increasing the deflection angle, the increase of Fowler motion slows down.
Naturally, the overall behavior of the curves is identical for the different configurations. We see that the curves for the deflection angle versus the overlap of the flap are very similar, only marginal variations of the curves are noticeable. For the gap versus the overlap varia-

[1] refer to Section 1.1 for explanation of the expression “Fowler motion”.

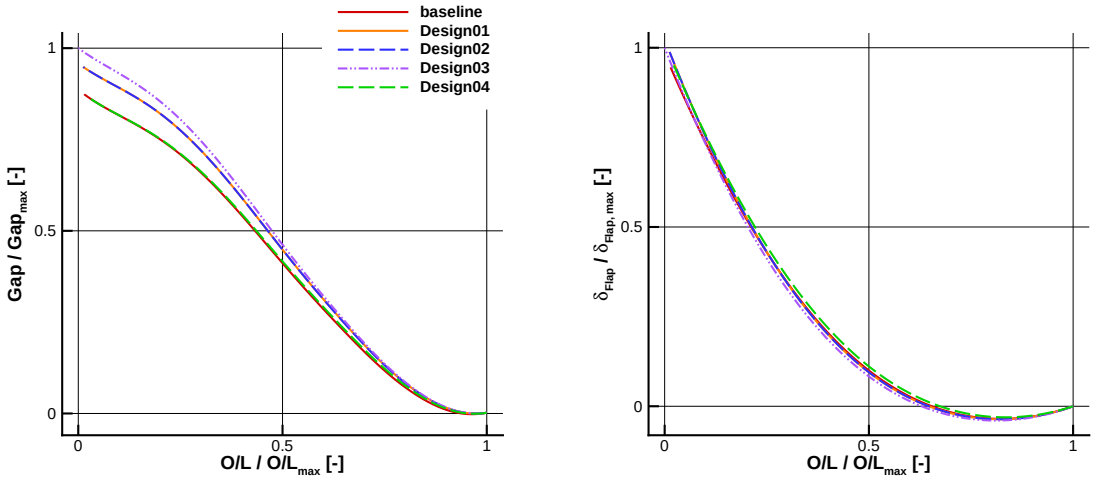

Figure 39: Trajectory of flap mechanism.
Left: gap versus overlap. Right: deflection angle of flap versus overlap.

tions are discernible. Close to the stowed setting of the flap (O/L / O/L$_{max}$ $\approx$ 1) the various curves are close together. Whereas, towards the maximum deployment of the flap the curves are spread more pronounced than what was seen before for the deflection angle versus the overlap.
It is apparent that the trajectories for the Design01 and Design02 almost collapse. Thus, the geometries of these two mechanisms only change insignificantly. For the baseline and the Design04 gap versus overlap almost collapse again. However, for these configurations small variations in the distribution of deflection angle versus overlap are recognized.
Concluding remarks: The choice of the type of flap mechanism defines directly the type of trajectory path distribution. By changing the positions of the supports, bearings and mounts the variations in the flap setting may increase towards smaller overlaps, respectively. Hence, for landing a wider flap setting variation can be achieved naturally in contrast to the variations that can be obtained for the take-off setting. Overall, the changes of the geometry of the mechanism lead to more pronounced changes in the trajectories for gap versus overlap than for deflection angle versus overlap.

3.4.3 Flap Settings

Figure 40 shows the domains of the trajectories of the various designs where the take-off and landing settings are located. These settings are indicated by symbols. The settings that are related to take-off and landing are boxed for illustration, respectively. The symbols that indicate the take-off settings are clustered at higher values for the overlap. The landing settings are reached when the flap is deflected almost at maximum.
In Subsection 2.5.3 two categories of parameters for the trailing edge mechanism were introduced. For the baseline and the Design01 the variations of the flap setting is mainly driven by the second category of parameters, which defines the position of the flap on the trajectory. The first category of parameters is almost identical, which defines the geometry of the mechanism and thus the trajectory path of the flap element.
A further interesting aspect here are the settings for take-off and landing for Design01 and Design02. The trajectories as well as the settings are almost identical for both designs, but

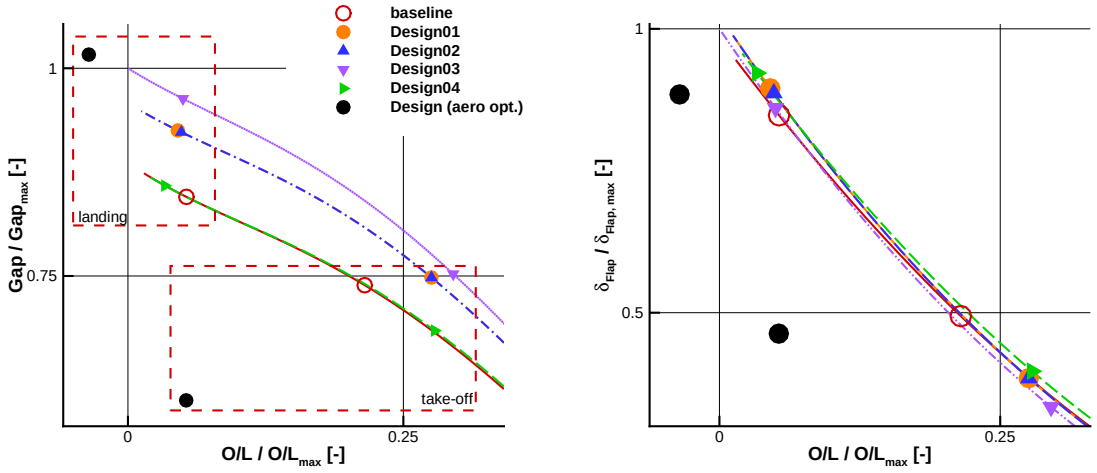

Figure 40: Detail of trajectory of flap mechanism.
Left: gap versus overlap. Right: deflection angle of flap versus overlap.

Design02 has a better landing performance. Therefore, the slat setting is taken into account which forms a further degree of freedom. These two designs differ in their deflection angle of the slat for landing, refer to subsection 3.4.1. For Design02 the deflection angle of the slat is increased. This leads to a higher maximum lift coefficient and consequently to an improved landing performance. For take-off the slat deflection angle is almost identical for both designs, as mentioned before. Consequently, the take-off performance differs insignificantly for the two designs, since the flap settings also collapse. This observation is as expected (according to Figure 36).
The aerodynamically optimized configuration shows a significant different position of the flap. During take-off, for this setting the overlap is drastically decreased in comparison to the other designs, shown in the figure, and also the gap is reduced. The deflection angle is similar to the baseline configuration. For landing the overlap is the most obvious value that is decreased for the aerodynamically optimized design in comparison to the mechanism-based designs. The gap for the Design (aero opt.) shows the highest value for all designs. The variations of the gap size for landing are mainly driven by the changes of the trajectories of the mechanism-based designs. These designs have a similar overlap. For take-off the design on the Pareto front share a similar overlap, but again the gap changes for the just mentioned reason. Since the distribution for deflection angle versus overlap has minor variations, the changes in the deflection angle for similar overlaps are naturally small.
Within this work, the mechanism-based optimizations are not able to reproduce the settings found to be optimal when the mechanism of the trailing edge device is neglected (Design (aero opt.)). The questions are, if the used type of mechanism is not able to reproduce these settings or if the optimization algorithm is not capable of finding the geometry of such a mechanism. From the shown figures it is expected that the distribution of the deflection angle versus the overlap of the flap may reproduce these optimal settings. However, for the distribution of the gap versus the overlap of the flap this case does not seem possible, since the gradient between the two optimal settings is very steep compared to the gradients of the shown trajectories in that domain.
To investigate this issue systematically, an optimization was set up with the objective to reproduce identically these aero optimal settings (take-off and landing) by a track-linkage mechanism. After many optimizations with substantial variations of the standard settings

of the algorithm, variation of the starting parameter setting and with the help of latin hypecube samplings in conjunction with a response surface method, it was not possible to find a mechanism which reproduces these settings equally. Even a reproduction with less accuracy is not possible.
Therewith, we can conclude that the difference between the optimal settings of the aerodynamic and the multidisciplinary approach is based on the choice of the mechanism and not on the algorithmic of the optimization. To say it in other words, the optimal settings of the aerodynamic approach are just not part of the design space of the parameterization for the multidisciplinary approach.
Now, as conclusion it can be said that two trends for the variation of the setting of the flap are recognized. For the deflection angle the trajectories for the different designs have a small spreading. Here, the variation of the deflection angle is mainly achieved by a variation of the position of the flap on the trajectory. Geometry changes in the mechanism therewith have insignificant influence on the trajectory of the deflection angle of the flap. For the gap the spread of the trajectories increases towards maximum flap deflection angle. Thus, the variation of the flap setting w.r.t. gap can result from changes in both categories of parameters. Both, the geometry change of the mechanism and the change of the position of the flap on the trajectory influence the gap value of the flap.

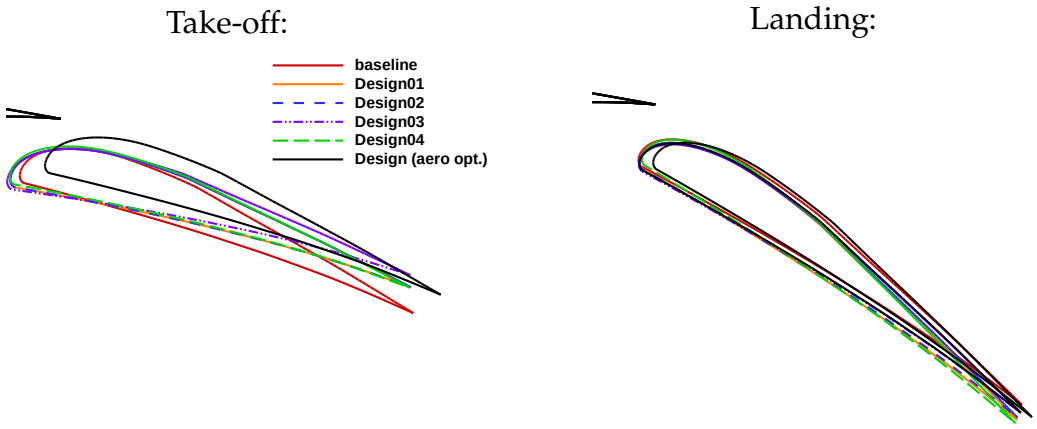

Figure 41: Setting of flap for take-off and landing.

Now, we take again the settings for the flap into consideration from an aerodynamics point of view. Figure 41 presents the settings for the flap for take-off and landing. Let's start to have a look on the **take-off** settings.
According to this figure, it is noticed that the designs on the Pareto front are from their setting rather similar. The setting of the baseline configuration shows a significant higher deflection angle. The aerodynamic optimized configuration has both a significant lower gap and overlap.
The overlap as well as the gap are almost identical for Design01 to Design03. For Design04 a reduction of the gap is recognized. Variations in the deflection angle for Design03 are more obvious in contrast to Design01, Design02 and Design04. The baseline configuration has a significant higher deflection angle and less overlap, the gap is rather similar to the designs on the Pareto front. The Design (aero opt.) shows a similar deflection angle like the baseline design, but has strongly reduced gap and overlap.
Now, we have a concluding look on the **landing** settings. Globally, all designs except from the Design (aero opt.) share similar values for gap and overlap. The deflection angle varies minor. The Design (aero opt.) has significantly less overlap and a slightly higher gap in

comparison to the other designs.
As a conclusion one can formulate, that from this thesis it is highly recommended to account for the flap mechanism during high-lift optimizations. Since it is shown, that it is not inevitably possible to reproduce multiple flap settings that are achieved by aerodynamic optimizations without accounting the flap mechanism. By the negligence of the flap mechanism the design process gets iterative or compromises of the settings have to be agreed on. Both aspects are less beneficial. When considering additionally the flap mechanism, the design process reveals only settings that can be implemented by the predefined flap mechanism and thus a more productive design process is achieved.

3.5 Aerodynamic Analysis of Data

Now, let's have a closer look on how the setting changes of the designs affect the aerodynamics for take-off and landing. The aerodynamic data presented in this section were calculated after the overall data base was established. The data were calculated according to the previously mentioned solver settings. Here, the robust (moderate) settings are used. Both the resolution of the angle of attack domain and the requirements for the accuracy of the aerodynamic coefficients for each angle of attack are increased. Towards maximum lift, the angle of attack increment is reduced naturally to cover the non-linear behavior of this region properly.

3.5.1 Take-Off Run

For the take-off run the Lilienthal polars of the baseline configuration, the designs on the Pareto front and the aerodynamically optimized configuration are shown in Figure 42. The aerodynamic coefficients shown in this figure are first the two-dimensional evaluated coefficients. Second, the lift coefficient (2.5D)[2] is shown versus the drag coefficient (quasi 3D)[2]. The quasi three-dimensional drag coefficient covers the lift-induced drag to cover that the variation of the lift coefficient influences also the drag coefficient. For the flight mechanics evaluation of the take-off and landing distance the lift (2.5D) and drag (quasi 3D) coefficients are considered. Furthermore in this figure, the aerodynamic coefficients for the climb phase are indicated by symbols.
The curves are almost collapsing as expected due to the small differences achieved in the overall take-off distance. The curves show more variety for the two-dimensional results than for the results in the line-of-flight plane (2.5D, quasi 3D). The main difference is the maximum lift coefficient, while in the domain below the maximum lift coefficient the various curves almost collapse. As expected, the influence of the lift-induced drag coefficient is significant, since the behavior of the curves is changed drastically. The direct dependency of the climb condition on the maximum lift coefficient[3] is obvious for the designs and therefore the coefficients for climb differ. An increase of the maximum lift coefficient leads directly to a raise of the lift coefficient for the climb condition. The glide-ratio[4] decreases while the angle of attack increases for the line-of-flight plane under consideration of the lift-induced drag. Here the glide-ratio is not optimized for each design, meaning the optimal glide-ratio for the given lift-to-drag curve is not detected, but the lift coefficient is always chosen based

[2] refer to Figure 14 and to Equations (2.27) to (2.29)
[3] refer to Table 3
[4] Note: The expressions glide-ratio and lift-to-drag ratio are used equivalently in this work.

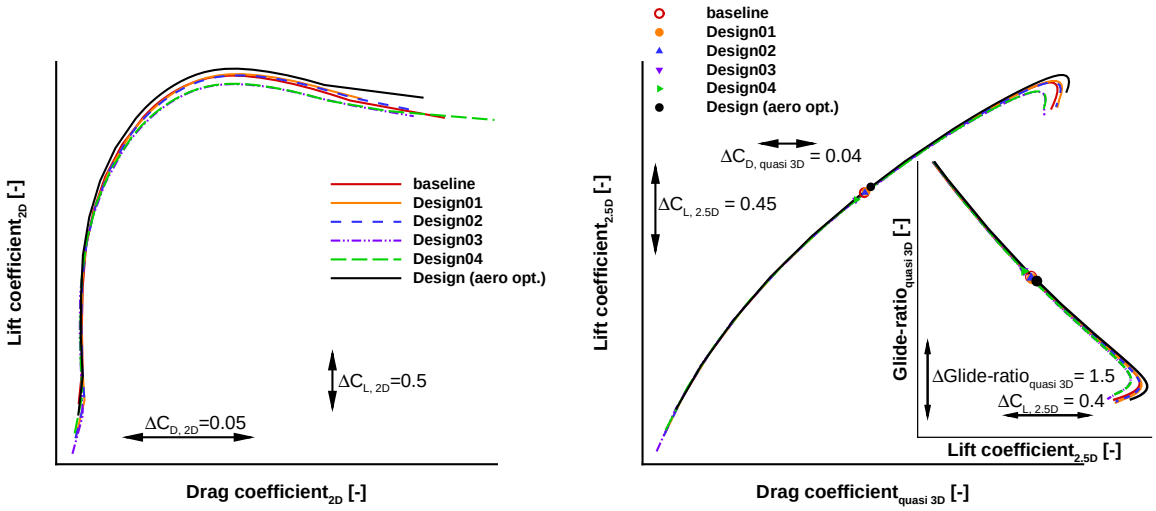

Figure 42: Left: lift (2D) versus drag coefficient (2D). Right: lift (2.5D) versus drag coefficient (quasi 3D), which covers the lift-induced drag. Right-small: Glide-ratio (quasi 3D) versus lift coefficient (2.5D). The glide-ratio is determined according to following relationship: Glide-ratio$_{\text{quasi 3D}} = C_{L,\text{2.5D}}/C_{D,\text{quasi 3D}}$. For both plots, the free-stream stalling condition for take-off is considered.

on the following relationship: $C_L = C_{\text{L,max,TO}}/1.13^2$. The glide-ratio for the various designs changes insignificantly. The variation of the glide-ratio for the climb segment in comparison to the baseline configuration is roughly -1% to +1.5%. The domain for the maximum lift variation is roughly -1.8% to +1.5% in comparison to the baseline configuration.
The optimal configuration from the aerodynamic optimization exhibits the greatest negative variation in the glide-ratio for take-off but reaches the highest improvement in the maximum lift coefficient. The optimal configuration under the consideration of the flap mechanism w.r.t. take-off (Design01) shows also this trend. However, the improvement in the maximum lift coefficient is less pronounced and hence the lift-to-drag ratio for climb is minorly reduced.
Concluding remarks: Overall, the non-dominated samples that form the Pareto front imply that there are two-different strategies to decrease the take-off distance. Either the maximum lift coefficient is increased which leads to a reduction of the glide-ratio during climb, or vice versa. I.e. the maximum lift coefficient and the glide-ratio show a conflicting manner. The aerodynamic optimized design follows the strategy to enhance maximum lift and it accepts a minor reduction in the glide-ratio. For the design of a new aircraft both quantities are important, the maximum lift coefficient and the glide-ratio during climb. As an example, for the design of a new aircraft with a desired short take-off field length[5] the enhancement of the maximum lift coefficient is focused on. But still, an acceptable glide-ratio during climb according to the federal aviation regulations at minimum has to be made possible.
As stated at the beginning of this section, the aerodynamic data shown here are established after data generation was accomplished. A higher resolution in the angle of attack domain and a higher accuracy of each individual angle of attack computation were accounted. It is shown that the trends found in the optimization are well reproduced, i.e. the accomplished steps in the optimizations to decrease the turn-around cycles for each design show feasible results for the baseline and the designs on the Pareto front. Therewith, we can conclude that the applied computational scheme is properly defined to reproduce the trends of the

[5]take-off field length is the distance over ground from stand still till the obstacle height (35ft) is reached

optimization problem for the shown examples.

3.5.2 Landing Run

Figure 43 depicts the lift coefficient over the angle of attack for a wide angle of attack domain.

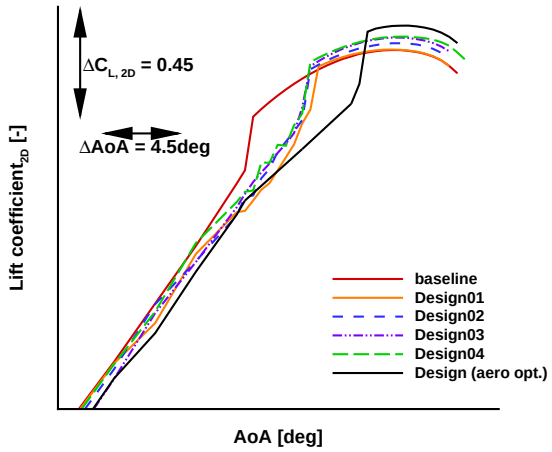

Figure 43: Lift coefficient versus angle of attack (AoA) for landing setting.

For lower angles of attack in this figure the various designs exhibit roughly a linear behavior. Then a sudden increase in the lift coefficient is recognized. Thereafter, a non-linear relationship between lift coefficient and angle of attack is noticed. The lift coefficient reaches its maximum value and afterwards it decreases.
For the various designs the maximum lift coefficient increases from the baseline sample, via Design01, Design02, Design03 and Design04 and it achieves its maximum value for the aerodynamic optimized configuration (Design (aero opt.)). It is recognized that the sudden increase of the lift coefficient takes place at a significant lower angle of attack for the baseline configuration compared to the designs on the Pareto front. The baseline design has a higher angle of attack margin for the domain of sudden lift-increase and maximum lift. The angle of attack for maximum lift coefficient does not vary strongly for all shown designs. The angle of attack domain (angle of attack at sudden increase of lift coefficient until angle of attack at maximum lift coefficient) is drastically smaller for the designs on the Pareto front compared to the baseline configuration. This is noticed even more distinctly for the aerodynamically optimized configuration. The designs on the Pareto front differ in their maximum lift coefficient slightly and their overall behavior is similar. In the angle of attack domain, for angles smaller than the angle at the sudden increase of the lift coefficient, the slope of the lift coefficient curves differ only minor for the different designs.
Now, the reason for the sudden increase of the lift coefficient is studied, therefore we take Figure 44 into account. This figure shows the pressure coefficient distribution for the rear part of the main element and the flap element for two angles of attack (AoA_1, AoA_2). Additionally, the lift coefficient versus the angle of attack for the baseline configuration is shown. The angles of attack are indicated in the lift coefficient versus angle of attack plot. They refer to the angle of attack below and above the sudden increase of the lift coefficient. Additionally, the flow fields around the flap element are depicted for the two angles of attack. The

data belong to the baseline configuration, which is shown here exemplarily.

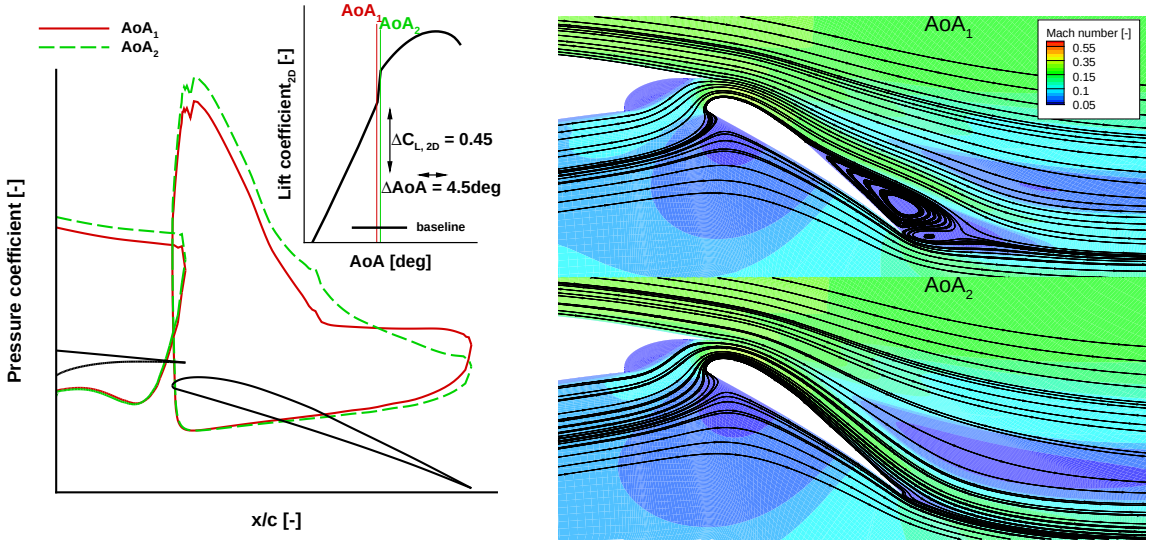

Figure 44: Left: pressure coefficient distribution for landing setting for baseline configuration. Right: detail of flow field for baseline configuration in the vicinity of the flap in landing configuration. Mach number is indicated by the contour.

According to this figure, we can recognize that the main difference between the two shown flow fields is whether or not there is a separation on the rear part of the flap element. The flow field snapshots clearly show that the **separation on the flap** is absent for the higher angle of attack (AoA_2). The stream lines follow the contour of the flap element for the higher angle of attack. For the lower angle of attack (AoA_1) a distinct separation bubble is noticed from approximately half of the flap chord till the trailing edge for the suction side of the flap element. The trailing edge stagnation point is shifted from the trailing edge into the flow field.
Let's have a look on the pressure coefficient distribution for both angles of attack. A possible separation at the lower angle of attack is recognized by a wide domain of constant pressure coefficient on the suction side of the flap close to the trailing edge. Additionally, the pressure coefficient is negative at the trailing edge, which indicates a separation and a shift of the trailing edge stagnation point into the flow field. According to the snapshots of the flow field it is already shown that this constant pressure domain is related to a separation. For the higher angle of attack the pressure coefficient distribution is distributed in a "healthy" manner, i.e. no domain of constant pressure and consequently no separation is noticed.
The pressure coefficient distributions show oscillations in the domain of the suction peak and roughly half of the chord on the suction side for the flap. These oscillations are originated in surface imperfections, i.e. the curvature distribution is not smooth. Aftwards, the position of the oscillations on the flap is at the trailing edge of the spoiler for the retracted flap. At the junction of the cove shape and the upper surface of the flap the curvature distribution is naturally not smooth. At the forward position of the oscillations an unsmooth curvature distribution is also found. These can lead to the recognized oscillations in the pressure coefficient distribution and furthermore the aftward position might trigger the separation.
We will now have a closer look at the pressure coefficient distributions. On the flap, we notice the increased suction peak for the attached flow on the flap for AoA_2 in comparison to AoA_1. Furthermore, the pressure ratio between suction peak and trailing edge pressure is higher. On the main element the pressure level on the suction side is decreased and also the

trailing edge pressure is reduced. Therewith, the flow does not expand that intensely and the flow velocity in the vicinity of the trailing edge of the main element is increased. The origin of lower pressure level on the main element is the increased circulation and dumping effect[6] of the flap. The slat effect[6] (main element towards flap) controls the suction peak of the flap. Therewith, the suction peak is lowered and the pressure ratio between leading and trailing edge is reduced. Hence, the tendency of a separated flap is decreased with increased lift generation on the main element. Regarding the pressure coefficient of the lower angle of attack, it is noticeable that the pressure ratio is even smaller. First, the pressure at the trailing edge of the flap is decreased, the flow expands to free stream conditions not at the trailing edge, but in the flow field aft of the flap (shifting of the rear stagnation point). Second, the suction peak is reduced. This is originated by the fact that the shape of the flap is artificially thickened and enlarged by the separation. The flow does not need to accelerate that strong around the leading edge of the flap to be able to follow the surface, that is artificially thickened. The camber of the flap is lowered artificially by the separation. Furthermore, as said before, the stagnation point aftwards is shifted from the trailing edge of the flap into the flowfield. Hence, the trailing edge pressure does not expand to the farfield static pressure. With these effects the circulation of the flap is decreased and consequently the flow velocity is decreased in the vicinity of the trailing edge of the main element.
For the lower angle of attack, the main element is not "strong" enough to reduce the suction peak of the flap sufficiently to avoid the separation. This also affects the main element for which then on the suction side the pressure level is increased. This means that on the main element and on the flap the circulation is reduced unfavorably.

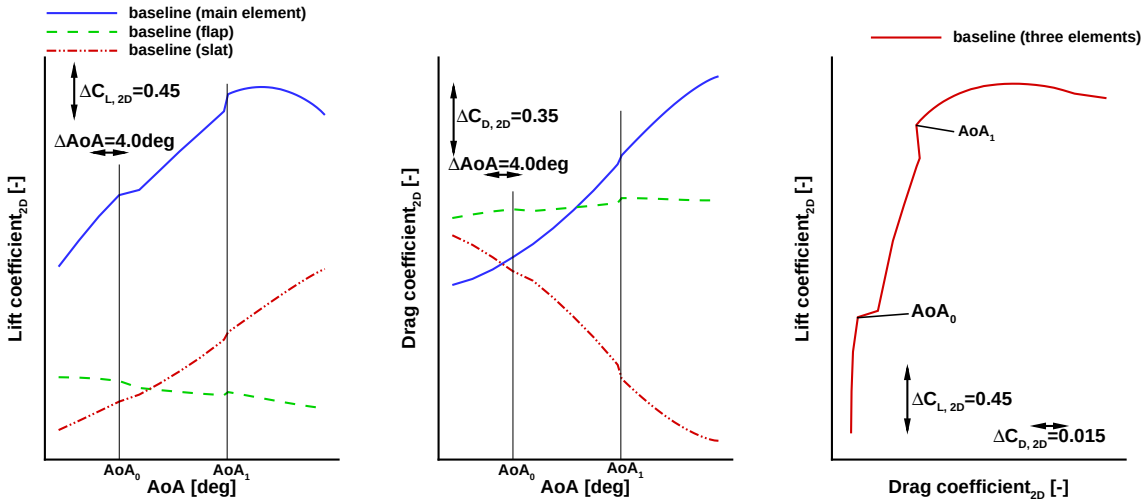

Figure 45: Aerodynamic coefficients (2D) for slat and flap (left, center) and for whole configuration (right) at landing for the baseline configuration. For the definition of AoA_2 refer also to Figure 44.

The lift and drag coefficients for the three elements versus the angle of attack and the lift versus drag coefficient for the overall configuration are shown in Figure 45. The lift coefficient for the slat increases over the whole angle of attack domain. The flap shows an overall slight reduction of the lift coefficient and additionally in the domain, where a separation is detected on the flap, the lift coefficient is slightly reduced. The main element produces naturally the main part of the lift and a non-linear region is discernible around the angle of

[6] refer to Smith [13]

attack domain of the maximum lift coefficient. For this element the angle of attack domain, in which a separation on the flap exists, is recognized due to a sudden reduction of the lift coefficient ($AoA_0 < AoA < AoA_2$). For the angle of attack when the flap separation is just vanished, the lift coefficient for the main element and slat element increases rapidly at the higher angle of attack (AoA_2). This figure clearly shows again that the circulation of the main element and of the flap is lower, while a separation on the flap is recognized. Furthermore, it is noticed that the separation also affects the slat element. For this element a sudden increase of the lift coefficient is also discernible when the separation on the flap vanishes (at AoA_2).
The drag coefficient that is plotted in the figure for the different elements is the drag coefficient obtained from the two-dimensional computations. It consists of pressure and friction drag. For the slat, the drag coefficient decreases while the angle of attack increases. The drag coefficient gets negative at a small angle of attack and it produces thrust for this element. For the main element the drag coefficient increases with the angle of attack. For the flap the drag coefficient is roughly constant over the entire angle of attack domain. For all elements a sudden change in the drag coefficient is recognized when the separation vanishes (at AoA_2). For the slat, the drag coefficient decreases, whereas for the main element and the flap the drag coefficient increases. The drag coefficient rise for the main element and the flap is originated mainly in the increase of the pressure drag. The friction drag of the flap is naturally decreased when the separation vanishes but the sum of the drag components increases.
The polar plot for the whole airfoil is additionally shown. This plot shows that at the point where the separation vanishes, it mainly leads to a jump in the lift coefficient. The drag coefficient decreases only slightly.
Concluding remarks: Overall, the results show that the final configurations on the Pareto front on one side and the optimized configuration from the aerodynamic optimization on the other side show a strong separation on the flap which vanishes only in the close vicinity of the maximum lift coefficient. This behavior is more pronounced for the aerodynamic optimized configuration than for the samples on the Pareto front. For the baseline configuration the separation is suppressed at lower angles of attack with a drastic higher margin towards the maximum lift coefficient.
As stated in Subsection 3.5.1, the settings for the determination of maximum lift coefficient are sufficient during data generation. Since, even with both a higher resolution in angle of attack and with a higher accuracy for the flow computations the results found during data generation are reproduced.

3.6 Flight Mechanical Analysis of Data

After the aerodynamic behavior of the various designs on the Pareto front, the baseline design and the aerodynamic optimized design are analyzed, we now have a look on how these designs behave from a flight mechanics point of view. Additionally, all designs of the various sub data sets are considered for this analysis. We start with the analysis of the take-off run and afterwards, the landing run is discussed.

3.6.1 Take-Off Run

Generally, *"the aerodynamic optimization of the take-off configuration is aimed at finding the best compromise between lift capability and L/D efficiency to satisfy the requirements for both take-off*

field length and the climb rate."[7] With this statement in mind, let's analyze and discuss the data base.

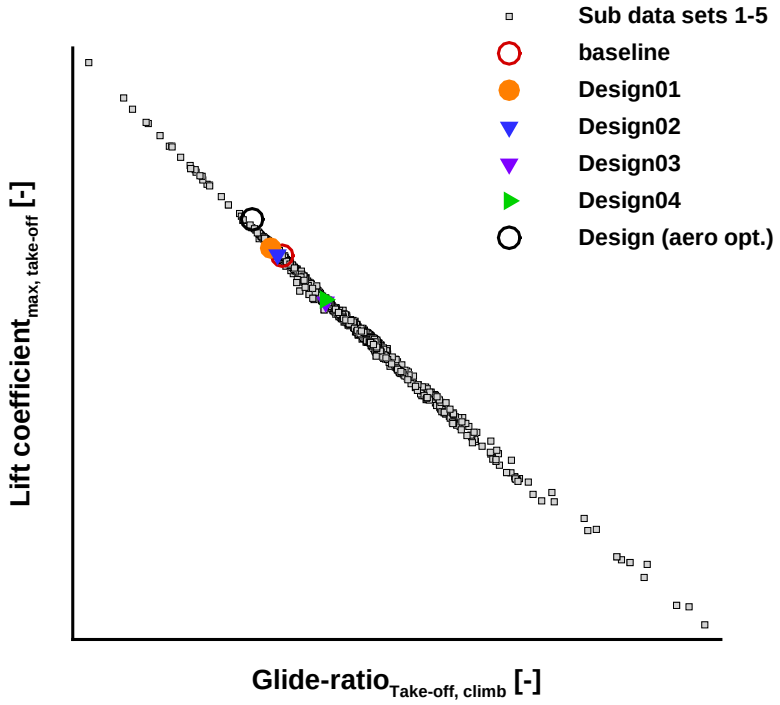

Figure 46: Maximum lift coefficient for take-off versus glide-ratio for climb segment.

Figure 46 shows the behavior of the maximum lift coefficient versus the lift-to-drag ratio[8] for the climb segment for all sub data sets. Additionally, the samples on the Pareto front, the baseline, and the aerodynamic optimized configurations are depicted by symbols. It is found that the data samples show a conflicting manner of the maximum lift coefficient and the lift-to-drag ratio for the climb segment, which was already indicated by the citation of Flaig at the beginning of this section. Globally spoken, samples with increased maximum lift coefficient tend to show less beneficial glide-ratio for the climb segment and vice versa. The data samples are distributed almost on a straight line. The baseline configuration, the samples on the Pareto front, and the aerodynamic optimized configuration are roughly located in the moderate region. This means that the samples neither focus on maximization of the maximum lift coefficient nor on the maximum possible glide-ratio for the climb segment. The two quantities are moderately balanced. It is noticeable that the aerodynamic optimized configuration is located slightly off the straight line. The lift-to-drag ratio is enhanced compared to the samples with similar maximum lift coefficient that consider the mechanism for the flap. This observation indicates again that the mechanism for the flap restricts the design space of the flap setting and thus its aerodynamic performance.
The overall take-off distance covers the ground-roll, the transition phase and the climb phase. The two dominating distances for take-off are ground-roll and climb, which cover together roughly 94% of the total take-off distance for a climb altitude of h=1500ft and evaluated for the baseline configuration. Refer to Figure 28 for illustration of the segments during the take-off run. In the following, we concentrate on these two distances. Figure 47

[7] Flaig [12] page 31-3
[8] Note: The expressions glide-ratio and lift-to-drag ratio are used equivalently in this work.

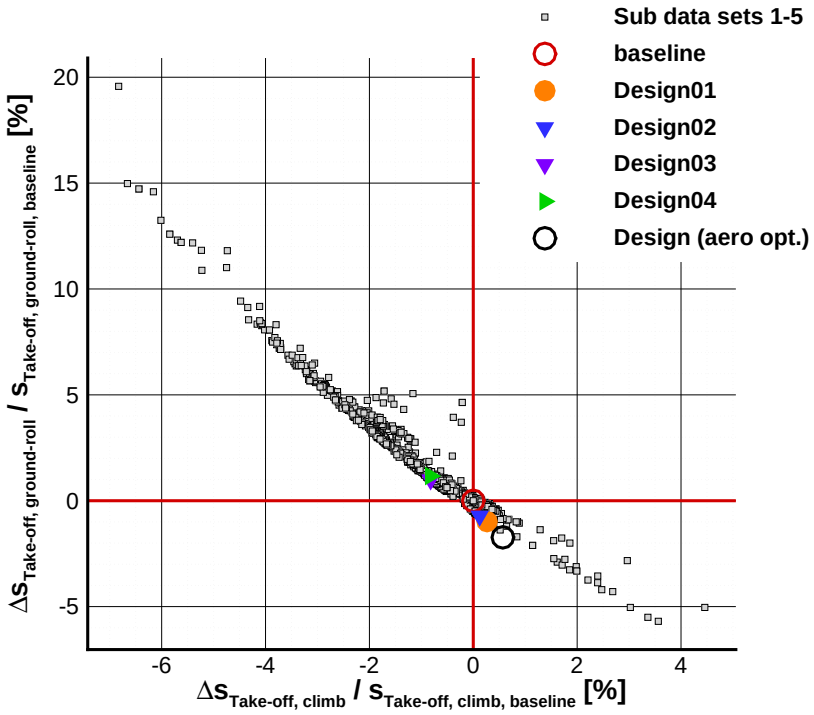

Figure 47: Percentual variation of distance for ground-roll versus percentual variation of distance for the climb segment for a climb altitude of 1500ft.

shows the ground-roll distance versus the distance for the climb segment. As expected, a conflict between the two quantities is noticed, i.e. the two quantities show anti correlation. The data samples are distributed roughly along a slight non-linear curve. The curve separates sharply the domain towards the origin. In the other direction, some outliers exhibit for a given climb distance an increased ground-roll distance and vice versa. It is recognized that the aerodynamic optimized configuration is located slightly out of the bulk data towards the origin.

Based on the flight mechanics relationships presented in Subsection 2.9.1 (refer to Equations (2.40), (2.49)), the ground-roll distance depends mainly on the maximum lift coefficient and the climb segment depends on the glide-ratio. This behavior is reflected by the data samples depicted in Figures 48, 49. These figures clearly shows the anti correlation of maximum lift and ground-roll distance and for climb distance and glide-ratio.

Hence, for take-off the maximum lift coefficient and the glide-ratio need to be balanced, according to the impact of ground-roll, transition and climb, to achieve a proper configuration. This reflects well the citation of Flaig[9] at the beginning of this section.

Figures 50, 51 depict the relationship between the overall take-off distance, the distance for ground-roll and for the climb segment respectively. The minimum overall take-off distance is achieved by the Design01 under consideration of the mechanism for the flap. When the mechanism is neglected, possible reductions in the overall take-off distance are higher, which is seen for Design (aero opt.). Generally, for each overall take-off distance there are two extreme possible designs: one design with a shorter distance for climb but with an increased distance for ground-roll and vice versa for the second design. When comparing the two plots it is discernible that the data samples are mirrored. Data samples that have a

[9]Flaig [12] page 31-3

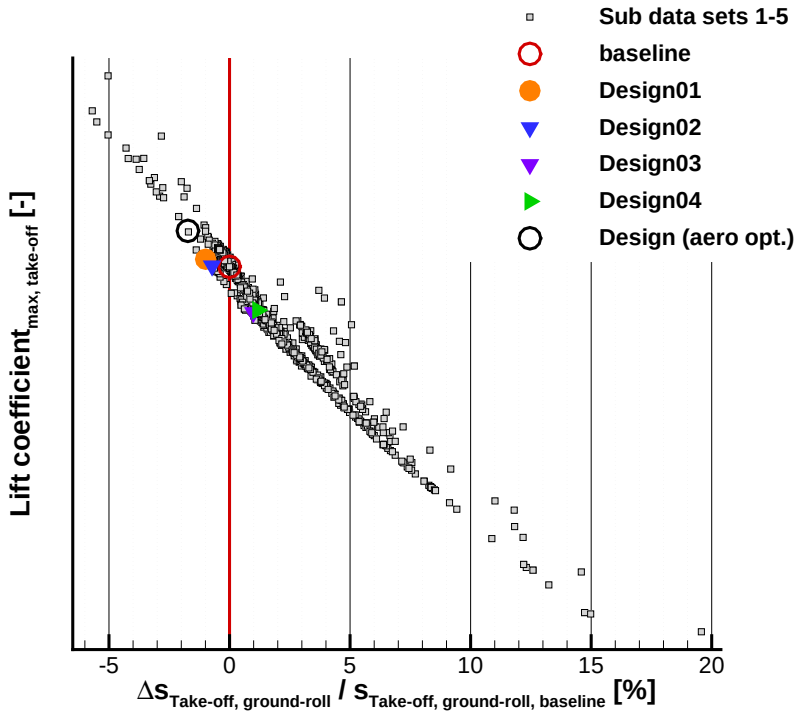

Figure 48: Maximum lift coefficient for take-off versus percentual variation of distance for ground-roll.

long ground-roll distance show a short climb distance. The optimal design for the equally weighted take-off and landing distances under consideration of the mechanism for the flap (Design04) do not exhibit the shortest take-off distance. Optimality is derived under the consideration of take-off and landing, that is why the optimal configuration (Design04) for the objective with equally weighted normalized distances does not necessarily exhibit for both dimensions the lowest distance. But from the dual-distances view this design shows the highest improvements.

Concluding remarks: We have seen that the maximum lift coefficient and the glide-ratio are in conflict, therefore it is important to decide which quantity for take-off is more important. If the climb distance is the important one, then a focus is laid on the maximization of the glide-ratio during climb. If a short take-off field length[10] is needed then the focus is laid on a higher maximum lift coefficient.

For the design of a new aircraft both quantities are relevant. First of all, a high climb performance is desired and also the operated airports need to be considered, whether take-off and landing are possible on the available runways. Taking into account the received overall data base, following conclusions can be summarized. To improve the take-off performance the trend is to increase the maximum lift coefficient slightly and to accept a reduction of the glide-ratio for the climb phase. This tendency is recognized for the optimal configuration for take-off under the consideration of the flap mechanism (Design01, Design02). Design (aero. opt.) also follows this tendency. But there is also a second option to increase the take-off performance. Instead of an increase of the maximum lift, this option focuses on the enhancement of the glide-ratio for the climb phase. Therewith the maximum lift coefficient is consequently reduced (refer to Design03 and Design04). According to this data

[10] take-off field length is the distance over ground from stand still till the obstacle height (35ft) is reached

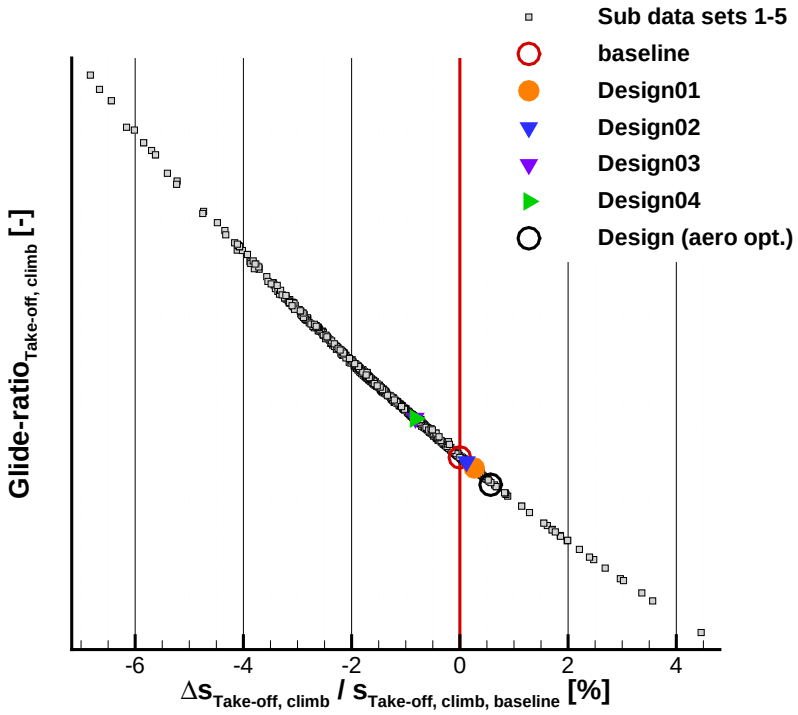

Figure 49: Glide-ratio for climb segment versus percentual variation of distance for the climb segment for a climb altitude of 1500ft.

base, the more effective option seems to be the first one. This is deduced since this option is taken by the aerodynamic optimized configuration and also by the configuration on the Pareto front (Design01) that achieves the best take-off performance for all studied samples under consideration of the flap mechanism.

3.6.2 Take-Off Run - Variation of Climb Altitude

This subsection investigates how the climb altitude (H_{Climb})[11] influences the final, optimal configuration w.r.t. the equally weighted objective function (Equation (3.1)). Hence the optimality considers again the equally weighted normalized take-off and normalized landing distances. For this investigation no further data were generated. Only the previously shown overall data base (sub data sets 1-5) is postprocessed again with different climb altitudes. It is important to point out that the bulk of the data samples are generated within optimizations aiming at improving take-off with 1500ft climb altitude. Hence the data distribution for the alternative two altitudes may not be fully representative.
Three different climb altitudes are considered:

1. 400ft is the altitude when it is first possible to change and to retract the high-lift system, respectively.[12]

[11] refer to Figure 28 for illustration of the climb altitude H_{Climb}

[12] CFR, titel 14, part 25, subpart B, 25.111 (c)(4) [73]: *"The airplane configuration may not be changed, except for gear retraction and automatic propeller feathering, and no change in power or thrust that requires action by the pilot may be made until the airplane is 400 feet above the takeoff surface;"*

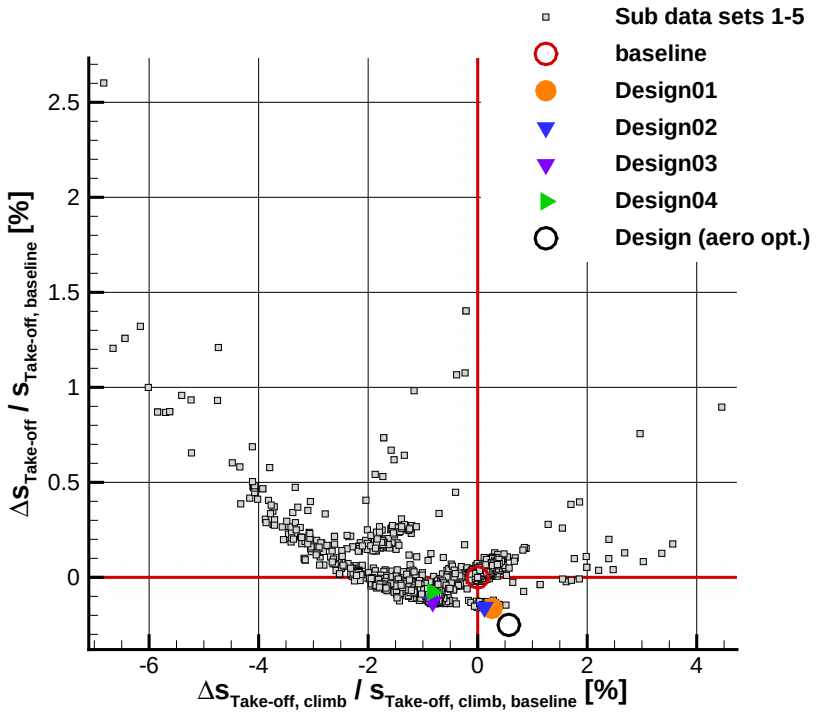

Figure 50: Percentual variation of overall distance for take-off versus percentual variation of distance for the climb segment for a climb altitude of 1500ft.

2. It is foreseen that the take-off path extends at least to a point at which the aircraft is 1500ft above the take-off surface.[13]

3. The take-off path can be further extended. It ends when the transition from take-off to en route configuration is completed and the final take-off speed is reached[13]. Here we consider 3000ft to further increase the influence of the climb segment.

Figure 52 shows again the relationship of maximum lift coefficient and glide-ratio during the climb phase for take-off. In contrast to Figure 46, the optimal settings for the different climb altitudes 400ft, 1500ft and 3000ft are indicated by symbols.
This figure shows clearly that the balance between maximum lift coefficient and glide-ratio changes significantly for the optimal sample by the variation of the climb altitude. For the lowest climb altitude (400ft) the optimal configuration is characterized by a high maximum lift coefficient and a low glide-ratio (Design05). For the highest climb altitude (3000ft) the optimal design shows an opposite behavior (Design06). The extrema of the shown plots are not taken as optimal designs, even if the climb altitude is further increased/decreased. This is due to the fact that still the second dimension of the optimization problem is considered, namely, landing distance. Figures 53, 54 show the take-off distance versus the landing distance, both normalized, for 400ft and 3000ft take-off height. These figures show again that there is not one single design showing optimality for both take-off and landing. Possible performance enhancements are more pronounced for a climb altitude of 400ft than

[13]CFR, titel 14, part 25, subpart B, 25.111 (a) [73]:*"The takeoff path extends from a standing start to a point in the takeoff at which the airplane is 1,500 feet above the takeoff surface, or at which the transition from the takeoff to the en route configuration is completed and VFTO is reached, whichever point is higher."* VFTO stands for final take-off speed.

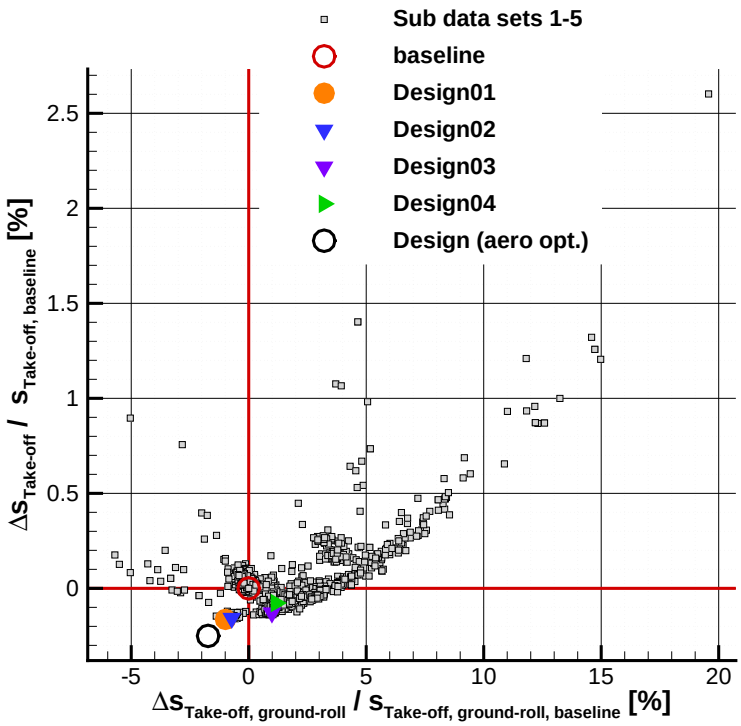

Figure 51: Percentual variation of overall distance for take-off versus percentual variation of distance for ground-roll for the climb segment for a climb altitude of 1500ft.

for 3000ft. It is evident that the landing performance of the samples is independent of the take-off climb altitude. The highlighted samples achieve equivalent landing enhancements but the take-off performance changes.
Table 10 shows the percentual part of the individual distances that form the overall take-off distance. This table apparently demonstrates that the climb altitude significantly changes the impact of the ground-roll distance and the distance for the climb segment on the overall take-off distance. The increase of the climb altitude leads naturally to a more dominant distance of the climb segment. Consequently, the influence of the ground-roll distance and the distance for the transition phase is reduced. For 400ft and 1500ft, the impact of ground-roll and climb segment is roughly reversed.
A further aspect is the reduction of the impact of the transition phase while the climb altitude is increased. This is simply explained by the direct correlation of the distance for transition with the maximum lift coefficient, refer to Subsection 2.9.1 and Equation (2.43). For the distance for transition the glide-ratio is also accounted, it defines the angle of the rotation. However, the diameter of the rotation is directly driven by the maximum lift coefficient which has more effect than the variation of the angle of rotation.
The shown results for the varied climb altitudes underline the drawn conclusions from the previous section. Practically spoken, the glide-ratio directly drives the distance for the climb segment whereas the ground-roll distance is dominated by the maximum lift coefficient.
As stated by Rudolph[14] and Flaig[15] the take-off configuration is targeted to balance maxi-

[14]Rudolph [5] page 41: *"Therefore, every optimization of the high-lift system takeoff configuration is aimed at finding a good compromise between the lift capability and the L/D efficiency"*

[15]Flaig [12] page 31-3: *"the aerodynamic optimization of the take-off configuration is aimed at finding the best compromise between lift capability and L/D efficiency to satisfy the requirements for both take-off field length and the climb rate."*

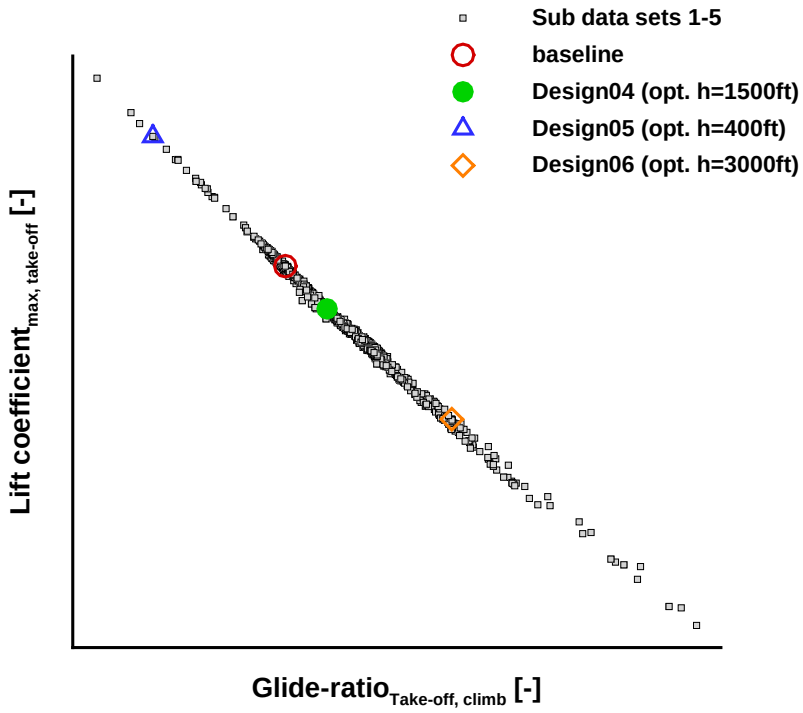

Figure 52: Take-off: maximum lift coefficient versus glide-ratio for climb segment.

Table 10: Percentual part of ground-roll, transition and climb segment on the overall take-off distance for different climb altitudes (H_{Climb}) for baseline configuration.

Climb altitude H_{Climb}	Distance for ground-roll $s_{\text{Take-off, ground-roll}}$	transition $s_{\text{Take-off, trans}}$	climb segment $s_{\text{Take-off, climb}}$
400ft	60%	12%	28%
1500ft	32%	6%	62%
3000ft	20%	4%	76%

mum lift and glide-ratio well. Since the gains in the take-off performance are rather small in comparison to the industrial designed baseline configuration for the 1500ft climb altitude, this scenario in conjunction with the domains of the parameters seems to be balanced rather realistically.

Figures 55 - 60 show the influence of the boundary condition of the take-off run on the ground-roll, climb and overall take-off distance. As stated before, it is again noticed within these figures that the data samples that reflect optimality for 400ft, 1500ft and 3000ft take-off altitude show opposite behavior. They are located towards the opposite extrema of the data samples.
As stated before, the data in plots (Figures 55, 56) are mirrored. These figures show the same data as Figures 50, 51 but other optimal designs are highlighted. This (mirroring of data) is found for the climb altitude of 3000ft again, refer to Figures 57, 58. For this climb altitude,

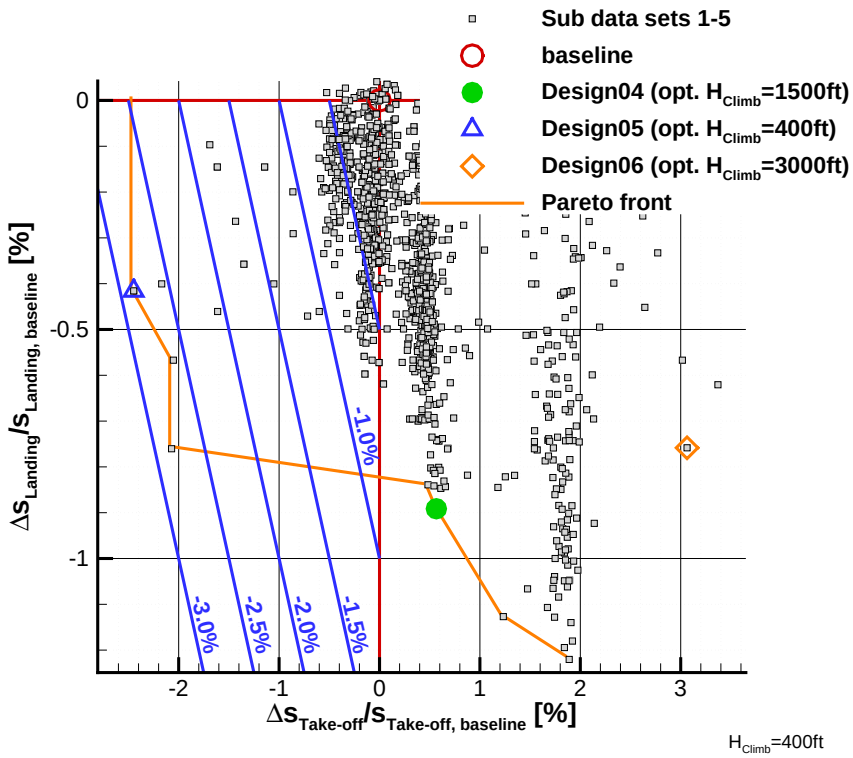

Figure 53: Take-off distance versus landing distance. The take-off run is evaluated up to a climb altitude of H_{Climb}=400ft.

the data samples for the climb distance show a denser distribution than for the ground-roll distance. Especially in the center of the plots a difference is observed, where for the left plot the data are condensed highly and in the right plot more pronounced gaps between the data samples are recognized. This observation underlines the statement made earlier that the variation of the ground-roll distance impacts less the overall take-off distance compared to the climb distance. Hence the optimization needs to focus on achievements in the glide-ratio for the take-off configuration, whereas the maximum lift has a lower importance. The bulk of the data base is generated under consideration of 1500ft climb altitude. For 3000ft the data samples are simply recomputed and no additional data is generated. Hence, the data base is not fully covering the design space for this climb altitude. However, the data base covers the design space sufficiently since the optimal configurations are not located at the bounds of the data. The influence of the climb altitude is perceived in a realistic manner.
Figures 59, 60 present the distribution of data for the climb altitude of 400ft. One interesting aspect here is that the distribution of the data samples looks different than for the previous studied climb altitudes. The data samples show roughly a linear behavior for overall take-off distance versus the ground-roll distance, whereas for the overall take-off distance versus the climb distance a slight non-linear behavior is noticed. The domain of the climb distance is less than a quarter of the domain of the ground-roll distance in absolute numbers. Variations of the climb distance are so small that there is no recognizable influence on the overall take-off distance. Here, we can conclude that the influence of the climb distance is almost negligible compared to the distance for the ground-roll segment. It is found that the impact of the ground-roll distance is so high on the overall take-off distance that the spreading of the data samples for the climb segment show almost no effect on the overall take-off distance.

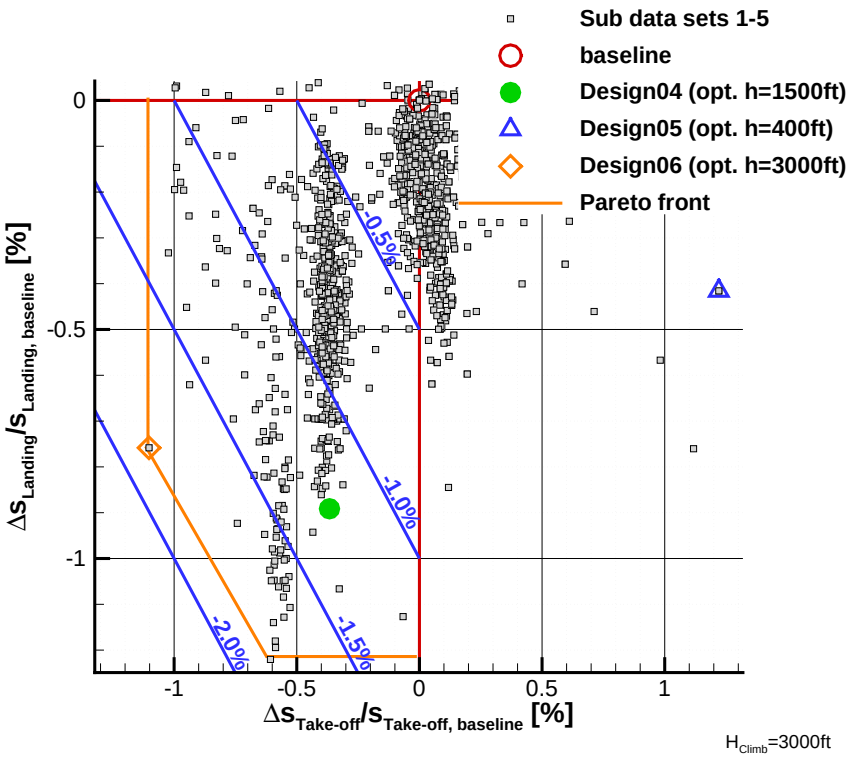

Figure 54: Take-off distance versus landing distance. The take-off run is evaluated up to a climb altitude of H_{Climb}=3000ft.

3.6.3 Landing Run

As described previously in Subsection 2.9.2, the landing run can be divided into approach, transition and ground-roll. Within this work, a typical glide slope of three degrees during approach for commercial airliners[16] is defined. Since the glide slope is constant the approach distance is also almost constant. Only due to the dependency of the transition phase on the maximum lift coefficient, the approach distance changes[17]. Generally it can be stated, that a reduction of the approach speed during landing leads to a shorter ground-roll distance. The approach aerodynamics are evaluated to ensure that depending on the actual setting of the high-lift system the thrust of the aircraft is sufficient to fly the defined glide slope.
Figures 61, 62 illustrate the maximum lift coefficient versus the normalized landing distance. The data suggest an anti correlation behavior of the two quantities. An increase of the maximum lift coefficient leads from a global point of view to a reduction of the overall landing distance. This behavior is expected and in aerodynamic high-lift optimizations landing performance is generally optimized by a maximization of the maximum lift coefficient. The *"critical landing parameter is generally approach speed"*[18], which is directly linked to the maximum lift coefficient. This target is reflected properly by the flight mechanics' evaluation.
In Figure 61 we recognize data samples of the overall data base in different colors by symbols. The domain of improved landing performance is shown compared to the baseline design. The red symbols in form of a diamond represent the data samples that have a decreased take-off performance, again compared to the baseline configuration, i.e. for these

[16] Rudolph [5] page 41
[17] refer to Subsection 2.9.2 and to Equations (2.55) and (2.58)
[18] Rudolph [5] page 41

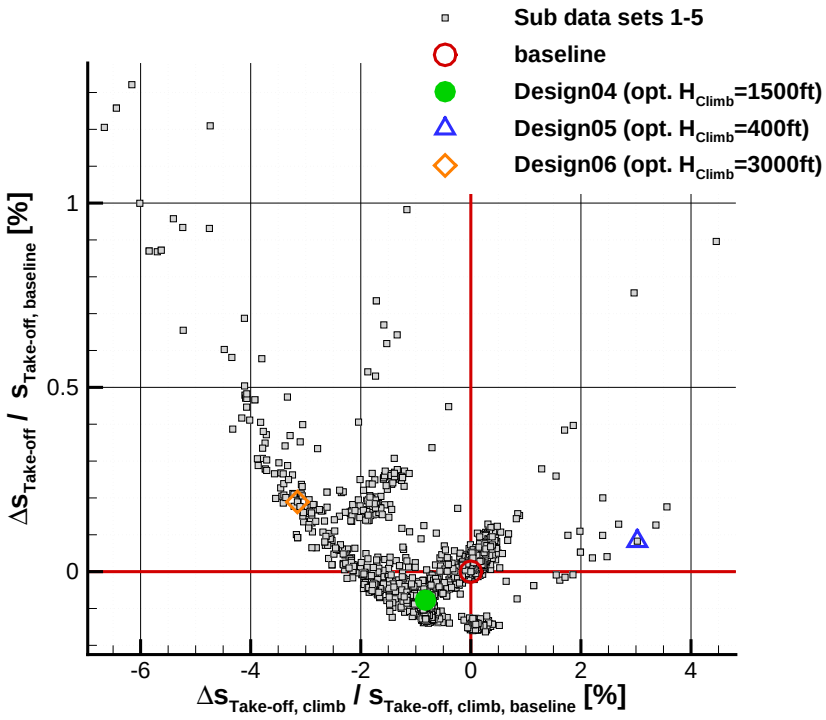

Figure 55: H_{Climb}=1500ft; percentual variation of the overall take-off distance versus the distance of climb segment for a climb altitude of 1500ft.

samples the following relationship is valid:

$$\Delta s_{\text{Take-off}} / s_{\text{Take-off, baseline}} > 0.$$

The grey symbols indicate the opposite. Additionally, the optimal samples on the Pareto front, the baseline configuration and the aerodynamic optimized configuration are highlighted. The optimal sample from the perspective of the landing run is the sample in the upper left corner, which is obtained by the pure aerodynamic optimization. The optimal sample under the consideration of the mechanism of the flap is a red sample with the peak performance in maximum lift coefficient. But this sample has a reduced take-off performance. When considering only the grey samples, to ensure that both take-off and landing performance are enhanced, the optimal configuration is Design04.
A further interesting aspect is the location of the Design03. Data samples exist, that have a less overall landing distance while the maximum lift coefficient is almost equal compared to Design03. This is motivated by an increased drag coefficient for ground-roll, which leads at an equivalent maximum lift coefficient, to a reduced ground-roll distance. Nevertheless, these data samples with reduced landing distance are not represented on the Pareto front, due to the duality with the take-off performance. Figure 62 shows the reason for it. This figure depicts next to the relationship of maximum lift coefficient and normalized overall landing distance, the normalized overall take-off distance. The take-off distance is represented as a color of the samples. In this figure it is discernible that for the samples left of Design03 with almost equivalent maximum lift coefficient and less landing distance the contour color changes gradually. The take-off distance increases slightly while moving left of Design03. Hence, Design03 reveals from a dual objective perspective with equally weighted distances a better performance than the samples on the left. The decrease in the normalized take-off distance is higher than the loss in the landing performance for Design03 compared

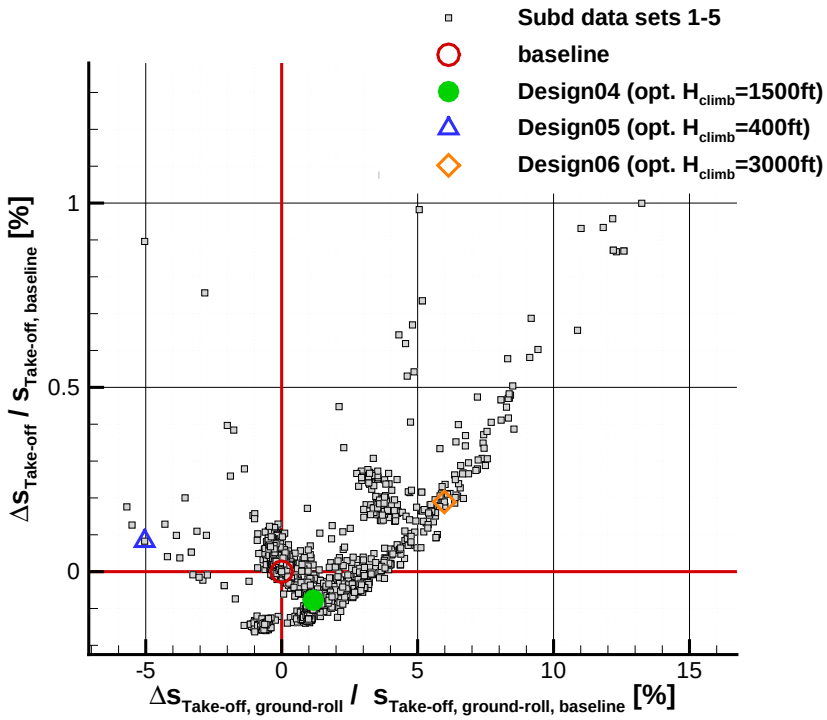

Figure 56: H_{Climb}=1500ft; percentual variation of the overall take-off distance versus distance for ground-roll for a climb altitude of 1500ft.

to the sample left of it.
Concluding remark: Within this section it is shown that the usage of an additional discipline to judge the aerodynamic performance during landing reflects properly the objectives regularly used within aerodynamic optimizations of landing configurations. In both approaches the maximum lift coefficient is the relevant quantity which dominates the landing performance.

3.7 Analysis of the Influence of the Mass of the Mechanisms

Within this section, additionally to the earlier discussed disciplines, the data base is evaluated under consideration of the mass of the slat and flap mechanism. The mass of the slat and flap mechanism is fed into the flight mechanics module and it influences maximum take-off weight, maximum landing weight and hence the overall take-off and landing distances. The weight of the aircraft (W) is calculated as presented in the following relationship:

$$\mathrm{W}_{\text{current}} = \mathrm{W}_{\text{baseline}} + (\mathrm{m}_{\text{mechanism, current}} - \mathrm{m}_{\text{mechanism, baseline}}) \cdot g. \tag{3.2}$$

This relationship reflects the variation of the weight of the overall aircraft (MTOW, MLW) based on the variations obtained by the mass estimation of the current design for the mechanism compared to the baseline design. Additionally, the relationship shows that the variation of the mass of the mechanisms affects only the operational empty weight, i.e. weights for payload and fuel among others remain constant. Equation (3.3) gives the relationship to calculate the overall mass of the mechanism.

$$\mathrm{m}_{\text{mechanism, current}} = \mathrm{k}_{\text{mechanism, Slat}} \cdot \mathrm{m}_{\text{mechanism, Slat}} + \mathrm{k}_{\text{mechanism, Flap}} \cdot \mathrm{m}_{\text{mechanism, Flap}}. \tag{3.3}$$

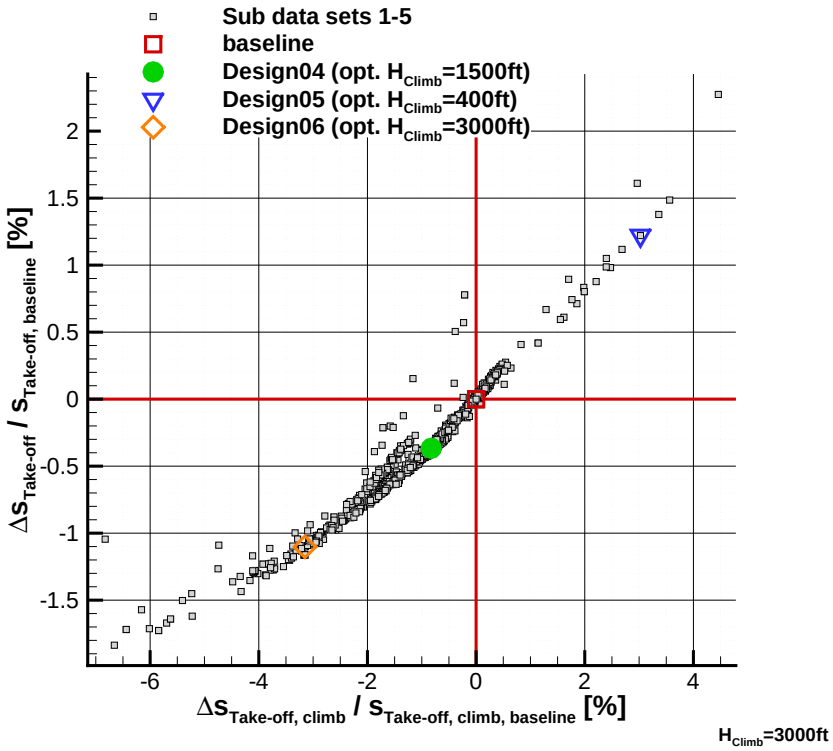

Figure 57: H_{Climb}=3000ft; percentual variation of the overall take-off distance versus distance of climb segment for a climb altitude of 3000ft.

k stands for the number of mechanisms (stations) that position the slat and flap elements and m reflects the mass of the mechanism. In this work, 15 slat stations and five flap stations are considered for each wing. Layouts for wings for commercial aircraft, their distribution and number of high-lift elements are presented by e.g. Flaig et. al [12], Rudolph [5] and Holert [54]. From these publications the number of stations (mechanisms) for the slat and flap elements are derived.
The data base presented before is postprocessed again for this investigation, such as the previously accounted constant maximum take-off weight and constant maximum landing weight are now adapted based on the current mass of the overall mechanism of each data sample. Hence, no additional data is generated for this analysis.

3.7.1 Mechanism for Flap Device

According to the work of Holert [54] and the documentation of TEFlaMeS [72] the method to estimate the mass of the flap mechanism is feasible. The validation of the mass estimation module for the flap, developed by the author, was done with the load cases for validation presented by Holert[19]. Within this work the high-lift flow conditions presented in Table 3 are used to predict the two-dimensional high-lift flow. Additionally, the cruise and dive condition are considered with retracted high-lift devices. For the dive case the aerodynamic loads of cruise are multiplied by a factor of 2.5. The absolute mass of the mechanism for the flap seems to be underestimated. The type of mechanism is the same as for the validation test case, but the overall mass of the mechanism obtained in this work is lower[20]. For

[19] refer to Subsection 2.8.2.
[20] A quantitative comparison cannot be given here, due to confidentiality.

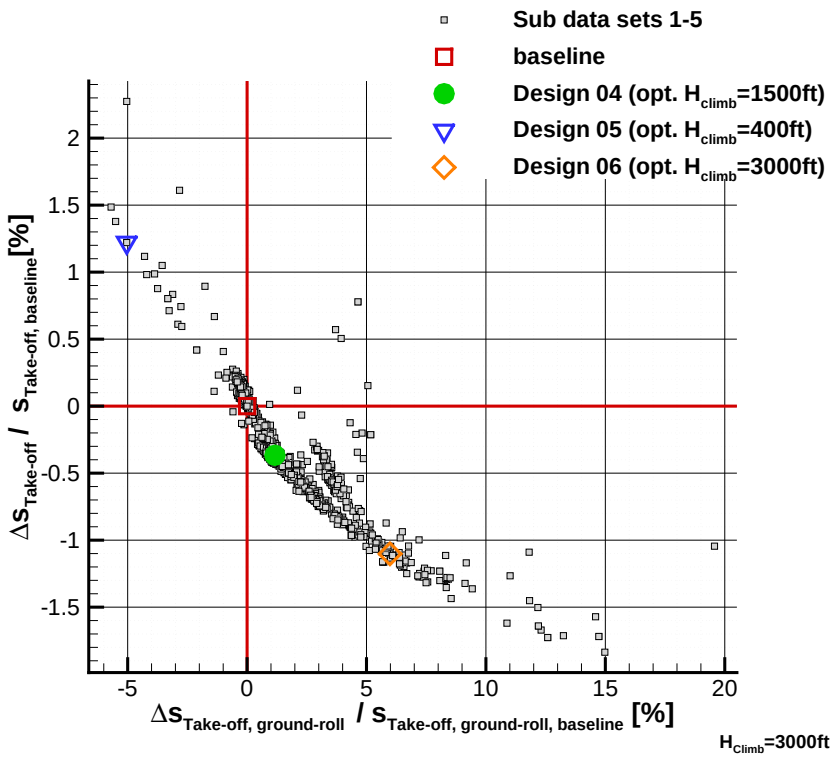

Figure 58: H_{Climb}=3000ft; percentual variation of the overall take-off distance versus distance for ground-roll for a climb altitude of 3000ft.

the estimation of the mass of the mechanism, no technology factors are used to increase its mass. We assume here that the absolute mass of the mechanism might be too low, but the qualitative tendencies of the mass changes are realistic.
For the flap mechanism, each flow condition for take-off is combined with each flow condition of the landing configuration to estimate the mass of the mechanism. The flow conditions dive and cruise are always accounted for. The aerodynamic loads for dive and cruise differ only by the afore mentioned factor. However, both conditions have to be accounted for each load case. The dive condition gives higher aerodynamic loads and may drive the mass of the mechanism. To interpolate properly the aerodynamic loads in between the retracted position and the take-off position of the flap the cruise load condition is used.
An overview of the load cases that are taken into account in this work is given in Table 11. In total nine load conditions are accounted during mass estimation of the mechanism for the flap device. This table shows that e.g. load case #1 is the combination of following flow conditions: maximum lift coefficient for the take-off setting, maximum lift coefficient for the landing setting, dive and cruise for the retracted high-lift system.
The load case that reaches the maximum overall mass of the mechanism for the current design is used to determine MTOW and MLW. These individual values of each design are used afterwards to evaluate the flight mechanics.
As mentioned before the aerodynamic loads are linearly interpolated w.r.t. the deflection angle of the flap. For three settings (retracted (cruise), take-off and landing) the aerodynamic loads are given and in between the loads are interpolated.
Another approach would be to sum up the overall mass of the mechanism by taking the maximum mass of each component of the mechanism from the different load cases (load case #1 to #9). However, it is found that the mass for the mechanism collapse for both approaches.

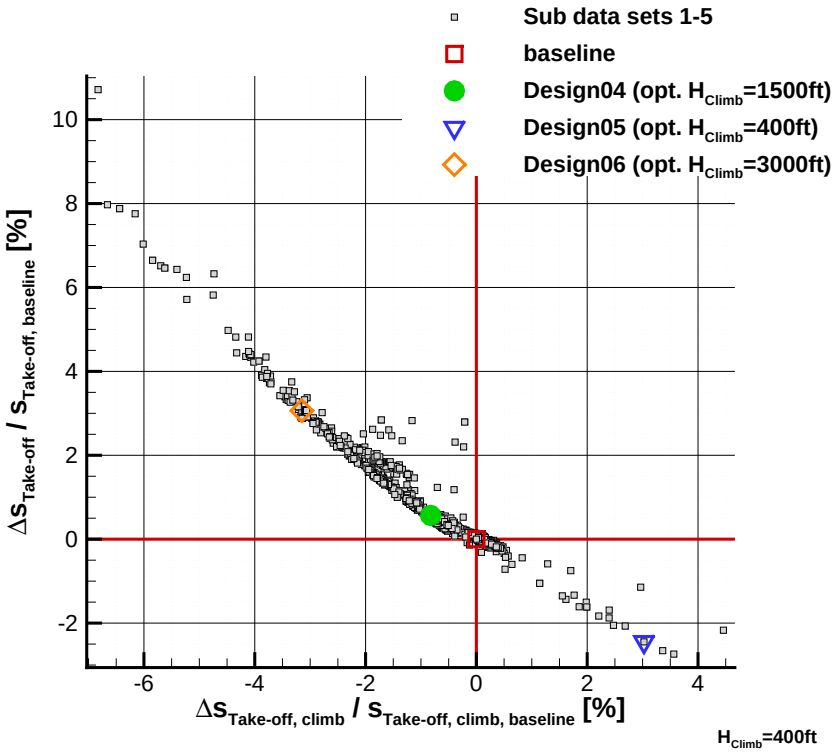

Figure 59: H_{Climb}=400ft; percentual variation of the overall take-off distance versus distance of climb segment for a climb altitude of 400ft.

Most of the time, the maximum mass of the mechanism is reached for the combination of climb condition for the take-off setting and approach condition for the landing setting (load case #5). Few times, the ground-roll condition for the landing setting and the climb condition during take-off is used to size the mechanism (load case #8). This implies that for the flap mechanism the aerodynamic condition at maximum lift coefficient, independent of the high-lift setting, is not the load condition that determines the system mass.
Figure 63 shows the lift and drag coefficient for slat and flap versus the angle of attack for baseline and Design04 for the high-lift system in take-off setting. We recognize that the lift coefficient on the flap decreases slightly while the angle of attack is increased. Whereas, the drag coefficient increases mildly. However, in comparison to the variations in lift and drag coefficient for the slat, the flap is roughly constant over the entire angle of attack range.
For the sake of completeness: the aerodynamic forces (F) are a function of the integral, aerodynamic coefficient multiplied with the flow velocity squared, for example for the lift it reads:

$$L = f(c_L, v_\infty^2) = f(c_L, \text{Ma}_\infty^2). \tag{3.4}$$

This explains why the load conditions that define the mass of the flap mechanism are not related to the maximum lift coefficient condition but to the higher loaded climb and approach condition. First, the aerodynamic lift coefficient is slightly enhanced and second, the Mach number is increased. The drag coefficient decreases but the drag coefficient is in absolute values only a portion of the lift coefficient, thus the influence is less dominant. Note, the lift force for the overall aircraft during flight is equal to the gravitational force of the aircraft. However, here the forces of the flap are individually regarded, therewith the lift force does not necessarily remain constant.
Qualitatively, the forces for lift and drag versus the angle of attack are shown for the take-

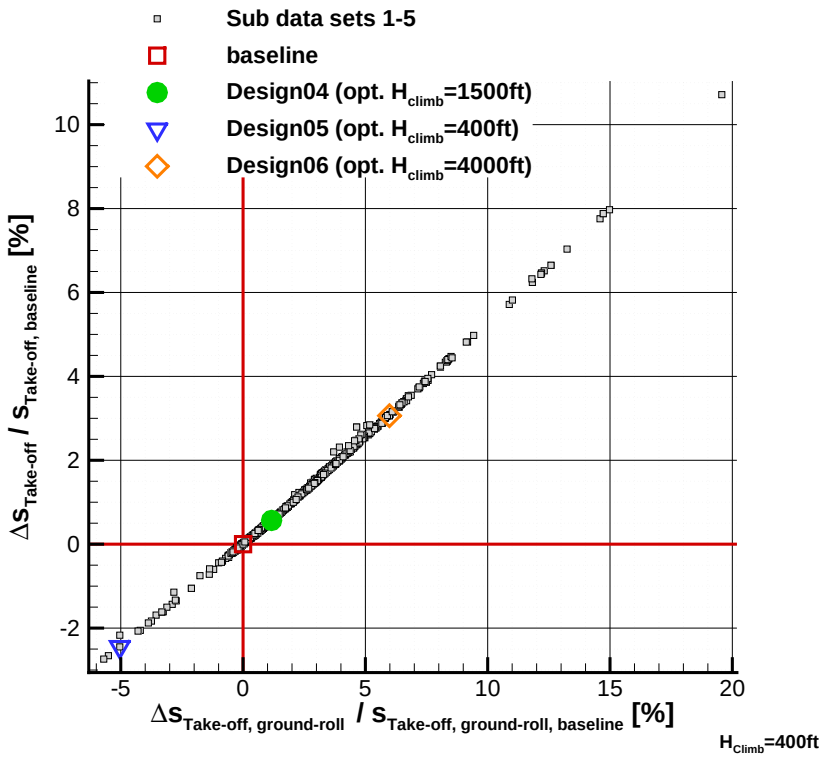

Figure 60: H_{Climb}=400ft; percentual variation of the overall take-off distance versus distance for ground-roll for a climb altitude of 400ft.

off setting at ground-roll, climb and at maximum lift coefficient condition in Figure 64. The aerodynamic coefficients are translated into forces for the discrete three flow conditions according to the on-flow velocity, angle of attack and lift coefficient.
For the flap, the climb condition reaches the highest force for lift and for drag, this is recognized for both designs. The variation of the aerodynamic lift force between the climb and the ground-roll condition are low. For the drag force, climb and the maximum lift coefficient conditions differ less. However, the drag force is only a portion of the lift force and influences less the mass of the mechanism. These observations agree well with the statement made before and it underlines why the load cases at lower angles of attack are the ones that lead to higher masses of the flap mechanism. The lever arm for the higher deflected landing setting plays an insignificant role according to the findings here.
Concluding remarks: The relevant load case that drive the mass of the mechanism for the flap device are most of the time climb during take-off and the approach during landing. These parts of the take-off and landing run exhibit the highest aerodynamic loads on the flap device. Only for a few times during landing, the ground-roll condition shows a higher aerodynamic load on the flap than the approach condition. These findings lead unfortunately not to a reduction of the computational effort, since the climb and approach condition both depend on the maximum lift coefficient for the take-off and landing configuration, respectively. Hence, it is necessary to determine the maximum lift coefficient for each sample for both the take-off and the landing configuration.

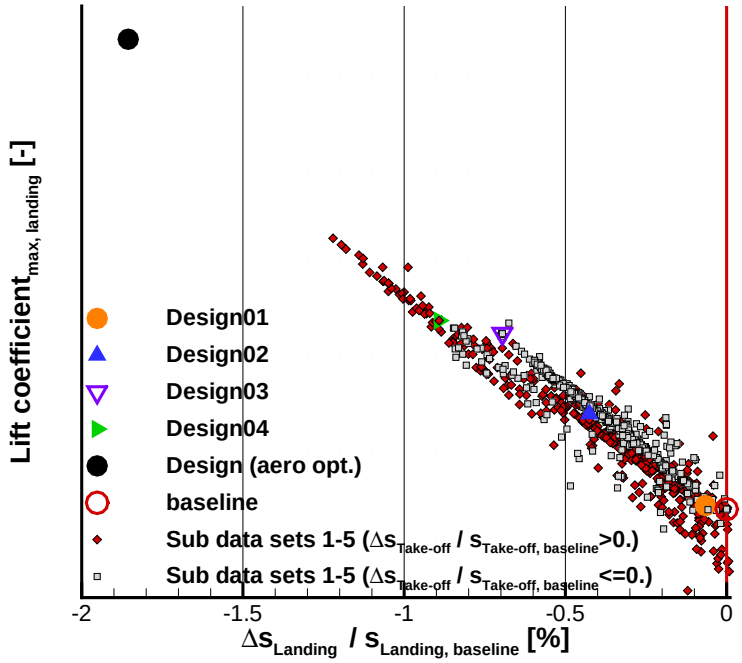

Figure 61: Maximum lift coefficient versus normalized landing distance.

3.7.2 Mechanism for Slat Device

For the method to determine the mass of the slat mechanism only the plausibility was checked, due to the lack of details on realistic slat mechanism designs. The method covers the mass estimation of the slat track beam, the rollers and the actuator, for illustration of the components refer to Figure 4. The actuator (pinion drive) is defined by the method of Holert [54], [72]. Consequently, the mass of the actuator is a function of the corresponding torque at the actuator. The rollers are sized based on a contact stress analysis. The slat track is sized at each setting (retracted/take-off/landing) with the different flow conditions related to this setting. The cross-section of the slat track beam is constant along its length, hence every load case covers only one flow condition to determine its size. The length of the slat track beam depends on the deflection angle of the landing setting for the slat. The cross-section of the slat track beam is illustrated in Figure 27. We have again the six high-lift on-flow conditions. In addition, the cruise and dive condition are considered. In total eight load cases are accounted. An overview of the load cases is given in Table 12. The load case that results in the highest mass of the slat mechanism defines its dimension.
Figure 63 shows the lift and drag coefficient distribution of the slat for a wide angle of attack domain. According to this figure, we recognize the increase of the lift coefficient for the slat while the angle of attack is increased, whereas the drag coefficient decreases. But the drag coefficient increases in magnitude, since it gets negative at small angles of attack. Thus, the highest aerodynamic load on the slat is achieved for the maximum lift coefficient condition. The results show that the slat mechanism is structurally sized by the maximum lift coefficient condition at take-off (load case #4). The Mach number for take-off at the maximum lift coefficient condition is higher than for landing. However, the maximum lift coefficient is smaller for take-off than for landing. The on-flow Mach number is of higher impact (refer to

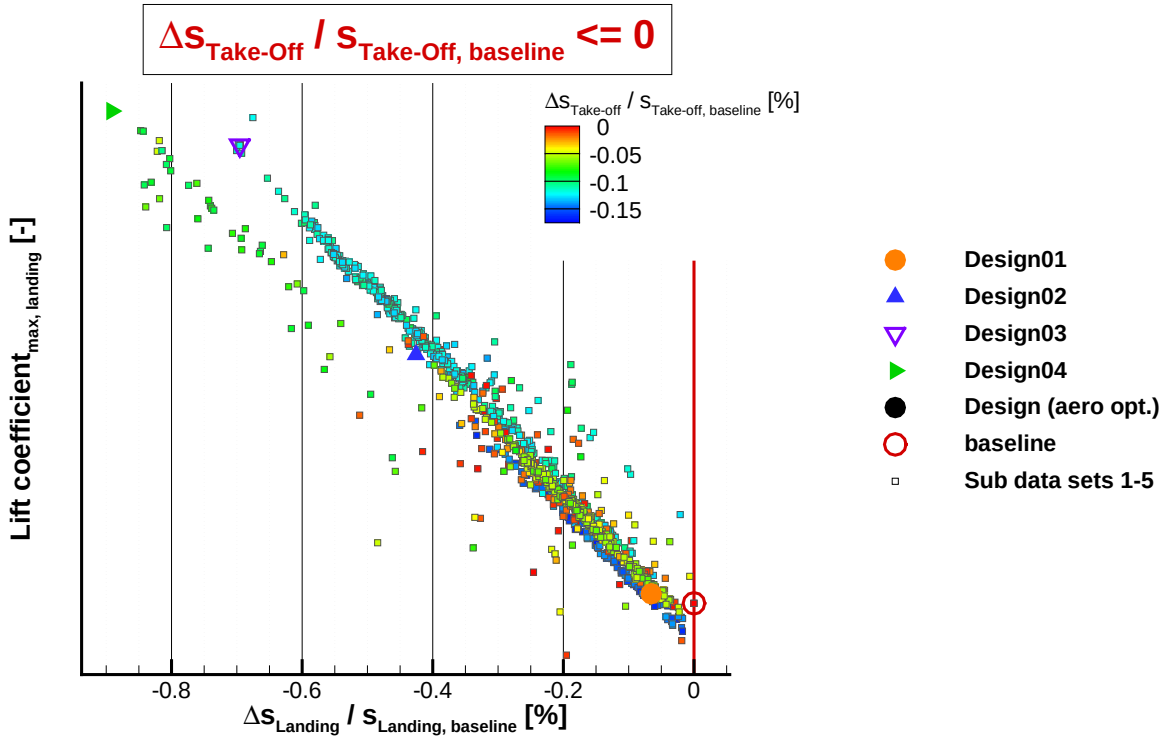

Figure 62: Maximum lift coefficient versus normalized landing distance. As contour the normalized take-off distance is shown. Data samples that have a reduced take-off performance compared to the baseline configuration are omitted.

Equation (3.4)) than the maximum lift coefficient for the aerodynamic forces. Consequently, it is plausible, that for the slat mechanism the design case that drives the mass of the mechanism is the maximum lift coefficient condition for the take-off setting.
Overall, it is reasonable that first the maximum lift coefficient condition, and second the take-off setting define the mass of the slat mechanism.
Now, let's have a look on Figure 64. It is recognizable that the lift force for the slat increases with the angle of attack, whereas the drag force decreases. But in magnitude the drag force increases, since it gets negative. The highest aerodynamic forces are achieved for the maximum lift coefficient condition. Hence, the drawn conclusions are in line with the observations priorly found.
Concluding remarks: According to the results presented before the dimensioning load case for the slat device mechanism is the maximum lift coefficient condition during take-off. From the view of the determination of the mass of the slat mechanism, it would not be necessary to calculate the maximum lift coefficient during landing. However, it cannot be neglected, since it is needed for the determination of the mass of the flap device.

3.7.3 Influence of Mass of Mechanisms on the Flight-Mechanics Performance

Figure 65 sketches the influence of the mass of slat and flap mechanism on the overall take-off and overall landing distance. These plots show only the data samples that form the Pareto front with and without the consideration of the mass of the mechanism respectively. According to this figure, we can recognize that both shape and position of the Pareto front

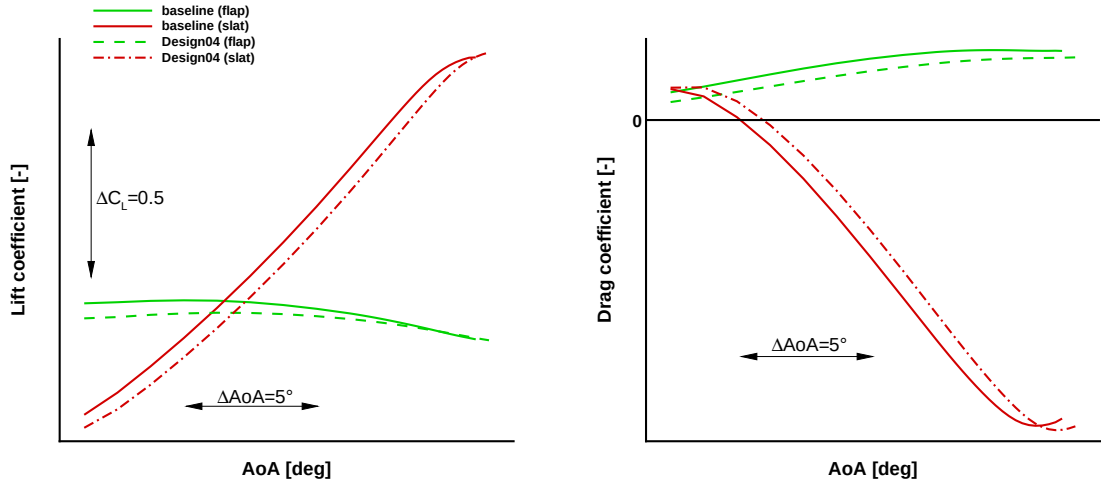

Figure 63: Aerodynamic coefficients for baseline and optimal configuration (Design04) for slat and flap in take-off configuration.

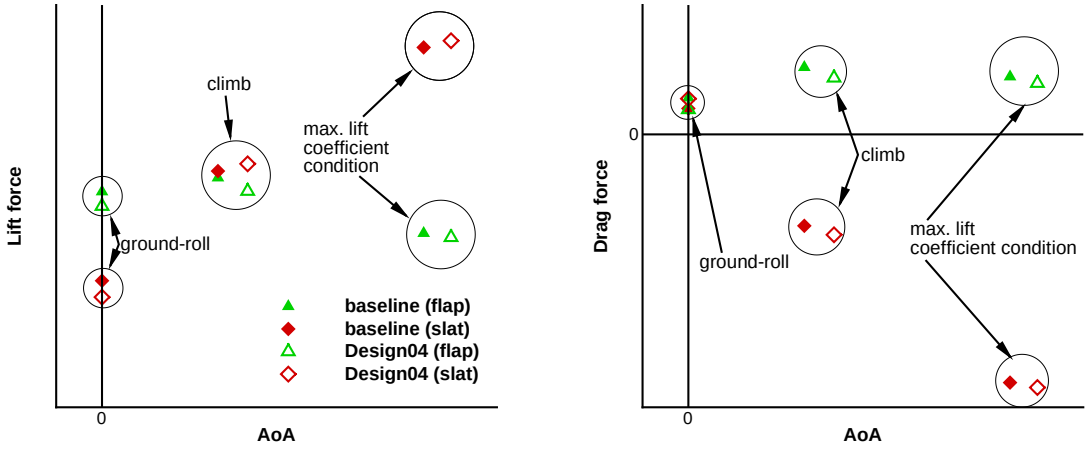

Figure 64: Aerodynamic forces for baseline and Design04 for slat and flap in take-off setting.

change when the overall mass of the mechanism is accounted for the flight mechanical relationships. The shape of the Pareto front for MTOW≠const. and MLW≠const. tends towards a so called "L-shaped"[21] Pareto front, but still there is not one single sample that reflects optimality both for take-off and landing. The position of the Pareto front changes as well, it moves towards higher enhancements of both the take-off and the landing performance. Overall, the best sample for the equally accounted normalized distances for take-off and landing is for both evaluations the same design (Design04). Without the consideration of the mass of the mechanisms the maximum improvement of the objective function, see Equation (3.1), exhibits roughly -0.48%, whereas under consideration of the mass of the flap and slat mechanism the benefit of the objective function is higher and reaches roughly -0.53%.
When it comes to the single components of the objective function the highest improvements are gained for take-off for the Design07 and for landing for Design04 both under the consideration of the overall mass of the mechanisms. The reductions in the take-off distance are

[21] refer to Iannelli et al. [44] and Moens et al. [48].

Table 11: Overview of load cases for mass estimation of flap mechanism.

setting	landing			take-off			retracted	
on-flow condition	max. lift coef.	approach	ground-roll	max. lift coef.	climb	ground-roll	dive	cruise
1	x			x			x	x
2	x				x		x	x
3	x					x	x	x
4		x		x			x	x
5		x			x		x	x
6		x				x	x	x
7			x	x			x	x
8			x		x		x	x
9			x			x	x	x

-0.18% and in the landing distance -0.92%. When both MTOW and MLW are constant the reductions are -0.16% for take-off and -0.89% for landing (refer to Subsection 3.3). However, the highest improvements are gained for take-off and constant weight for the Design01. The prior made statements are under the condition that both components of the objective function are enhanced in comparison to the baseline design, i.e. only samples that are located in the third quadrant are considered in these statements.
Now, let's have a look on the distribution of the data samples in both plots of Figure 65. We can recognize first, that most of the samples enhance their take-off and landing performance in comparison to the baseline configuration when the mass of the mechanism is considered. This observation means that the overall mass of the mechanism reduces for these data samples. Thus the overall mass of the aircraft reduces which is benefical for the flight mechanic's performance. Two samples are located in both plots roughly on the Pareto front for MLW=const. and MTOW=const.. This implies that the overall mass of the mechanism for these data samples are close to the overall mass of the mechanism for the baseline configuration. In this plot no sample is shown that actually decreases its take-off and landing performance. Therewith, one might conclude misleadingly that the overall mass of the mechanism stays constant or decreases for all data samples of the overall data base. We will now have a look on this issue and how the mass of the flap and slat mechanism change. Figure 66 depicts the relationship between the mass of the slat mechanism and the mass of the flap mechanism. The change of the overall mass of the mechanisms for the complete aircraft is indicated by iso-lines. Additionally, the normalized objective function is plotted by different colors of the symbols. This figure only shows the samples that exhibit improvements both in take-off and landing performance under the consideration of the overall mass of the mechanism (MTOW$\neq$ const., MLW$\neq$ const.) for the flight mechanics evaluation.
The bulk of data samples show a reduced overall mass of the mechanism. Peak reduction of the overall mass of the mechanism is approximately -7.6%. The increase in the overall mass reaches up to approximately +1.5% at maximum. Hence, this plot shows that the priorly made guess cannot be confirmed, since not all data samples reduce their overall mass. The overall mass of the flap mechanism is in the domain of -15.5% and +2.0%. For the overall mass of the slat mechanism the domain is smaller and it reads -0.6% and +5.2%. Only few

Table 12: Overview of load cases for mass estimation of slat mechanism.

setting	landing			take-off			retracted	
on-flow condition	max. lift coef.	approach	ground-roll	max. lift coef.	climb	ground-roll	dive	cruise
1	x							
2		x						
3			x					
4				x				
5					x			
6						x		
7							x	
8								x

samples are found that reduce both the mass of the slat and flap mechanism in comparison to the baseline design. The mass of the flap mechanism decreases for the bulk of samples, but an increase of the mass of the slat mechanism is obtained. The gains for the overall mass of the mechanism are mainly achieved by a reduction of the mass of the flap mechanism. The mass of the slat mechanism increases for most of the samples. Hence, its impact on the overall mass of the mechanisms of the whole aircraft is less dominant. The slope of the iso-lines indicates this behavior as well. Note here again, that the prior made statements are related to data samples that improve both take-off and landing performance.
In the following, the plausibility of the results w.r.t. to mass changes for the slat and flap mechanism is discussed. Let´s start with the discussion of the slat mechanism. Figure 64 showed the distribution of the lift force versus the angle of attack for take-off for the baseline configuration and the Design04. Prior, it was stated that the maximum lift coefficient condition for the take-off setting is the design case that sizes the slat mechanism. At this load condition the two designs differ slightly w.r.t. the lift and drag force. For Design04 the lift force and the slat deflection angle are increased compared to the baseline configuration. The drag force is marginally increased in magnitude. In Figure 66 we can see that the mass of the slat mechanism is increased for Design04 in comparison to the baseline configuration. Now, let's discuss if this finding is reasonable. Therefore, we first have a look back on Figures 37, 38. These figures showed that the deflection angle of the slat for take-off is higher for Design04 than for the baseline configuration. Therewith, the lever arm for both the drag force and the lift force increases slightly for Design04 than for the baseline configuration. Hence, the inner stresses in the slat track beam increase towards the position of the rollers. This leads to a slightly higher dimension of the Pi-section (increase in size of roughly 0.18%) and furthermore, it leads to a slight increase of the mass of the pinion drive (0.12%). These effects are based on the slight increase of the aerodynamic forces and on the increase of the slat deflection angle. Another aspect is the length of the slat track beam that naturally influences also the mass of the slat track beam. This length is determined by the landing setting of the slat. For the two discussed designs the deflection angle of the slat for the landing run is mildly increased for Design04 in comparison to the baseline configuration, as described before. Hence, it is reasonable that an increase of the mass of the slat mechanism is achieved for Design04 in comparison to the baseline configuration.

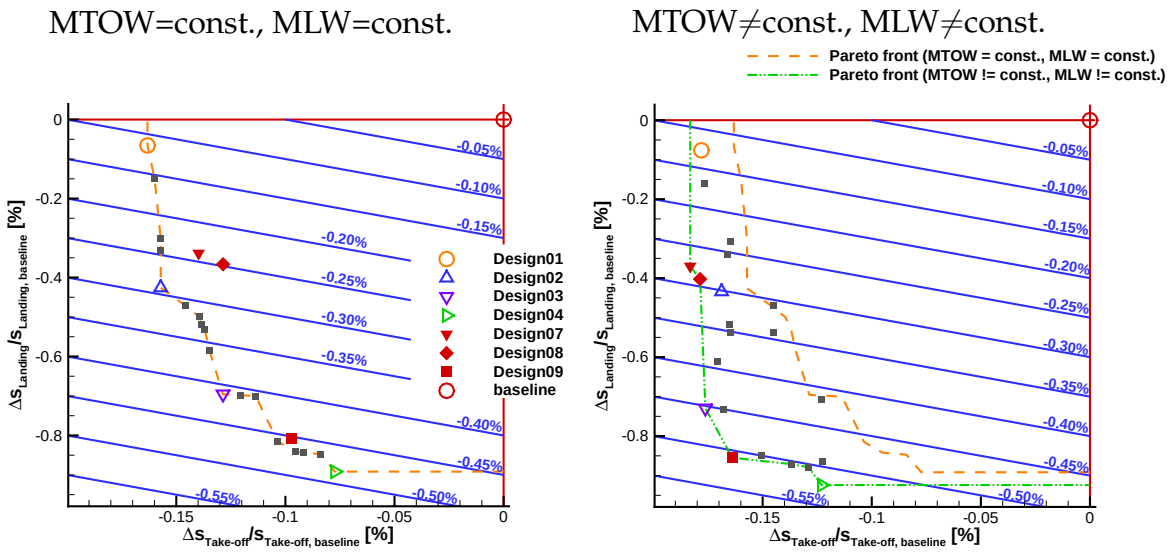

Figure 65: Left: normalized take-off distance versus normalized landing distance without the consideration of the weight of mechanisms (MTOW=const., MLW=const.). Right: normalized take-off distance versus normalized landing distance under consideration of mass of the mechanisms (MTOW≠const., MLW≠const.) Additionally, the Pareto front for the aircraft with constant weight (MTOW=const., MLW=const.) is depicted as well.

For most of the samples shown in Figure 66 the mass of the flap mechanism is decreased in comparison to the baseline design. Let's discuss where these reductions in mass are coming from and if these reductions are plausible. Table 13 gives an overview how the components of the mechanisms for the baseline, Design04 and Design09 change. According to Figure 66 Design09 is the sample with the highest reduction of the mass of the flap mechanism for the samples on the Pareto front (MTOW≠ const., MLW≠ const.), which is the reason to take it into account in the following discussion. This table shows significant reductions of the

Table 13: Percentual part of each component of the overall mechanism w.r.t. the overall mass of the mechanism of the baseline configuration.

Component	baseline [%]	Design04 [%]	Design09 [%]
Beams	62.2	56.4	55.6
Girders	6.8	6.9	6.2
Actuator	18.5	17.0	15.7
Rods	1.0	1.1	0.9
Carriage	7.7	7.5	6.8
Joints	3.8	4.0	3.5
Sum	100.0	92.9	88.7

overall mass of the flap mechanism for the improved designs. The reductions in the overall mass of the flap mechanism are 7.1% for Design04 and 11.3% for Design09 in comparison to the baseline configuration.

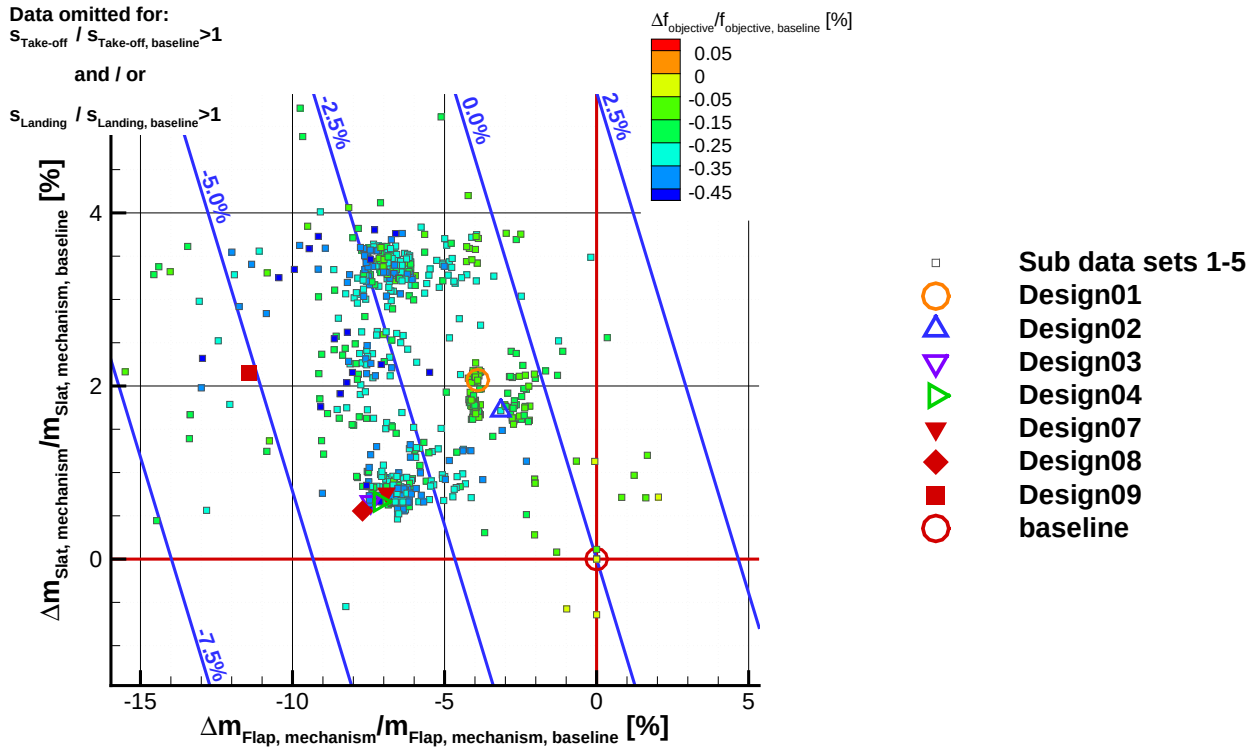

Figure 66: Normalized mass of the slat mechanism versus normalized mass of the flap mechanism. Objective function value is indicated as contour. Iso-lines illustrate the change in the overall mass of the mechanism for the whole aircraft.
Data samples that exhibit performance loss in take-off and/or landing compared to the baseline configuration are omitted.

In the following, we will have a closer look on the acting loads on the two components that have a high percentual part of the overall weight. These are the beam and the actuator, which determine roughly 80% of the mass of the mechanism. Additionally, the reductions of the overall mass of the mechanism for Design09 and Design04 are mainly driven by the reductions achieved for the beam and the actuator.
For the sizing of the beams the normal force (F_N), shear force (F_Q) and bending moment (M_{bending}) are the relevant quantities. For each beam and its flanges, these quantities define the dimension of the cross-section. The cross-section is constant along the beam and its flanges. Within stress analyses the highest loads for F_N, F_Q and M_{bending} are determined for each discrete deflection angle of the flap for the beams. The distribution of the loads versus the deflection angle of the flap is depicted in Figure 67 for the main beam, which dominates the weight of the beams. Table 14 compares the percentual variation in the beam height[22] and the variation in the overall beam length including the lengths of the flanges of Design09 and Design04 in comparison to the baseline configuration. According to the figure, we recognize that the highest load is received for all three designs for the take-off setting. Consequently, for this component both the landing setting and the retracted flap are not the sizing load case. For the two improved designs the distribution of the forces almost collapse, therewith it is plausible that the two designs have almost the same dimension in the cross-section of the beam. This is indicated in Table 14, where only a small difference in the beam height between Design04 and Design09 is recognized. However, since the lengths of both

[22]For illustration of the beam height, refer to Figure 22.

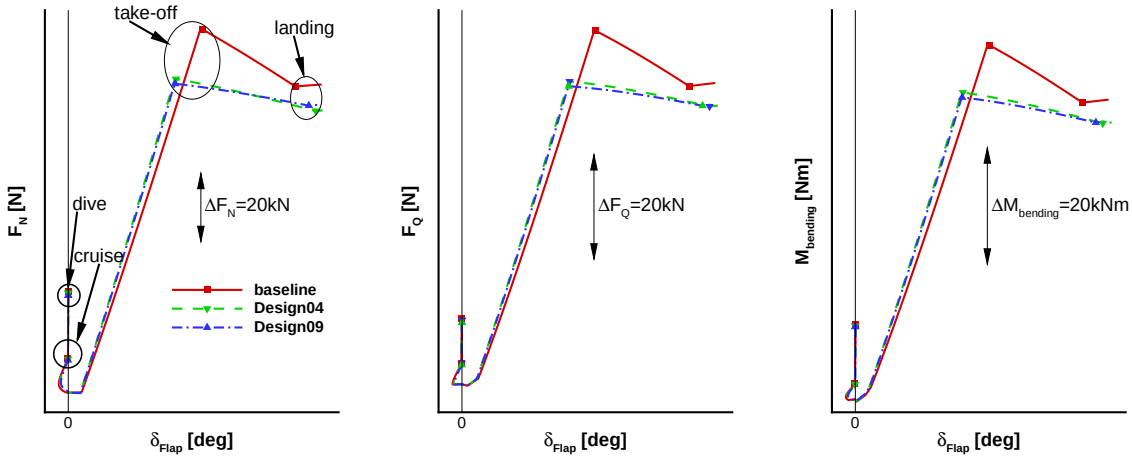

Figure 67: Distribution of highest inner forces (normal, shear) and moment (bending) versus the deflection angle of the flap for the main beam.

Table 14: Percentual part of beam geometry w.r.t. beam of the baseline configuration.

Component	baseline [%]	Design04 [%]	Design09 [%]
Beam length	100	99.97	99.64
Beam height	100	95.18	94.67

beams differ, the overall mass is necessarily not constant. Further on, it is evident that due to a significant increased maximum load for the baseline configuration, an increased length and height of the beam the overall mass for this component is considerably increased, compared to Design04 and Design09.
Next, we consider the actuator mass. It is determined by the maximum moment acting at the actuator. Figure 68 depicts the moment distribution at the actuator. The moment increases while the flap is deflected. It reaches its maximum at the take-off setting and while further deploying the flap the moment decreases. Hence, for the actuator the loads for the take-off setting determine its mass and for this component the landing setting is not the sizing load case. The three shown samples have different maximum moments. The highest moment is reached for the baseline configuration. Design04 reaches a lower moment at take-off and for Design09 the moment is even lower. This observation is reflected by the mass reductions reported by the mass estimation tool, where the same hierarchy is obtained.
Another aspect that needs to be mentioned is how the further extraction of the flap has to be dealt with. In the tool to simulate the flap deflection and to estimate the mass of the mechanism the flap is not necessarily deployed to its maximum at landing. In this tool, the forces are kept constant independent of the flap deflection angle for higher flap deflection angles than for landing. Since, we just examined that the cross-section of the beam and the actuator mass is determined by the take-off loads, the further extension is not critical w.r.t. to the mass estimation. The geometrical dimensions of the mechanism are considered and therewith the flap could be extended further without the need of reevaluating the mass of the system.
An aspect that is not reflected in this work is that the variation of the setting of the slat and

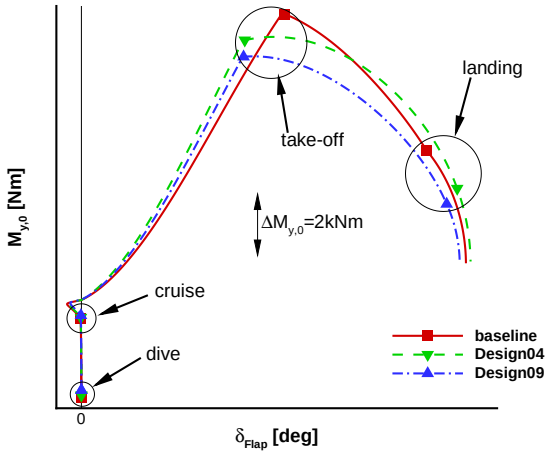

Figure 68: Distribution of aerodynamic moment versus the deflection angle of the flap at the actuator.

flap influences also the structural requirements to the structure of the flap and slat. Additionally, the structure of the main element, which has to sustain the aerodynamic loads of the flap and slat, is also not adapted here. In Figure 64 the distribution of the lift and drag force on the slat and the flap element is shown. For the slat both the lift and the drag force in absolute numbers at the maximum lift coefficient condition are slightly higher for the Design 4 in comparison to the baseline design. From this work, it can be expected that the structural weight of the slat might increase mildly for the Design 4. Here the question arises, which load case is used to do the structural sizing of the slat element.
For the flap element both the lift force and the drag force reduce for ground roll, climb and the maximum lift coefficient condition for the Design 4 in comparison to the baseline design. Therefore, it can be expected that the structural weight of the flap element is not increased. Hence, from this discussion it cannot be confirmed that the structural weight of the slat element need to be adjusted due to the minor increased loads at high angles of attack.
This issue should be investigated further to evaluate how the structural weight of the slat element and also the flap element need to be adjusted based on the variation of the outer aerodynamic loads.
Finally, it has to be pointed out again that the overall mass of the mechanism is expected to be underestimated in this simulation framework. Hence, possible savings in the mass of the high-lift mechanism are expected to be higher in practice and thus the gains shown here are conservatively estimated.
Concluding remarks: Overall it is shown exemplarily, that the variations of the mass of the high-lift mechanism are plausible. Savings in the system mass of high-lift designs are a result of reductions obtained by mass decreases for the flap device mechanism. Mostly, these designs have slat device mechanisms with increased system mass. I.e. the savings in the high-lift mechanism system mass are based on savings in the mass of the flap mechanism. Variations in the system mass are more pronounced for the flap mechanism in comparison to the variations of the slat mechanism. The choice of the type of mechanism is expected to be the crucial step for the definition of the domain of the mass of the high-lift system.
Comparing the designs with and without the consideration of the system mass of the high-lift system following conclusions can be drawn. First, the consideration of the system mass of the high-lift system is beneficial for the flight mechanics performance. Benefits are gained,

since most of the times the overall system mass of the high-lift system is reduced and hence the flight mechanics performance is enhanced. This is valid for the designs that show improvements in both take-off and in landing performance. Second, the distribution of the data samples is influenced by the consideration of the system mass. The Pareto front changes its shape. It tends more towards a so-called "L-shaped" Pareto front when the system mass is considered during the flight mechanics evaluation.

4 Conclusions and Outlook

This work covers investigations with respect to the mutual influence of the disciplines involved in the high-lift design process. Disciplines considered are the aerodynamics, kinematics, mass estimation of the high-lift system and flight mechanics. In the first place, a process was set up to enable the data generation. This step covers not only the implementation of the process chain, but also effort was spent to implement and/or adapt modules for the design process of the various disciplines. Additionally, validation of each implemented module was performed to ensure reliable results. This multifunctional process chain was used to investigate the influence of the mentioned disciplines on the optimal high-lift design, such as various data bases were generated. Afterwards the single data were merged together and the resulting overall data base was analyzed in detail from different points of view. To analyze the overall data base, all samples of the data base were postprocessed to achieve a data base that is based on the same boundary conditions, same judgment criteria and same parameter space. The analysis was done to determine first plausibility of the overall data base, and second to investigate the influence of the single disciplines on the distribution of the data samples. Additionally, benefits and drawbacks of a multidisciplinary approach were discussed. The major outcomes of these investigations and recommendations, which disciplines should be considered during a future high-lift design process, are given in the following.
It is shown that the data gained in this work are plausible. It is found that the monodisciplinary approach reaches more pronounced improvements compared to the multidisciplinary approach. This is due to the higher flexibility of the flap setting when the flap mechanism is neglected. The design space for the flap setting is less restricted when the aerodynamic parameterization for the flap is applied.
The high-lift enhancements of the samples during the data generation within this thesis are always compared to the baseline configuration. The baseline configuration is of a very successful aircraft in service and was designed by industry in a multidisciplinary context with various design teams involved from different disciplines in an iterative process. With this in mind, the result of finding only minor improvements compared to the baseline configuration is reasonable and it is seen as a great success. The automated process chain is able to detect optimal high-lift settings close to the design provided by industry and it is able to even enhance the high-lift performance.
In addition, the comparison of the final design with respect to the baseline design does not show the full capability of the used method, since one should compare the enhancements of the optimized design with the starting point used in industry, which is unfortunately not available. Naturally, the starting design of industry should be used as baseline design for the data generation process.

In the following, the involved disciplines are reviewed and recommendations on the necessity to cover them in a multidisciplinary design are given.

Kinematics: The results reveal that there is a great benefit in simulating the kinematics within a high-lift design process to gain a feasible multidisciplinary design. Overall it is highly recommended from this thesis to account the kinematics of the slat and flap mechanisms in future high-lift design tasks. On one hand, the number of high-lift setting is higher for a realistic design of a commercial airliner (take-off I-III, approach, full landing) and on the other hand the trend for the trailing edge high-lift systems is to use simpler mechanisms. This leads directly to less degree of freedom for the mechanism, while increasing the number of settings. Both aspects are not beneficial for the design of a high-lift mechanism, when the settings are derived independently, i.e. by aerodynamic optimizations. Hence, the process to design the high-lift mechanisms has to be performed iteratively or a compromise has to be agreed on. The compromise covers the definition of important settings and settings that not necessarily have to be identically realized. It is shown in this thesis that when the flap mechanism is neglected, the high-lift settings found are not realizable with the predescribed high-lift mechanism.

For the simulation of the **Aerodynamics**, a big effort was done to reduce the turn-around cycles of the data generation by mesh coarsening. For the analysis of the high-lift configurations, the aerodynamics was recomputed with finer meshes, higher accuracy for the aerodynamic, integral coefficients and a higher resolution of the angle of attack domain for the determination of the maximum lift coefficient. It is found, that the trends of the results of the data base are well reproduced. Hence, the accomplished steps for the data generation to decrease the turn-around cycles for each design sample do not show unfavorable impact on the results, i.e. they are feasible, reliable.

The **Flight Mechanics** is a relevant discipline to weigh the single aerodynamic coefficient realistically and to account additionally for the variations of the mass of the mechanism. It is shown that by using this discipline in the presented way, the aerodynamic objectives to optimize the system aerodynamically are reflected well. For landing the maximum lift coefficient is optimized, which is the important quantity for landing. For take-off, the maximum lift coefficient and the glide-ratio during climb are weighted. These two quantities need to be weighted properly. The kind of aircraft type that is to be designed determines the weightening. For this issue, the take-off climb height is recognized as a sensitive parameter to control the influence of both quantities.

The consideration of the **Mass Estimation** of the flap and slat mechanism influences the distribution of the data samples. When the mass estimation is considered, the Pareto front of the data base tends more towards a so-called “L-shaped” Pareto front. The high-lift performance enhances compared to the performance when the mass of the mechanisms is neglected. When the individual masses of the slat and flap mechanisms are examined the data show that the possible mass savings are achieved by the flap mechanism. Most of the time, the slat mechanism increases its mass for the samples in the third quadrant. The samples in the third quadrant enhance both their take-off and landing performance in comparison to the baseline configuration. The variations in the mass for the flap mechanism are significantly higher compared to the variations obtained for the slat mechanism. In total, the data suggest that the negligence of the mass estimation for the high-lift mechanisms leads to a more conservative contemplation of the design issue. Conservative contemplation means, possible enhancements for the high-lift performance are not exploited fully, when

the system mass of the high-lift mechanism is neglected during performance evaluations. In the beginning of the design task the type of mechanism is defined. This is expected to be the crucial step for the mass domain of the mechanism. The mass domain of the mechanism is the domain in which the mass of the mechanism can vary. The variations are due to geometrical variations of the mechanism and variations in the aerodynamic loads that are the result of setting changes. Hence, the type of mechanism has to be chosen carefully, when a certain system mass of the mechanism is aimed at.

For **future applications** the noise generation of the high-lift system will become more and more relevant. Hence, this discipline might be a good candidate to be further accounted in a coupled approach. With this discipline the quantity time-to-climb for the take-off might get relevant to reduce the noise abatement by climbing faster. For a future application, it would be valuable to evaluate in detail the benefits and drawbacks for different types of mechanisms, especially concerning their system mass. Further on, a study on high-lift systems in a multidisciplinary context should focus on three-dimensional aspects. The idea is to evaluate the limitations of the two-dimensional approach and to investigate if the tendencies found in this approach are valid for a three-dimensional configuration. Special attention may be set on relationships that cannot be evaluated in two-dimensions. In addition, the influence of the high-lift system on the cruise performance may be a future topic. Both, the fairing size of the flap mechanism and the mass of the high-lift system influence the cruise performance.
Additional aspects that may be tackled in the future are e.g. more elaborated flight mechanics, a multiobjective optimizer and reduced order model capabilities. For the flight mechanics, e.g. the balanced field length, landing climb and approach climb can be considered to enhance the simulation depth of the discipline. A multiobjective optimizer can be applied to focus on the determination of the Pareto front and to study more in detail the character of the trade-off. In terms of computational time, the aerodynamic computations are the bottle neck of the described approach. Hence, the use of reduced order models, such as e.g. a response surface method (RSM), might be a valuable option to save computational time. However, in the first place experience has to be achieved to be able first to set up properly a reliable RSM, and second to refine the RSM to gain trustworthy results in the parameter space. Besides the use of the RSM for temporal reductions, these capabilities enable to better understand the design space. Additionally, reliable predictions can be given, on how design changes (e.g. setting changes of high-lift elements) influence the overall performance.

Bibliography

[1] BAKER, T. J.: Mesh generation: Art or science? *Progress in Aerospace Sciences*, Vol. 41, Nr. 1, pp. 29–63 (2005).

[2] DAM, C. P.: The aerodynamic design of multi-element high-lift systems for transport airplanes. *Progress in Aerospace Sciences*, Vol. 38, Nr. 2, pp. 101 – 144 (2002).

[3] MEREDITH, P.: Viscous phenomena affecting high-lift systems and suggestions for future CFD development. *AGARD Conference Proceeding, CP-515, High-Lift System Aerodynamics*, pp. 19-1 – 19-8 (1993).

[4] BUTTER, D. J.: Recent Progress on Development and Understanding of High-Lift Systems. *AGARD Conference Proceeding, CP-365, Improvement of Aerodynamic Performance Through Boundary Layer Control and High Lift Systems* (1984).

[5] RUDOLPH, P. K. C.: High-Lift Systems on Commercial Subsonic Airliners. *NASA Contractor Report 4746* (1996).

[6] GARNER, P.L. ; MEREDITH, P.T. ; STONER, R.C.: Areas for Future CFD Development as Illustrated by Transport Aircraft Applications. *AIAA Paper 91-1527-CP*, pp. 10–20 (1991).

[7] ROGERS, S.E. ; ROTH, K. ; CAO, H.V. ; NASH, S.M. ; BAKER, M.D.: Computation of viscous flow for a Boeing 777 aircraft in landing configuration. *Journal of Aircraft*, Vol. 38, Nr. 6, pp. 1060–1068 (2001).

[8] RECKZEH, D.: Aerodynamic Design of the A400M High-Lift System. In: *Proceedings of the 26th International Congress of the Aeronautical Sciences ICAS*, 2008

[9] DILLNER, B. ; MAY, F.W. ; MCMASTERS, J.H.: Aerodynamic Issues in the Design of High-Lift Systems for Transport Aircraft. *AGARD Conference Proceeding, CP-365, Improvement of Aerodynamic Performance Through Boundary Layer Control and High Lift Systems*, pp. 9-1 – 9-22 (1984).

[10] EUROPEAN COMMISION: *European Aeronautics: A Vision for 2020*. Office for Official Publications of the European Communities, 2001. – ISBN 92–894–0559–7

[11] EUROPEAN COMMISION: *Flightpath 2050 Europe's Vision for Aviation*. Office for Official Publications of the European Communities, 2011. – ISBN 978–92–79–19724–6

[12] FLAIG, A. ; HILBIG, R.: High-lift design for a large civil aircraft. *AGARD Conference Proceeding, CP-515, High-Lift System Aerodynamics*, pp. 31-1 – 31-12 (1993).

[13] SMITH, A. M. O.: High-Lift Aerodynamics. *Journal of Aircraft*, Vol. 12, Nr. 6, pp. 501–530 (1975).

[14] MOIR, I. R. M.: Measurement on a Two-Dimensional Airfoil with High-Lift Devices. *AGARD Advisory Report, AR-303, Vol. I, A Selection of Experimental Test Cases for the Vali-*

dation of CFD Codes, pp. A2-1–A2-12 (1994).

[15] QUEST, J. ; WRIGHT, M. ; HANSEN, H. ; MESURO, G.: First measurements on an Airbus high lift configuration at ETW up to flight Reynolds number. *AIAA Paper 2002-0423* (2010).

[16] RECKZEH, D. ; HANSEN, H.: High Reynolds-number windtunnel testing for the design of Airbus high-lift wings. In: RATH, H.J. (Hrsg.) ; HOLZE, C. (Hrsg.) ; HEINEMANN, H. J. (Hrsg.) ; HENKE, R. (Hrsg.) ; HONLINGER, H. (Hrsg.): *New Results in Numerical and Experimental Fluid Mechanics V* Vol. 92 Notes on Numerical Fluid Mechanics and Multidisciplinary Design. Springer, 2006, pp. 1–8

[17] JIRASEK, A. ; ELIASSON, P. ; WALLIN, S.: Computational study of the high-lift a-airfoil. *Journal of Aircraft*, Vol. 38, Nr. 4, pp. 769–772 (2001).

[18] RUDNIK, R. ; ELIASSON, P. ; PERRAUD, J.: Evaluation of CFD methods for transport aircraft high lift systems. *Aeronautical Journal*, Vol. 109, Nr. 1092, pp. 53–64 (2005).

[19] MURAYAMA, M. ; YAMAMOTO, K. ; KOBAYASHI, K.: Validation of computations around high-lift configurations by structured- and unstructured-mesh. *Journal of Aircraft*, Vol. 43, Nr. 2, pp. 395–406 (2006).

[20] ELIASSON, P.: Investigation of a half-model high-lift configuration in a wind tunnel. *Journal of Aircraft*, Vol. 45, Nr. 1, pp. 29–37 (2008).

[21] SCHINDLER, K. ; RECKZEH, D. ; SCHOLZ, U. ; GRIMMINGER, A.: Aerodynamic Design of High-Lift Devices for Civil Transport Aircraft Using RANS CFD. *AIAA Paper 2010-4946* (2010).

[22] RUMSEY, C.L. ; SLOTNICK, J.P. ; LONG, M. ; STUEVER, R.A. ; WAYMAN, T.R.: Summary of the First AIAA CFD High-Lift Prediction Workshop. *Journal of Aircraft*, Vol. 48, Nr. 6, pp. 2068–2079 (2011).

[23] RUMSEY, C. L. ; SLOTNICK, J. P.: Overview and Summary of the Second AIAA High-Lift Prediction Workshop. *Journal of Aircraft*, Vol. 52 (2015).

[24] RUMSEY, C. L. ; YING, S. X.: Prediction of high-lift: review of present CFD capability. *Progress in Aerospace Sciences*, Vol. 38, Nr. 2, pp. 145–180 (2002).

[25] RUDNIK, R. ; SCHWETZLER, D.: High lift INflight VAlidation (HINVA) - Overview about the 1st Flight Test Campaign. *AIAA Paper 2014-2843* (2014).

[26] RUDNIK, R. ; SCHWETZLER, D.: High lift INflight VAlidation (HINVA) - Overview about the 2nd Flight Test Campaign. *AIAA Paper 2016-0041* (2016).

[27] BIER, N. F. ; ROHLMANN, D. ; RUDNIK, R.: Numerical Maximum Lift Predictions of a Realistic Commercial Aircraft in Landing Configuration. *AIAA Paper 2012-0279* (2012).

[28] BIER, N. ; RUDNIK, R. ; QUEST, J. ; RECHLIN, A.: Stall Behavior of the HINVA KH-A320-HA Highlift Model in ETW. *AIAA Paper 2015-1226* (2015).

[29] RUDNIK, R. ; RECKZEH, D. ; QUEST, J.: HINVA - High lift INflight VAlidation - Project Overview and Status. *AIAA Paper 2012-0106* (2012).

[30] WILD, J.: Recent research topics in high-lift aerodynamics. *CEAS Aeronautical Journal*, Vol. 7, Nr. 3, pp. 345 – 355 (2016).

[31] RECKZEH, D.: Aerodynamic design of the high-lift-wing for a Megaliner aircraft. *Aerospace Science and Technology*, Vol. 7, Nr. 2, pp. 107–119 (2003).

[32] NIELD, B. N.: An overview of the Boeing 777 high lift aerodynamic design. *Aeronautical Journal*, Vol. 99, Nr. 989, pp. 361–371 (1995).

[33] KAFYEKE, F. ; PÉPIN, F. ; KHO, C.: Development of High-Lift Systems for the Bombardier CRJ-700. In: *Proceedings of ICAS congress*, 2002

[34] LACY, D. S. ; SCLAFANI, A. J.: Development of the High Lift Common Research Model (HL-CRM): A representative High Lift Configuration for Transonic Transports. *AIAA Paper 2016-0308* (2016).

[35] NIU, M. C.-Y.: *Airframe Structural Design*. Hong Kong: Conmilit Press Ltd., 1997. – ISBN 962–7128–04–X

[36] EYI, S. ; LEE, K. D. ; ROGERS, S. E. ; KWAK, D.: High-lift design optimization using Navier-Stokes equations. *Journal of Aircraft*, Vol. 33, Nr. 3, pp. 499–504 (1996).

[37] BESNARD, E. ; SCHMITZ, A. ; BOSCHER, E. ; GARCIA, N. ; CEBECI, T.: Two-Dimensional Aircraft High Lift System Design and Optimization. *AIAA Paper 98-0123* (1998).

[38] WILD, J.: *Numerische Optimierung von zweidiminsionalen Hochauftriebskonfigurationen durch Lösung der Navier-Stokes-Gleichungen*, University of Braunschweig, Germany, Dissertation, 2001. – DLR-FB-2011-11

[39] WILD, J.: Multi-objective constrained optimization in aerodynamic design of high-lift systems. *International Journal of Computational Fluid Dynamics*, Vol. 22, Nr. 3, pp. 153–168 (2008).

[40] NEMEC, M. ; ZINGG, D. ; PULLIAM, T.: Multipoint and multi-objective aerodynamic shape optimization. *AIAA Journal*, Vol. 42, Nr. 6, pp. 1057–1065 (2004).

[41] BENINI, E. ; PONZA, R. ; MASSARO, A.: High-Lift Multi-Element Airfoil Shape and Setting Optimization Using Multi-Objective Evolutionary Algorithms. *Journal of Aircraft*, Vol. 48, Nr. 2, pp. 683–696 (2011).

[42] CARRESE, R. ; WINARTO, H. ; LI, X. ; SOBESTER, A. ; EBENEZER, S.: A comprehensive preference-based optimization framework with application to high-lift aerodynamic design. *Engineering Optimization*, Vol. 44, Nr. 10, pp. 1209–1227 (2012).

[43] BENINI, E. ; PONZA, R. ; IANNELLI, P. ; STRÜBER, H. ; HRNCIR, Z. ; MOENS, F. ; KÜHN, T.: Multi-Point Shape and Setting Optimization of High-Lift Airfoils in both Take-Off and Landing Conditions. In: *Proceedings of the European Congress on Computational Methods in Applied Sciences and Engineering (ECCOMAS 2012), Vienna, Austria*, 2012

[44] IANNELLI, P. ; WILD, J. ; MINERVINO, M. ; MOENS, F. ; RAETS, M.: Analysis and Application of suitable CFD-based Optimization Strategies for High-Lift System Design. In: *Proceedings of the European Congress on Computational Methods in Applied Sciences and Engineering (ECCOMAS 2012), Vienna, Austria*, 2012

[45] BREZILLON, J. ; WILD, J.: Evaluation of different optimization strategies for the design of a high-lift flap device. In: *Proceedings of the EUROGEN 2005, Evolutionary and Deterministic Methods for Design, Optimization and Control with Applications to Industrial and Societal Problems*, 2005

[46] WILD, J. ; BREZILLON, J. ; AMOIGNON, O. ; QUEST, J. ; MOENS, F. ; QUAGLIARELLA, D.: Advanced Design by Numerical Methods and Wind-Tunnel Verification Within European High-Lift Program. *Journal of Aircraft*, Vol. 46, Nr. 1, pp. 157–167 (2009).

[47] QUIX, H. ; SCHULZ, M. ; QUEST, J. ; RUDNIK, R. ; SCHRÖDER, A.: Low Speed High

Lift Validation Tests within the European Project EUROLIFT II. *AIAA Paper 2007-4298* (2007).

[48] MOENS, F. ; DANDOIS, J.: Optimization of Passive Flow Control Devices of a Slatless High-Lift Configuration. *Journal of Aircraft*, Vol. 53, Nr. 1, pp. 189–201 (2016).

[49] FRANKE, D. M. ; WILD, J.: Aerodynamic Design of a Folded Krüger Device for a HLFC Wing. In: DILLMANN, A. (Hrsg.) ; HELLER, G. (Hrsg.) ; KRÄMER, E. (Hrsg.) ; WAGNER, C. (Hrsg.) ; BREITSAMTER, C. (Hrsg.): *New Results in Numerical and Experimental Fluid Mechanics X* Vol. 132 Notes on Numerical Fluid Mechanics and Multidisciplinary Design. Springer, 2016, pp. 17–27. – DOI: 10.1007/978-3-319-27279-5_2

[50] DAM, C. P. ; SHAW, S. G. ; KAM, J. C. V. ; RUDOLPH, P. K. C. ; KINNEY, D.: Aeromechanical design of high-lift systems. *Aircraft Engineering and Aerospace Technology*, Vol. 71, Nr. 5, pp. 436–443 (1999).

[51] TAKENAKA, K. ; NAKAHASHI, K.: Aerodynamic optimization of 2–D High-Lift Device under Kinematic Constraints. In: *Proceedings of the 5th European Congress on Computational Methods in Applied Sciences and Engineering (ECCOMAS)*. Venice, Italy, 2008

[52] KOLLA, M. L. ; YOKATA, J. W. ; LASSALINE, J. V. ; FEJTEK, I.: Stowability Constraint Within a Two-Dimensional Aerodynamic Optimization Method. *Journal of Aircraft*, Vol. 46, Nr. 2, pp. 696–698 (2009).

[53] HOLERT, B. ; CARL, U.: Interdisziplinäre Synthese von Klappenführungsmechanismen. In: *Proceedings of Deutscher Luft- und Raumfahrtkongress 2002, Stuttgart, (DGLR-2002-155)*, 2002. – DOI: 10.15480/882.224

[54] HOLERT, B.: *Eine Methode zum mehrkriteriellen Entwurf der Führungsmechanismen in Hochauftriebssystemen von Transportflugzeugen*, University of Technology Hamburg, Germany, Dissertation, 2005

[55] KINTSCHER, M. ; WIEDEMANN, M. ; MONNER, H. P. ; HEINTZE, O. ; KÜHN, T.: Design of a smart leading edge device for low speed wind tunnel tests in the European project SADE. *International Journal of Structural Integrity*, Vol. 2, Nr. 4, pp. 383–405 (2011).

[56] PEPPER, R. S. ; DAM, C. P. ; GELHAUSEN, P. A.: Design methodology for high-lift systems on subsonic transport aircraft. *AIAA Paper 96-4056* (1996).

[57] ZACCAI, D. ; BERTELS, F. ; VOS, R.: Design methodology for trailing-edge high-lift mechanisms. *CEAS Aeronautical Journal*, Vol. 7, Nr. 4, pp. 521–534 (2016).

[58] KRETH, S.: Approach and Departure Procedure Variations to Reduce and Redistribute Noise. *AIAA Paper 2013-5170* (2013).

[59] FRANKE, D. M.: Aerodynamic Optimization of a High-Lift System with Kinematic Constraints. In: DILLMANN, A. (Hrsg.) ; HELLER, G. (Hrsg.) ; KREPLIN, H.-P. (Hrsg.) ; NITSCHE, W. (Hrsg.) ; PELTZER, I. (Hrsg.): *New Results in Numerical and Experimental Fluid Mechanics VIII* Vol. 121 Notes on Numerical Fluid Mechanics and Multidisciplinary Design. Springer, 2013, pp. 9–16. – DOI: 10.1007/978-3-642-35680-3_2

[60] FRANKE, D. M.: Multidisciplinary Optimization of a Generic 2D High-Lift Configuration Regarding Kinematics, Aerodynamics and Flight Mechanics. *AIAA Paper 2012-3017* (2012).

[61] FRANKE, D. M.: Investigation on continuously deflectable High-Lift Devices for a 3D High-Lift Configuration. *AIAA Paper 2015-2258* (2015).

[62] DREWS, J.: *Untersuchungen zur Interaktion von Struktur und Fluid bei Hochauftriebskonfigurationen*, University of Braunschweig, Germany, Dissertation, 2003

[63] KEYE, S.: Fluid-Structure Coupled Analysis of a Transport Aircraft and Flight-Test Validation. *Journal of Aircraft*, Vol. 48, Nr. 2, pp. 381–390 (2011).

[64] NOCEDAL, J. ; WRIGHT, S. J.: *Numerical Optimization*. Springer, 1999. – ISBN 0–387–98793–2

[65] TRAPANI, G. ; KIPOUROS, T. ; SAVILL, A. M.: The Design of Multi-element Airfoils Through Multi-Objective Optimization Techniques. *CMES: Computer Modeling in Engineering and Sciences*, Vol. 88, Nr. 2, pp. 107–140 (2012).

[66] ROWAN, T.: *Functional Stability Analysis of Numerical Algorithms*, University of Texas at Austin, USA, Dissertation, 1990

[67] NELDER, J. A. ; MEAD, R.: A Simplex Method for Function Minimization. *Computer Journal*, Vol. 7, pp. 308–313 (1965).

[68] WIKMAN, B. ; BERGMAN, G. ; OLDENBURG, M. ; HAGGBLAD, H.-A.: Estimation of constitutive parameters for powder pressing by inverse modelling. *Structural and Multidisciplinary Optimization*, Vol. 31, Nr. 5, pp. 400–409 (2006).

[69] BREZILLON, J. ; ABU-ZURAYK, M.: Aerodynamic Inverse Design Framework using Discrete Adjoint Method. In: DILLMANN, A. (Hrsg.) ; HELLER, G. (Hrsg.) ; KREPLIN, H.-P. (Hrsg.) ; NITSCHE, W. (Hrsg.) ; PELTZER, I. (Hrsg.): *New Results in Numerical and Experimental Fluid Mechanics VIII* Vol. 121 Notes on Numerical Fluid Mechanics and Multidisciplinary Design. Springer, 2012, pp. 489–496. – DOI: 10.1007/978-3-642-35680-3_58

[70] BREZILLON, J. ; RONZHEIMER, A. ; HAAR, D. ; ABU-ZURAYK, M. ; LUMMER, M. ; KRÜGER, W. ; NATTERER, F.-J.: Development and application of multi-disciplinary optimization capabilities based on high-fidelity methods. *AIAA Paper 2012-1757* (2012).

[71] JENKINSON, L. R. ; SIMPKIN, P. ; RHODES, D.: *Civil Jet Aircraft Design*. Elsevier, 1999

[72] HOLERT, B. ; CARL, U.: Rechnerunterstützte Synthese von Klappenführungsmechanismen / Hamburg University of Technology, Institute of Aircraft System Engineering. 2005. – No.: 04-158, v1.08

[73] FEDERAL AVIATION ADMINISTRATION: *Code of Federal Regulations (CFR), Titel 14: Aeronautics and Space, Part 25-Airworthiness standards: transport category airplanes*. 2015

[74] RAYMER, D. P.: *Aircraft Design: A Conceptual Approach*. American Institute of Aeronautics and Astronautics, 1992

[75] BRODERSEN, O. ; RONZHEIMER, A. ; ZIEGLER, R. ; KUNERT, T. ; WILD, J. ; HEPPERLE, M.: Aerodynamic Applications using MegaCads. In: *Proceedings of the 6th Intern. Conference on Numerical Grid Generation*. London : Ed.: M.Cross et. al., 1998

[76] WILD, J.: Application of Smooth Mixed Meshes Based on Metric Identity in Aerospace Analysis and Design. In: *Proceedings of the 17th International Meshing Roundtable*, Springer, 2008, pp. 387–397

[77] GERHOLD, T.: Overview of the Hybrid RANS Code TAU. In: KROLL, N. (Hrsg.) ; FASSBENDER, J. (Hrsg.): *MEGAFLOW – Numerical Flow Simulation for Aircraft Design* Vol. 89 Notes on Numerical Fluid Mechanics and Multidisciplinary Design. Springer, 2005, pp. 81–92

[78] KERLE, H. ; PITTSCHELLIS, R. ; CORVES, B.: *Einführung in die Getriebelehre*. B.G. Teubner Verlag, 2007

[79] BURTON, P.: *Kinematics and Dynamics of Planar Machinery*. Prentice-Hall, 1997

[80] VEREIN DEUTSCHER INGENIEURE: Modulare kinematische Analyse ebener Gelenktriebe mit Dreh- und Schubgelenken. 1995. – VDI-Richtlinie 2729, VDI Handbuch Getriebetechnik I

[81] WOODWARD, D.S. ; LEAN, D.E.: Where is High-Lift Today. *AGARD Conference Proceeding, CP-515, High-Lift System Aerodynamics*, pp. 1-1 – 1-45 (1993).

[82] ANDERSON(JR), J. D.: *A History of of Aerodynamics and Its Impact on Flying Machines*. Cambridge Univerity Press, 1997

[83] WILCOX, D. C.: *Turbulence Modeling for CFD*. DCW Industries, 1998. – ISBN 0963605151

[84] SPALART, P. R. ; ALLMARAS, S. R.: A One-Equation Turbulence Model for Aerodynamic Flows. *AIAA Paper 1992-043* (1992).

[85] RUMSEY, C. L. ; LEE-RAUSCH, E. M. ; WATSON, R. D.: Three-dimensional effects in multi-element high lift computations. *Computers & Fluids*, Vol. 32, Nr. 5, pp. 631–657 (2003).

[86] WANG, X.-L. ; WANG, F.-X.: Aerodynamic Characteristics of High-Lift Devices with Downward Deflection of Spoiler. *Journal of Aircraft*, Vol. 48, Nr. 2, pp. 730–735 (2011).

[87] HAIN, R.: Ein effizientes Verfahren zur automatisierten numerischen Ermittlung des maximalen Auftriebsbeiwerts von Hochauftriebskonfigurationen. 2003. – Diploma Thesis, University of Braunschweig, Germany

[88] PEETERS, K. ; JANSSENS, S. ; RAETS, M.: personal communication (2011).

[89] LANGER, S.: personal communication (2011).

[90] KLEIN, M.: *Einführung in die DIN-Normen*. Teubner, 1989

[91] MCLEAN, D.: *Understanding Aerodynamics Arguing from the Real Physics*. Wiley, 2012. – ISBN 978–1119967514

List of Tables

List of Figures